TELECOMMUNICATION ENGINEERING

UNIVERSITY of TWENTE

University of Twente
Department of Electrical Engineering
Telecommunication Engineering Group

Simulation of a ring resonator-based optical beamformer system for phased array receive antennas

by

Martin Tijmes

Master thesis
Executed from July 2008 to April 2009

Supervisor: prof.dr.ir.ing. F.B.J. Leferink
Advisors: dr.ir. A. Meijerink
dr.ir. C.G.H. Roeloffzen
dr.ir. M.J. Bentum
M. Burla, MSc

Summary

This thesis describes the development of a simulator tool that can be used in the field of RF photonics. The development has been performed on the basis of a broadband, continuously tunable ring resonator-based optical beamformer system for phased array receive antennas. The application that is considered in this thesis is airborne satellite reception of digital television.

An extensive description of the satellite receiver system is given, in which all the input-output relations of the individual components in the system are considered. It is shown that LabVIEW provides a good simulation environment for the application that is considered, which enables the specification of a suitable signal representation for both the electrical and optical domain. The simulator tool employs a fixed sample rate to circumvent the necessity for the laborious operations of up and downsampling.

Based on the discrete-time representation that is introduced, the models are implemented in LabVIEW. The simulation model comprises a dynamical implementation of the optical beamforming network (OBFN), such that beamforming can be performed for any number of antenna elements (AEs). The settings that are required for the delay elements in the OBFN are automatically generated, based on the time delay difference between individual AEs. The satellite signals and sky noise are modeled as well, to be able to use a realistic context to test the system and do performance evaluations.

The models of the individual components have been tested to match their theoretical responses. It is recommended to verify a full system simulation with theory, and later on compare with measurements.

The scalability of the model has been investigated by determining the computational complexity relations of the most critical blocks. It was shown that a simulation with more than 2,000 AEs, is likely to be performed within ten minutes.

The developed simulator tool appears suitable for applications in RF photonics in general, and can be used in continued work on optical beamforming. The performance of the beamformer is highly dependent on the calculated ring settings for the OBFN. Therefore, the simulated OBFNs are limited insofar that the required settings must be able to be determined.

Several recommendations are given to illustrate the usability of the simulator tool, and remarks are given on the extendability and increment of efficiency.

Contents

List of abbreviations

AE antenna element

BER bit error rate

BPF bandpass filter

CATV cable TV

CMBR cosmic microwave background radiation

CMOS complementary metal-oxide-semiconductor

CNR carrier-to-noise ratio

DC directional coupler

DSB double-sideband

DSB-SC double-sideband suppressed-carrier

DVB digital video broadcasting

DVB-S DVB-satellite

DVB-S2 DVB-satellite version 2

EMI electromagnetic interference

ETSI European Telecommunications Standards Institute

FSR free spectral range

IF intermediate frequency

ISI inter-symbol interference

LNA low-noise amplifier

LNB low-noise block

LO local oscillator

LPF low-pass filter

MEMPHIS Merging Electronics and Micro&nano PHotonics in Integrated Systems

MPEG Moving Pictures Expert Group

MZI Mach-Zehnder interferometer

MZM Mach-Zehnder modulator

OBFN optical beamforming network

OSBF optical sideband filter

ORR optical ring resonator

PAA phased array antenna

PCB printed circuit board

PSD power spectral density

PSK phase-shift keying

QPSK quadrature phase-shift keying

RAM random access memory

RIN relative intensity noise

RF radio-frequency

RoF radio-over-fiber

SANDRA Seamless Aeronautical Networking through integration of Data links, Radios, and Antennas

SMART SMart Antenna systems for Radio Transceivers

SNR signal-to-noise ratio

SSB single-sideband

SSB-SC single-sideband suppressed-carrier

RS Reed-Solomon

RTT roundtrip time

TE Telecommunication Engineering

TIA transimpedance amplifier

WDM wavelength division multiplexing

Chapter 1

Introduction

1.1 Background

In many applications, radio-frequency (RF) signals need to be transmitted and processed without being digitized. Copper cables do not always provide enough bandwidth to accommodate these signals. Optical fiber is a transmission medium in which RF-modulated optical carriers can be transmitted and distributed with very low loss, making it more efficient and less costly than conventional electronic systems, especially at high microwave and millimeter wave frequencies [1]. In literature this method is called radio-over-fiber (RoF). A schematic view is given in Figure 1.1.

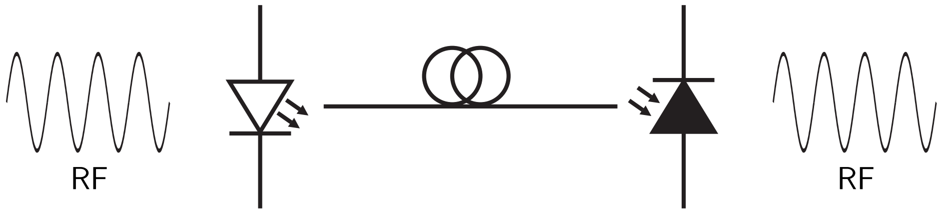

Figure 1.1: Radio-over-fiber (RoF)

When transporting RF signals over optical fibers, signal processing functions can also be performed in the optical domain, instead of the electrical domain. This has several advantages compared to the electrical domain, such as:

- compactness;
- light weight;
- large instantaneous bandwidth;
- low loss;
- inherent immunity to electromagnetic interference.

The main disadvantage is of course the conversion that has to made from the electrical to the optical domain and back, introducing noise and distortion. However, when the signal is already in the optical domain, many more processing functions can be preformed, such as high-frequency filtering, frequency conversion, optical distribution of RF clocks, antenna remoting, and beamforming for phased array antennas (PAAs). This area of research is called RF photonics and is one of the key research topics of the Telecommunication Engineering (TE) group at the University of Twente, The Netherlands [2].

Most of the RF photonics projects in the TE group are related to optical beamforming. This is described in more detail in the next section, as it will also be the main subject in this thesis.

1.2 Optical beamforming for phased array antennas

Within the TE group, research on the optical beamformer is part of ongoing work. In the past this work has been part of the SMart Antenna systems for Radio Transceivers (SMART) project, and is currently part of the Broadband Photonic Beamformer project, and the Merging Electronics and Micro&nano PHotonics in Integrated Systems (MEMPHIS) project. In the future this work will be continued in the Seamless Aeronautical Networking through integration of Data links, Radios, and Antennas (SANDRA) project [2]. In this thesis the SMART project is used to illustrate the application of optical beamforming, and therefore this section will go into more detail on this.

The SMART project was funded by SenterNovem, which is an agency of the Dutch Ministry of Economic Affairs promoting sustainable development and innovation [3]. The SMART project aimed at achieving global leadership of Europe in wireless markets and applications, by studying and developing a new generation of antenna systems dedicated to radio equipment for voice and data wireless networks [4]. A large group of companies participated in several consortia within the project. The TE group participated in a consortium based in the Netherlands, with its project partners LioniX BV, the National Aerospace Laboratory NLR, and Cyner Substrates.

Together with its project partners, the TE group developed an integrated radiation control technology, in which the development of a conformal aircraft array antenna serves as a pilot application. NLR was involved in researching the radiation pattern of an array antenna and the airborne regulations, as well as the design of broadband stacked patch antenna elements. Cyner Substrates is a manufacturer of printed circuit board (PCB) specials and worked on the fabrication of the antenna patch elements and feed lines. The TE group developed the optical beamformer concept, while LioniX worked on the realization of optical chips.

1.2.1 Phased array receive antenna

The reception of a satellite signal on the airplane occurs by means of a PAA. A PAA consists of a large number of small antenna elements (AEs) and is used to obtain the capabilities of a large mechanically steerable antenna. Both a mechanically steerable and a conformal PAA are shown in Figure 1.2.

A PAA has several advantages over a mechanically steerable antenna concerning gain, size and maintainability. For example, one can imagine that a mechanically steerable antenna might be inconvenient because of air drag. Additional to that are the possibility for beam-shaping, tracking and multi-beam reception. These last three advantages rely on the processing capabilities of the beamforming network and indicates its importance.

When discussing the reception of satellite signals on a moving aircraft (or other mobile platforms) there are two requirements that can be identified:

1. *continuous (or seamless) tunability*, to be able to receive the satellite signal from any direction;
2. *large instantaneous bandwidth*, to be able to receive broadband signals.

To satisfy these requirements the individual AEs should be broadband, but also the processing beamformer system should be able to realize true time delays for broadband signals, which can be tuned to any value in a (bounded) continuous range.

1.2.2 Optical beamformer

The beamformer system processes the signals from all AEs. The signal of each individual AE consists of a time-delayed version of some desired satellite signal, together with possible time-delayed versions of undesired signals. The specific time delay between the desired satellite signals depends on the geometrical distribution of the AEs and the direction of the incoming wave front. The beamformer system will subsequently delay all signals by the appropriate amount of time to synchronize all desired signals and obtain constructive interference by combining them; see Figure 1.3. It is called

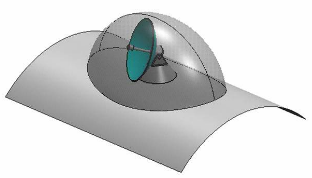

(a) Mechanically steered reflector antenna

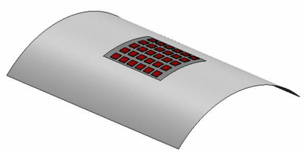

(b) Conformal phased array antenna

Figure 1.2: Receiving antenna on the plane fuselage

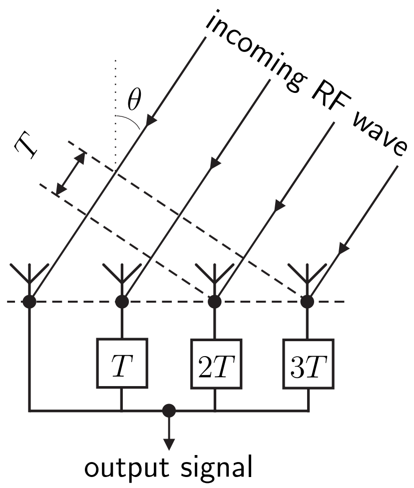

Figure 1.3: Beamforming operation for a phased array antenna (PAA)

beamsteering when only the delays are tunable and beamforming when additional to the delays the amplitudes of the AE signals are tunable as well. This last property is called amplitude tapering and may give rise to a better performance by the suppression of sidelobes in the beam pattern, which suppresses the received interference.

For narrowband systems it is possible to delay signals by means of a phase shifter. However, for broadband systems this will result in a frequency-dependent beam angle and shape (beam squint). By using switchable delay matrices the appropriate amount of delay can be generated, but only for a *discrete* number of angles. Switchable delay matrices show a trade-off between beam angle resolution and complexity.

In the optical domain *continuously* tunable delays can be realized over a large bandwidth by means of optical ring resonators (ORRs), thereby satisfying the desired properties mentioned in Section 1.2.1. This will be explained in more detail in Section 2.5.1. These properties together with the general advantages of optical processing mentioned in Section 1.1 make it very advantageous to implement the beamformer system in the optical domain.

1.2.3 Previous work on optical beamforming

The work on optical beamforming in the TE group started with tunable optical delay lines by means of ORRs. In [5] it has been shown that a continuously tunable delay can be realized over a large bandwidth. Using CMOS-compatible LPCVD waveguide technology, the tunable delay lines can be integrated on chip with low losses [6–8].

The advantages of the LPCVD waveguide technology and the possibility for continuous tuning of optical delay lines gave perspective for the full integration of multiple optical delay lines and combiners to a form an optical beamforming network (OBFN).

In [9] and [10] single-chip OBFNs have been demonstrated with respectively four and eight inputs. The development of the optical beamformer chips has been continued in perspective of the PAA application with respect to system level aspects [11–14].

To employ the optical beamformer to its full extent, research has been performed on optimal delay tuning algorithms, optical phase synchronization, and the usage of single-sideband (SSB) modulation [15–21]. To determine how well an optical beamformer performs compared to its electrical equivalent and to locate any bottlenecks, a performance study has been done for PAA satellite receiver systems, using an ORR-based beamformer [22]. In the SMART project an experimental demonstrator has been built, consisting of an 8-port beamformer for an 8×8 PAA [4].

However, there is still a lot of research that can be done. For example, in the final design the optical beamformer should have more that 1,600 inputs, but in the development of the single-chip beamformers it is hard and costly to upscale the number of inputs. Therefore, it would prove advantageous to have another means to investigate the performance of beamformers with a large number of inputs. Furthermore, the performance of the total system must be investigated in more detail. Especially for more complex systems, a lot of approximations must be made to be able to derive any analytical results. Moreover, the results depend on a great number of system parameters, and the way in which a particular parameter has an impact on the performance measures is not always obvious. By using simulations, a lot of these issues can be investigated.

1.3 The benefits of simulation

Simulation is often used in research and offers a lot of advantages. The most important advantages are [23]:

- The simulation results can be used to verify the results of the analyses. By means of the simulation results it can be checked whether any mistakes in the derivations have been made and whether all mathematical approximations are accurate;
- Especially in the case of complicated systems, models are often greatly simplified in order to facilitate theoretical analysis, resulting into inaccuracies of analytical results. These inaccuracies can be identified by running simulations on more advanced models;
- In cases where random processes play an important role, simulations can provide a good way of visualizing the actual signals that are involved. In this way, a simulation can enhance the understanding of system concepts. Furthermore, it can help identify noise effects and understand the influence of noise, since these are often random processes as well;

- Theoretical analysis may in some cases be a more time-consuming procedure than simply running a short simulation. Therefore, simulation can in some cases be a good way of quickly obtaining a first impression about a new system concept;
- Comparing the results from actual measurements on components with the simulation results can be helpful in checking fabricated devices, whether they are faulty or not. Also, it can help to locate errors or sources of phenomena that occur during measurements, and to verify the results;
- A simulation can easily be used for a demonstration. It can both show a proof of concept as well as help visualizing a complete system concept. Additional to that, simulation can be a cost-reducing method since no practical demonstrators have to be built, which can be quite expensive.

The advantages mentioned above, already make it interesting to investigate the usage of a simulator tool for the work on optical beamformers done in the TE group. Additional to that, does the previous work on this subject —discussed in Section 1.2.3— give rise to extra motivation for using simulation in the line of research that is conducted.

Using simulation, more detailed models can be used to evaluate the system and investigate the performance measures. Furthermore, simulation allows for easy scaling of the model and offers the possibility for investigation of a *real-size* system model. Therefore, with the advantages of a simulator the issues mentioned in Section 1.2.3 can be overcome.

1.4 Assignment goal

The goal of this assignment is to investigate and develop a *suitable simulator tool* that can be used in the field of RF photonics. This simulator tool should be able to study the performance of the optical beamformers that are and will be developed in the TE group. Furthermore, it is interesting to know to what extent it is possible to simulate *real-size* systems and what limitations are encountered in the simulator.

The pilot application that will be used to build the simulator tool is the reception of satellite signals on aircraft, which was part of the SMART project discussed in Section 1.2, is currently studied in MEMPHIS and will be part of the SANDRA project. From this application the most important requirements will result that can be generalized to other RF photonics applications and applied for research in those areas.

1.5 Report outline

In Chapter 2 we begin with describing the application of satellite reception on aircraft in more detail. Next, the description of the requirements for the simulator tool, as well as the signal representation are discussed in Chapter 3. The modeling of the total system explained in Chapter 2 is split into two chapters. In Chapter 4 the modeling of the optical beamformer is described, whereas in Chapter 5 the context is discussed, concerning the generation and reception of the satellite signal, as well as the demodulation and detection of the signal after beamforming. The time complexity and upscaling of the model are subject of Chapter 6. Finally, in Chapter 7 the conclusions and recommendations are given.

Chapter 2

System overview

In this chapter the SMART receiver system will be discussed. A functional overview is given in Figure 2.1. All the blocks will be discussed separately showing the functionality of the block and an analytical description of the input-output relation, to be able to model them in Chapters 4 and 5. The signal description that is used will be discussed in more detail in Chapter 3. Throughout this chapter, the signal spectrum for each block will be given to enhance the understanding of the operations performed on the satellite signal, as well as a mathematical signal description

2.1 Satellite signal

In this report we will focus on the reception of digital television on aircraft, by means of digital video broadcasting (DVB). DVB is an international standard for digital television. There are several standards for satellite reception (DVB-S), terrestrial television (DVB-T), cable (DVB-C) and others [24]. In the SMART project the satellite standard is used for airborne satellite reception, which uses phase modulation through quadrature phase-shift keying (QPSK). A newer version of the standard (DVB-S2) allows modulation using both amplitude and phase, including QPSK, 8-PSK, 16-APSK and 32-APSK.

After the DVB-S signal is received at the satellite from a ground station, it is converted to a different frequency, amplified per transponder and re-transmitted back to earth. The satellites are geo-stationary and are located 36.000 km above the Earth's

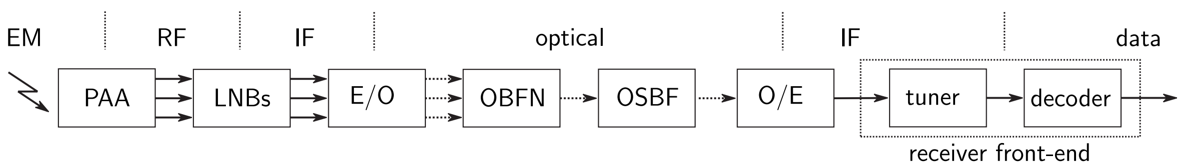

Figure 2.1: System overview

equator. Geo-stationary satellites appear to be fixed from an Earth point of view. Satellite television is typically transmitted in the C band (4–8 GHz) or K_u band (11–18 GHz). C-band transmission is more susceptible to terrestrial interference, while K_u-band transmission is affected by rain (also called rainfade). In this thesis satellite communication in the K_u-band will be considered.

Two polarizations are used within the K_u band (vertical and horizontal). The allocated spectrum for downlink (satellite to Earth) transmission is 10.7–12.75 GHz, and contains both television and radio broadcasts. The total spectrum is provided by a group of satellites, which are seen as a single source from earth [25, 26]. By directing the antenna to different angles, different groups of satellites can be selected, which reuse the frequency spectrum. The frequency range is subdivided into frequency slots of 26 to 36 MHz, and guard bands of at least 4 MHz. The frequency slots in the horizontal and vertical polarization are staggered, meaning that a slot for one polarization is placed in the guard band of the other polarization, as shown in Figure 2.2.

Considering a single polarization and ignoring noise and interference, the normalized field of the desired signal can be written as a bandpass signal consisting of a set of N subcarriers

$$s(t) = \sum_{n=1}^{N} r_n(t) \cos\Big(2\pi f_{\mathrm{RF},n} t + \psi_n(t)\Big), \tag{2.1}$$

which is defined such that the square of the amplitude is equivalent to the instantaneous power received by an isotropic antenna. The transmitted information is in the time-varying amplitude $r_n(t)$ and phase $\psi_n(t)$. For DVB-S, each carrier n corresponds to one of the N transponders. There is only one carrier per transponder, to avoid intermodulation distortion when the signals are amplified in the satellite. In DVB-S2, there may be more carriers per transponder.

2.2 Phased array antenna

The PAA is mounted on top of the fuselage of the aircraft, as shown in Figure 1.2(b), and will receive the DVB-S signal. Each AE m will receive a version of the DVB-S

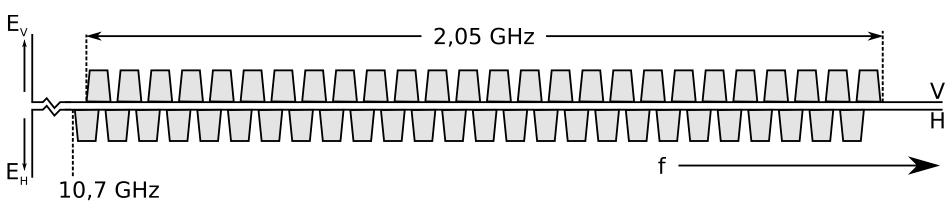

Figure 2.2: Frequency allocation with staggered slots. Each polarization consists of 60 slots.

signal $s(t)$, that is delayed by τ_m and can be written as a voltage

$$v_{\mathrm{AE},m}(t) = \sqrt{Z_{\mathrm{c}} G_{\mathrm{AE}}} \sum_{n=1}^{N} r_n(t-\tau_m) \cos\Big(2\pi f_{\mathrm{RF},n}(t-\tau_m) + \psi_n(t-\tau_m)\Big), \tag{2.2}$$

where Z_{c} is the characteristic impedance of the transmission line and G_{AE} the gain of the AE in the direction of the satellite signal. Note that the gain G_{AE} will differ for each AE when the surface is not flat, but conformal to some surface. The beamformer system will have to compensate for this, but that is not considered in this thesis. Therefore, the delays can be considered constant.

For two adjacent AEs on a *flat* PAA, the difference in time delay $\Delta\tau$ is calculated by

$$\Delta\tau = \frac{d \sin(\theta)}{c}, \tag{2.3}$$

where d is the distance between the AEs, c the speed of light and θ the deviating angle from broadside (see Figure 1.3).

Recall that geostationary satellites are located directly above the equator. Since airborne satellite reception should be possible at circles of latitude near the North Pole and South Pole, there should be sufficient performance under low elevation angles. The requirements are set such that reception angles from $-60°$ to $+60°$ should be possible. As the spacing for $\mathrm{K_u}$-band satellites can be as small as a few degrees [25], a small beamwidth (4.1°) as well as a high gain (32 dB) are required [27].

The AEs are microstrip patch elements, which are relatively inexpensive to manufacture and design. Patch elements are more or less omnidirectional and provide a gain of a few dBi. Using an array of patched elements can increase the gain largely while retaining its low profile, and is therefore suitable for and common on airplanes [28]. Inherent to patch elements is a low bandwidth, but this can be increased sufficiently using a stacked layout. The radiation pattern for a stacked patch antenna is shown in Figure 2.3 and shows a gain of about 9 dBi [29]. An advantage inherent to patch elements is the ability to have polarization diversity, which is very convenient for the horizontally and vertically polarized satellite signal, depicted in Figure 2.2.

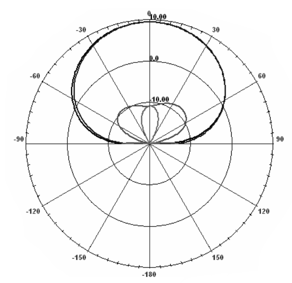

Figure 2.3: Beam pattern of a stacked $\mathrm{K_u}$-band patch antenna

2.3 Low-noise block

After reception by the PAA, the signal of each AE is bandpass-filtered and downconverted to intermediate frequency (IF) (950–2150 MHz) by a low-noise block (LNB). An LNB is a low-noise amplifier (LNA) in combination with a downconverter, using a local oscillator (LO), as shown in Figure 2.4. The IF range enables transmission to the tuner through a relatively low-cost coaxial cable. Higher frequencies (above 2150 MHz) would lead to an unacceptable high level of attenuation, and the range under 950 MHz is reserved for possible transmission of terrestrial cable TV (CATV) signals through the same cable.

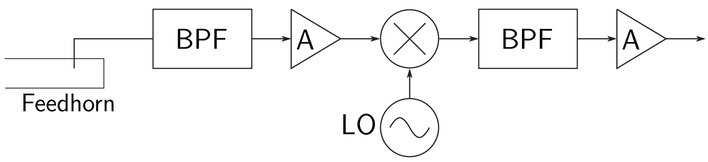

Figure 2.4: Block diagram of LNB after polarization decoupling

Since the bandwidth of the RF signal (2.05 GHz) is larger than the IF bandwidth (1.2 GHz), only part of the received signal can be transmitted. Therefore, two different mixing frequencies are used to select the upper or lower part of the RF signal band (either horizontally or vertically polarized). These mixing frequencies are 9.75 and 10.6 GHz, which select respectively the frequency ranges 10.7–11.9 and 11.55–12.75 GHz. The frequency ranges inhibit some overlap as a result of a larger IF bandwidth (1200 MHz) compared to half of the RF bandwidth ($(12.75 - 10.7)/2 = 1.025$ GHz). Thus within the total received spectrum, four parts of the total signal band can be distinguished. The signal spectrum after the LNB is shown in Figure 2.5.

The signal that is transmitted through the coaxial cable after filtering can be written as a voltage

$$\begin{aligned} v_{\mathrm{LNB},m}(t) = &\sqrt{Z_\mathrm{c} G_\mathrm{AE} G_{\mathrm{LNB},m}} \\ &\cdot \sum_n r_n(t-\tau_m) \cos\Big(2\pi f_{\mathrm{IF},n}(t-\tau_m) - 2\pi f_\mathrm{LO}\tau_m + \psi_n(t-\tau_m)\Big), \end{aligned} \tag{2.4}$$

where G_LNB denotes the gain of the LNB. Each subcarrier n denotes one of the frequency slots shown in Figure 2.5.

2.4 E/O conversion

After downconversion and amplification, the signals are converted to the optical domain to perform the beamforming operation.

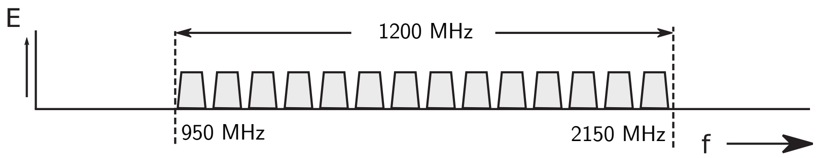

Figure 2.5: Signal spectrum after the LNB

The electrical signals are modulated onto an optical carrier by means of an MZM. The optical carrier is produced by a single laser and is split up into the number of AEs, by means of directional couplers (DCs). Then the signals $v_{\mathrm{LNB},m}(t)$ from the LNBs are used to externally modulate the carriers.

2.4.1 Laser

Using a scalar wave representation, the laser output can be described in the amplitude and phase form by [22, Sec. 4.4.3]

$$E_{\mathrm{o}}(t) = \sqrt{2P_{\mathrm{o}}(t)}\ \exp\Big(\mathrm{j}2\pi f_{\mathrm{o}}t + \mathrm{j}\phi_{\mathrm{o}}(t)\Big), \tag{2.5}$$

such that the instantaneous power is equal to

$$P_{\mathrm{o}}(t) \triangleq \frac{1}{2}\left|E_{\mathrm{o}}(t)\right|^2. \tag{2.6}$$

The laser signal will be generated with a constant optical power. However, due to relative intensity noise (RIN) and phase noise some fluctuations will appear in the optical signal. In [22] it was found that for the system under consideration the phase noise and RIN can be neglected. Therefore, the laser signal can be described by

$$E_{\mathrm{o}}(t) = \sqrt{2P_{\mathrm{o}}}\ \exp(\mathrm{j}2\pi f_{\mathrm{o}}t), \tag{2.7}$$

2.4.2 MZM

A schematic view of an MZM is given in Figure 2.6(a). The MZM consists of two DCs, interconnected by two branches whose refractive index can be changed by applying a voltage, using the electro-optic effect. The voltage is applied to an electrode in between the two branches, resulting in fields over the branches that are in *opposite* direction. Hence, it is said to operate in push-pull mode. The field-direction dependent electro-optic effect minimizes any phase distortion, thereby enabling chirp-free modulation.

The transfer function of the MZM is given in Figure 2.6(b) and shows the transfer of both power and field. When looking at the power transfer, the MZM is normally operated in quadrature ($\Delta V/V_{\pi,\mathrm{DC}} = 0.5$) to obtain an approximately linear transfer. However, since we want to convert the phase to amplitude modulation we need the transfer of the *field* to be linear. For small modulating signals the transfer of the

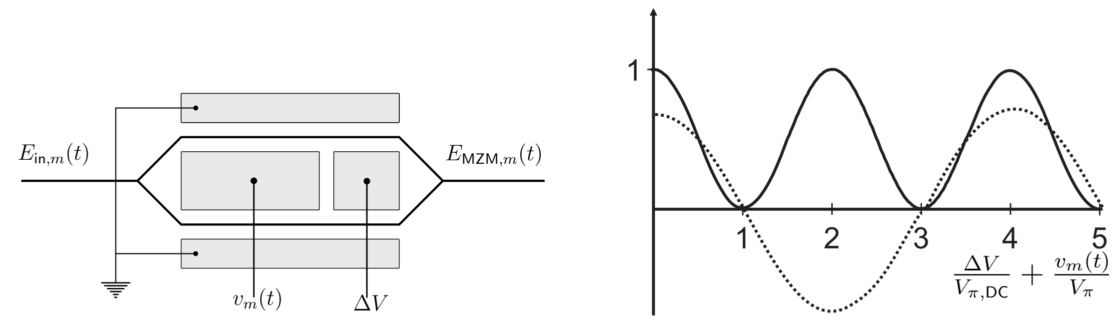

(a) A schematic view of an MZM in push-pull [30]

(b) Transfer function of MZM. The solid line indicates the power transfer, whereas the dotted line indicates the field transfer. The MZM is biased in a point where $\Delta V/V_\pi$ is odd, to obtain a linear field transfer.

Figure 2.6: The Mach-Zehnder modulator (MZM) and its transfer function

field is approximately linear when $\Delta V/V_{\pi,\text{DC}}$ is odd. When the modulation depth is increased more non-linear distortion will occur. Since the biased operating point has a zero power and field transfer the carrier is suppressed, as well as even higher order terms, and the modulation results in double-sideband suppressed-carrier (DSB-SC) [20]. Note that this is the case for an ideal MZM, having equal branches, and describes the model that will be used throughout this thesis. A more complex model can be used later on if proven necessary.

The output optical signal from the MZM in branch m can be shown to be [22]

$$E_{\text{MZM},m}(t) = \frac{1}{2\sqrt{L_\text{x}}} \left[H_{\text{PM},m}(t) + H^*_{\text{PM},m}(t) \right] \; E_{\text{in},m}(t), \tag{2.8}$$

where $E_{\text{in},m}(t)$ is the optical laser signal to be modulated, L_x the excess loss, and an inherent splitting and combining loss of $\sqrt{2}$ has been taken into account. The typical excess loss of an MZM is known to be 3–5 dB, resulting from the fiber-waveguide coupling. The transfers in the branches are $H_{\text{PM},m}(t)$ and its complex conjugate, and are given by

$$H_{\text{PM},m}(t) = \exp\left(\text{j}\, \frac{\pi v_m(t)}{2V_\pi} + \text{j}\, \frac{\pi \Delta V}{2V_{\pi,\text{DC}}} \right). \tag{2.9}$$

When assuming a small modulation depth ($v_m(t) \ll V_\pi$), the transfer of the MZM can be approximated to be linear around the bias point and there will be no higher order harmonics. In this case the optical signal of the IF signal that has been modulated on the optical carrier is shown in Figure 2.7. The width of both sidebands is equal to the IF signal bandwidth, but the total signal bandwidth is larger and equals 4300 MHz.

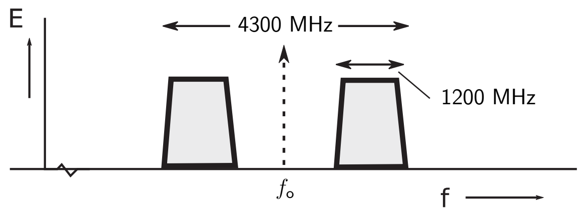

Figure 2.7: Signal spectrum after the MZM with a suppressed carrier (dotted line). The transfer is the MZM is considered linear, such that there are no higher order harmonics. For a wavelength of 1550 nm, the optical frequency f_o equals 194 THz

2.5 Optical beamforming network

Within the OBFN all branches are delayed by the appropriate amount of time to synchronize all signals. The delay elements are ORRs and are discussed next. Subsequently, the network structure is discussed.

2.5.1 Optical ring resonators

In the waveguide realization, an ORR consists of a straight waveguide and a recirculating waveguide coupled parallel to it. The coupling section is in fact a directional coupler (DC). This is illustrated in Figure 2.8. An ideal lossless ORR acts as an optical all-pass filter, which is characterized by a unity magnitude response. It has a periodic group delay response, which represents the *effective time delay* to the RF signal that is modulated on the optical carrier.

After injecting a light pulse into the optical waveguide of the ORR a certain amount of the light is coupled into the ring, while the remainder is passed through. After a single roundtrip time (RTT) T a certain amount of light is coupled out of the ring into the straight waveguide, and the remainder goes for another roundtrip. The amount of power that is coupled into or out of the ring is the determined by the power coupling

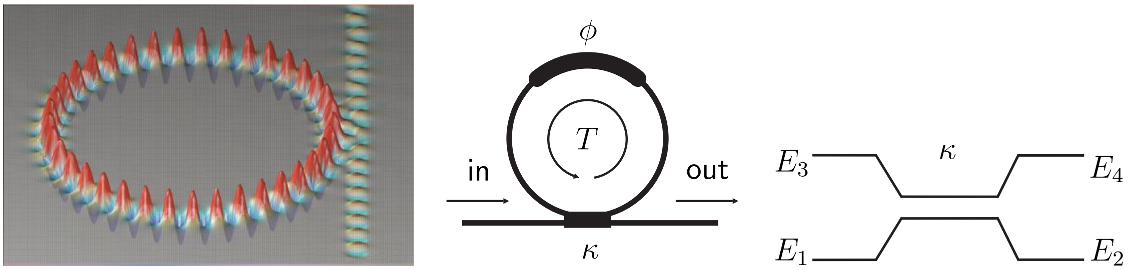

(a) Theoretical wave propagation in an ORR (b) Schematic view of an ORR with RTT T (c) Schematic view of a directional coupler (DC)

Figure 2.8: Optical ring resonator (ORR)

coefficient κ. The transfer of the DC is given by

$$\begin{bmatrix} E_4 \\ E_2 \end{bmatrix} = \begin{bmatrix} \sqrt{1-\kappa} & -\mathrm{j}\sqrt{\kappa} \\ -\mathrm{j}\sqrt{\kappa} & \sqrt{1-\kappa} \end{bmatrix} \begin{bmatrix} E_3 \\ E_1 \end{bmatrix}. \tag{2.10}$$

With ϕ an additional phase shift is added to the ring. The parameters κ and ϕ are tuned by voltage-driven heaters that use the thermo-optic effect to change the refractive index of the waveguide.

Since it will take an amount of time equal to the RTT for light to come out each time, it can be concluded that the impulse response of the ORR is discrete, as shown in Figure 2.9(a). This results in a periodic phase and group delay response that is repeating every free spectral range (FSR), which equals $1/T$. The group delay response is found by differentiating the phase response and is given by [5]

$$\tau_{\mathrm{g}}(f) = \frac{\kappa T}{2 - \kappa - 2\sqrt{1-\kappa}\,\cos(2\pi f T + \phi)}. \tag{2.11}$$

Within one FSR of the group delay response a peak is centered at the resonance frequency. The peak value and the position of the peak are determined by the parameters κ and ϕ, respectively. However, the peak value of the delay is more or less inversely proportional to the peak width. This is because the phase transition within one FSR is constant (2π), and thus the area underneath the delay curve is constant as well (unity). Hence, there is a inherent trade-off between the peak delay value and the width of the peak, which is shown in Figure 2.9(b) [5, 6].

For a broadband RF signal a single ORR may not provide enough delay bandwidth. When multiple ORRs are cascaded their individual group delay responses can be superposed to form a response with sufficient bandwidth. By tuning the rings properly a response with a flattened delay band can be achieved, shown in Figure 2.10. However, by increasing the number of rings to minimize the delay ripple, the tuning complexity increases. Hence, there is a trade-off for multi-ring delay sections between peak delay, bandwidth, delay ripple and the number of rings [5, 6].

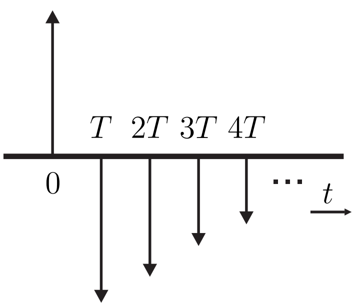

(a) Impulse response ORR

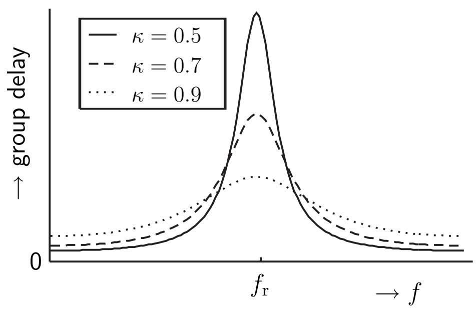

(b) Group delay ORR, showing a trade-off between peak height and width

Figure 2.9: Optical ring resonator (ORR) characteristics

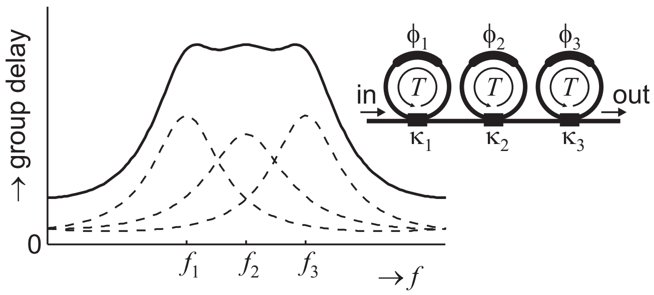

Figure 2.10: Individual and combined group delay responses of three cascaded optical ring resonators

2.5.2 Network structure

The OBFN has a binary tree structure to reduce the system complexity, opposed to a parallel delay line structure. In Figure 2.11 an example of an 8×1 OBFN structure is shown. The signals from the various branches are combined using DCs.

Within the TE group several prototypes of an OBFN chip have been developed and tested [9, 10]. In Figure 2.12 the measurement results of a 1×8 OBFN chip are shown, that has been fabricated using a CMOS-compatible optical waveguide technology [31].

In each stage, every two branches are combined coherently, to obtain constructive interference. For this to occur, the optical phases of both branches must be aligned. An optical phase shifter is added to the upper branch for each pair (ϕ_{13}–ϕ_{19} in Figure 2.11). In [19] an optical phase synchronization method has been developed, based on the output power of the beamformer, that operates with a feedback loop.

The losses that are introduced in the OBFN mainly originate from the propagation losses in the optical waveguides. The losses introduced by the DCs and ORRs are

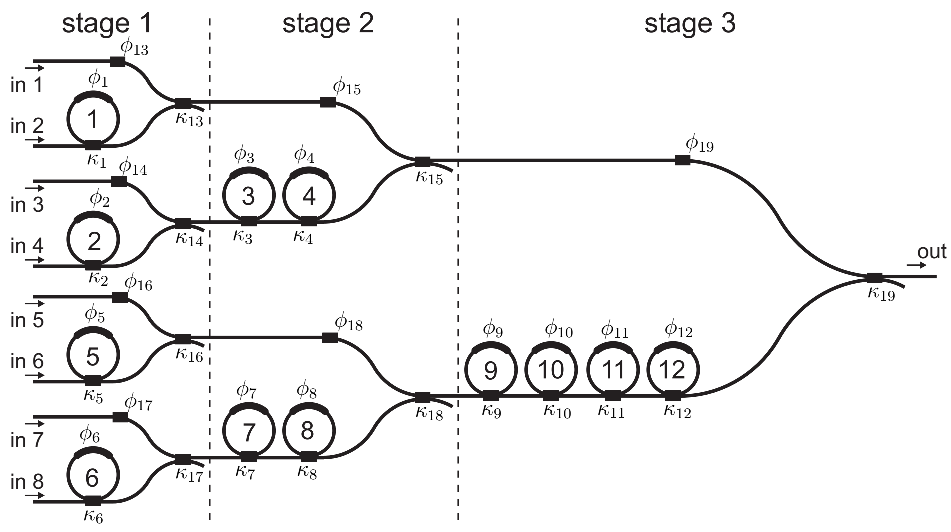

Figure 2.11: An optical beamforming network (OBFN) with a binary tree structure consisting of 8 inputs and 1 output

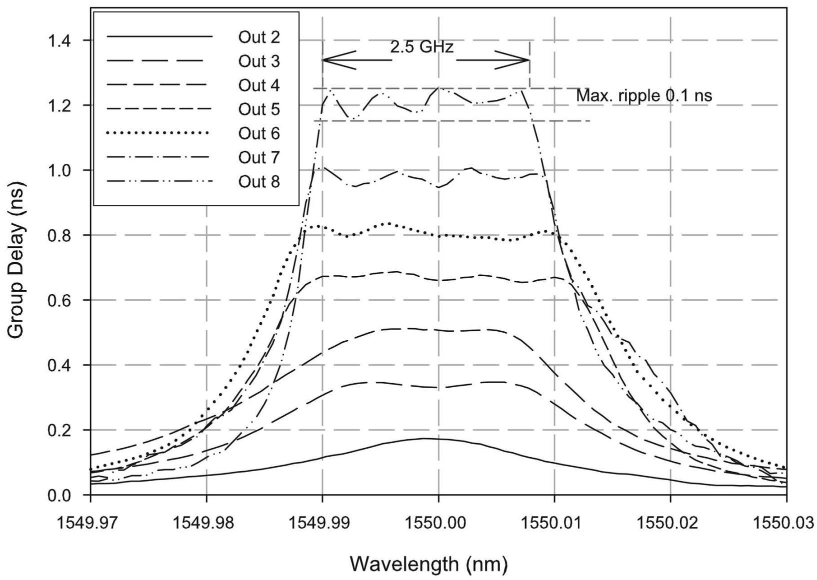

Figure 2.12: Measurement results showing the linearly increasing delays per outputs of the 1×8 OBFN chip

smaller and can be neglected. This will be discussed in more detail in Section 4.1.

2.6 Optical sideband filter

In Section 2.5 we have discussed the trade-off for multi-ring delay sections between peak delay, bandwidth, delay ripple, and the number of rings. Therefore it is desirable to have a modulating signal that has a bandwidth that is as small as possible. The IF signal (950–2150 MHz) has a bandwidth of 1200 MHz. However, when the signal is modulated onto the optical carrier using double-sideband (DSB) modulation, the total signal bandwidth is 4300 MHz (2×2150 MHz). By removing one of the sidebands, the bandwidth is reduced by half and is only 2150 MHz. Recall that the MZM is biased in a point where the carrier is suppressed, thus actually the signal is modulated using DSB-SC instead of DSB. Now, the remaining bandwidth equals the signal bandwidth (1200 MHz). The optical signal spectrum is shown in Figure 2.13(a).

A reduced signal bandwidth relieves the constraints on the OBFN somewhat. Since a smaller number of rings can be used to accommodate the smaller bandwidth, the complexity of the beamforming network is reduced. Since only one of the sidebands was synchronized correctly in the OBFN, the faulty one will be removed by means of the OSBF.

The OSBF consists of an asymmetric MZI with an ORR in its shortest arm, where the circumference of the ORR is twice the difference in length between the arms; see Figure 2.13(b). This results in the FSR of the ORR being half the FSR of the MZI,

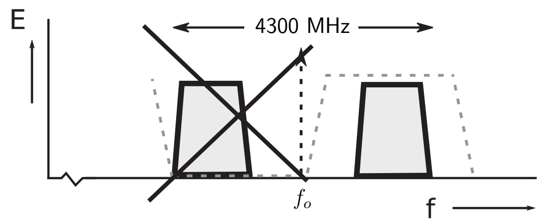

(a) Optical signal spectrum, with sideband and carrier removal

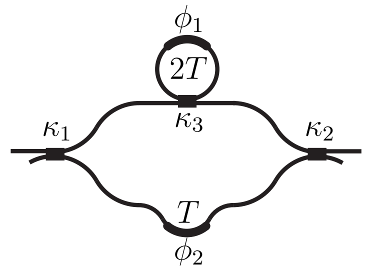

(b) OSBF, consisting of an asymmetric MZI with an ORR in one of its arms

Figure 2.13: Optical sideband filter (OSBF)

and can be seen in Figure 2.14. Compared to a normal asymmetric MZI (without an ORR) a more flat and broader passband can be obtained, which is necessary for leaving the signal bandwidth unattenuated. A maximally flat passband is obtained if the slope of the upper arm equals the slope of the lower arm [32].

2.7 O/E conversion

After the beamforming operation, the optical signal must be converted back to the electrical domain. The optical detection is performed by photodiodes, which convert light intensity into a current. Since the carrier of the signal is suppressed to reduce the bandwidth and obtain a linear transfer from the modulating signal to the field, we can only use coherent detection. Therefore, the optical carrier has to be reinserted before detection, as shown in Figure 2.15.

Detection of the information signal is done in a balanced-differential detection

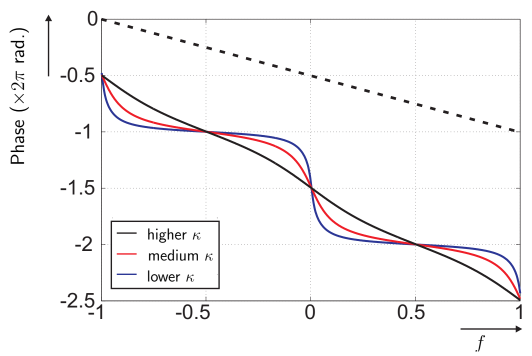

Figure 2.14: OSBF phase response of the lower arm consisting of the delay line over 1 FSR (dotted line), and the upper arm with the ORR over 2 FSRs (solid lines). By means of the ring parameters κ and ϕ the phase response of the upper arm can be tuned.

scheme. As a result of this scheme we will directly obtain the modulating signal itself without any direct-current term from the optical carrier, and the effect of RIN will be reduced [33]. After detection, the current is converted to a voltage by means of a TIA, which is not shown in Figure 2.15.

After the carrier has been reinserted by the DC, both outputs of the DC consist of a superposition of both input signals and an intermodulation term. The mixing terms in both outputs are in anti-phase. After subtraction of the detected photodiode currents, only the mixing term remains and the other terms are canceled. The resulting spectrum will equal the IF spectrum shown in Figure 2.5, when there is no distortion and noise introduced.

When we are omitting the shot noise, the detected photocurrent I_p can be written as

$$I_\mathrm{p}(t) = R_\mathrm{pd}\, [P_{\mathrm{pd},1}(t) - P_{\mathrm{pd},2}(t)], \tag{2.12}$$

where R_pd is the responsivity of the photodiodes and the power received by the photodiodes $P_{\mathrm{pd},x}$ equals the optical power

$$P_{\mathrm{pd},x}(t) = \frac{1}{2}\left|E_{\mathrm{pd},x}(t)\right|^2. \tag{2.13}$$

Using the TIA, the current is converted to the output voltage

$$V_\mathrm{out}(t) = -Z_\mathrm{TIA}\, I_\mathrm{p}(t), \tag{2.14}$$

where Z_TIA is the transimpedance of the amplifier. Normally, the TIA is put in cascade with a buffer that has unity gain to realize a matching output impedance, as shown in Figure 2.16 [34].

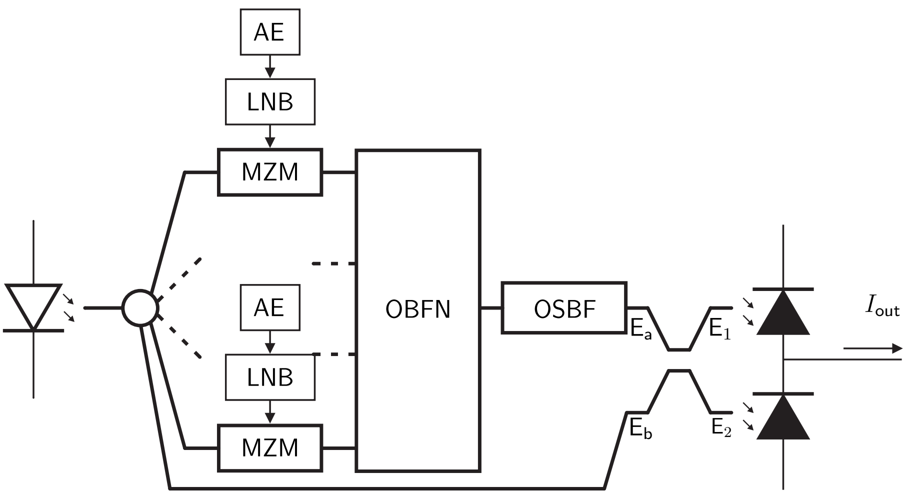

Figure 2.15: Carrier reinsertion for coherent detection

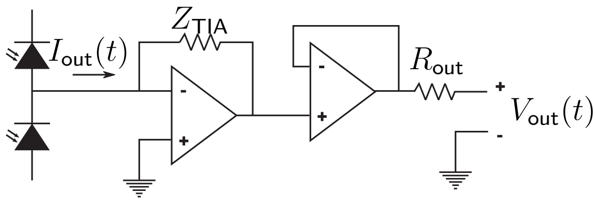

Figure 2.16: Transimpedance amplifier and buffer

2.8 Receiver front-end

The modem consists of a tuner and a decoder for the QPSK signal, as shown in Figure 2.17. In the tuner one of the slots of the DVB band shown in Figure 2.2 is selected using a tunable LO. Subsequently, the signal is bandpass-filtered at a fixed center frequency of 479.5 MHz with a passband width of 33 MHz.

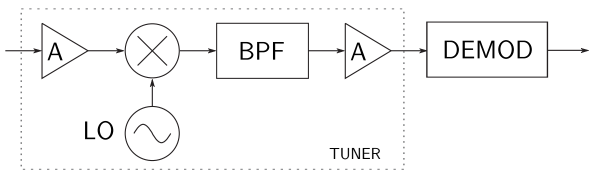

Figure 2.17: Block diagram of the tuner with the demodulator attached to it

The decoder essentially reverses the processing steps that were carried out in the encoder at the transmitting end. Tasks executed in the decoder include [35]:

- QPSK demodulation;
- equalization by a matched filter;
- depuncturing;
- Viterbi decoding;
- de-interleaving;
- Reed-Solomon (RS) decoding.

For practical purposes off-the-shelf modems can be used, that consist of both a tuner and a decoder. This holds for the DVB-S standard, as well as newer standards that use 8-PSK, 16-APSK and 32-APSK, instead of QPSK.

2.9 Summary

Throughout this chapter, all building blocks of the SMART receiver system have been discussed. For each block the signal spectrum has been given to clarify the operations performed on the DVB signal, throughout the system.

The system can be split up in an electrical and optical part, where the optical part can be characterized with the beamforming operation. First, the DVB signals received by the satellite are downconverted to IF. Then the IF signal is converted to the optical domain by means of single-sideband suppressed-carrier (SSB-SC) modulation, using an MZM with carrier suppression and an OSBF. A modulation scheme such as SSB-SC relaxes the constraints on the OBFN. Finally, the beamforming operation is performed by means of ORRs on an optical signal bandwidth, equal to the IF bandwidth. Using a balanced detection method to convert the signal back to the electrical domain, the RIN is suppressed. The final step is the decoding of the signal, after selection of the desired subcarrier.

Chapter 3

Simulation environment and signal representation

In this chapter a suitable simulation environment will be selected, based on several requirements that result from the SMART project and the field of RF photonics. After the selection of the software, a signal representation will be introduced for both the continuous and discrete domain.

3.1 Choice of the simulation software environment

Before building the simulator tool, a practical simulation environment must be chosen to develop the tool in. Based on the requirements for the simulator tool and considerations concerning optical signals, a certain software package is chosen.

3.1.1 General requirements

The requirements must hold for systems being developed in the field of RF photonics, as mentioned in Section 1.4. The beamformer system discussed in Chapter 2 is used to characterize these requirements. A number of qualitative requirements for the simulator are listed and discussed next.

Performance evaluation capabilities

Each system has certain performance requirements. To know whether these requirements are reached or not, the system must be characterized. Common performance metrics are the bit error rate (BER), the carrier-to-noise ratio (CNR) and the E_b/N_0 (SNR per bit). In the evaluation of a system, a good provision or easy implementation of these performance metrics can help substantially.

Automated and interactive control of simulation

Automated control can be used to execute the simulation using a parameter sweep, or running adaptive iterative simulations based on previous results. For large batches of simulations it is useful that parameters and settings can for example be read from text files or be based on a smaller set of settings, requiring no further intervention of human control. Furthermore, it is desirable to be able to change some of the controls and parameters interactively during execution.

Exportability of data and results

Exportable data is convenient to easily process results and use them for analysis of the system. It is beneficial if common standards such as comma-separated text files or other delimiter-separated files can be used for this purpose, such that many applications can be used for the processing. Furthermore, export of vector graphics is beneficial for the visualization of results and easy processing in reports.

Acceptable cost and availability

The simulation software should have an acceptable cost, such that the costs justify the means. It is equally important that the software package should be well available, in order to minimize any latency in the execution of the modeling process, and has sufficient support to resolve any problems or bugs that might occur.

Animation and user interface

To support the adoption of the simulation environment, a good user interface is essential. This helps understanding ongoing modeling and simulation work in a more flexible way. Also, animation is very supportive during the design process and evaluation of the model.

Compatibility with other simulation software and hardware

In research, many different tools and means are used for modeling and evaluation of systems. The possibility for interfacing with other simulation software can be advantageous to combine research work. Furthermore, in some cases it can be advantageous to implement certain parts of a model using another programming language such as C or assembly.

Compatibility with hardware leads to advantages of co-simulation. With co-simulation we are able to use experimental hardware demonstrators as part of a larger system that is simulated and tested.

Real-time simulation

Especially in the case of co-simulation it is desirable that the simulator adapts quickly to changing parameters. In order to do this, tasks must be prioritized such that the most critical tasks can always take control of the processor. This has the advantage that, during a simulation, specific building blocks can react immediately on an event, such as renewed input variables, while other non-critical building blocks can be delayed in execution. Note that real-time performance does not necessarily increase the execution speed of the program, but it actually enhances the application by providing more predictable timing characteristics.

Cross domain signal representation

A more specific requirement for the modeling of RF photonic systems, is the need for cross domain signal representation. Within the same simulation environment it should be possible to support both electrical and optical signals.

Optical signal representation

Another specific requirement for the simulation of RF photonics systems, covers the optical signal representation. A lot of optical systems being worked on in the TE group, particularly in the SMART project, cover *coherent* optical systems. In order to simulate these systems correctly, the simulator should be able to work with interference-based models. This means that optical signals should not just be represented by their power equivalent, but the calculations in the simulator must consider the optical phases as well.

3.1.2 General purpose versus dedicated software

In selecting a simulation environment, there are three approaches that can be considered:

1. Dedicated simulation software, specifically designed for optical and/or electrical systems;
2. General purpose simulation software, designed for multidomain systems;
3. Self-built simulation software, specifically designed for RF photonics and the application at hand.

The most easy approach is to take a *dedicated* software package that can be used to implement the model. However, most commercially available dedicated software packages are not able to handle signals from both the electrical and optical domain. Furthermore, most optical simulation environments are not suitable for coherent optical systems, since they are based on power equivalent signal representations. This limits the choice for a good commercial dedicated software package.

Another approach is to develop your own software from scratch, specifically designed for RF photonics and the applications mentioned in this thesis. This requires, however, a deep understanding of a suitable programming language and the model needs to be constructed from very basic blocks.

A middle course is use a general purpose simulator. With this software it is possible to use the correct signal representation in both domains. Both LabVIEW [36] and Matlab Simulink [37] are examples of such simulation software. A self-specified representation of signals can be used and there is a lot of freedom in the modeling of components. The disadvantage is, however, that more basic building blocks must be used, compared to dedicated software.

Since it is hard to find a suitable dedicated software package and it is not desirable to develop self-built simulation software, a *general purpose* simulation environment is chosen. Within the TE group, LabVIEW is already available and does not bring extra costs with it. Furthermore, a lot of experience is already present and using a common software environment allows for easy integration of multiple models that have been or will be developed. Finally, LabVIEW satisfies all criteria listed in Section 3.1.1. Especially the ability to interface with hardware components for co-simulation is advantageous. Running co-simulations allows for testing of experimental demonstrators that do not comprise an entire system, but can be used as hardware parts in the simulation. Such a setup can thus be used to check demonstrator parts, but also to run simulations with real input signals. This makes LabVIEW an excellent choice for the purposes defined in this thesis.

3.2 Signal representation

Since LabVIEW has been chosen as a simulation environment, we have to define a signal representation that can be used for simulations in the field of RF photonics.

First, a description for both electrical and optical bandpass signals in the continuous domain will be introduced. Subsequently, a discrete-time equivalent will be derived. A discrete-time form is needed since the calculations of the simulator are to be carried out on a digital computer. This means that the signals processed in the simulator are sampled versions of the simulated continuous time signals.

After the description of continuous- and discrete-time signals, we will look into the sample rate that is suitable for modeling the system discussed in Chapter 2. We will see that there is a trade-off in the selection of the sample rate concerning the amount of samples and the need to change the sampling rate within the model, in order to minimize the number of total samples that must be processed.

3.2.1 Continuous-time bandpass representation

The bandpass signals present in the system can be described by a general form. For a signal that is modulated in amplitude $r(t)$ and phase $\psi(t)$ we can write

$$s(t) = r(t)\cos\Big(2\pi f_c t + \psi(t)\Big), \tag{3.1}$$

where f_c is the carrier frequency. The amplitude is chosen such that the average power of the signal is given by

$$\langle p(t)\rangle \triangleq \langle s^2(t)\rangle, \tag{3.2}$$

where $\langle\cdot\rangle$ denotes the ensemble average.

Electrical signal representation

When discussing electrical signals, we define the signal as a voltage difference between the inner and outer conductor of a transmission line. According to Ohm's law the average electrical power dissipated in a resistor with resistance R equals

$$\langle p(t)\rangle = \frac{\langle v^2(t)\rangle}{R}. \tag{3.3}$$

Now, considering a transmission line with characteristic impedance Z attached to a matched load resistor, the relation between the electrical voltage $v(t)$ and the normalized field $s(t)$ can be found using Eq. 3.2 and 3.3

$$v(t) = \sqrt{Z}\, s(t). \tag{3.4}$$

Optical signal representation

Optical signals can also be represented using the scalar wave representation. This signal simply represents the optical power and phase, and not the actual mode profile [23].

The description of the scalar wave representation was already shortly introduced during the discussion of the laser in Section 2.4, to describe the laser output. For convenience, the scalar wave representation is repeated here and is written in the amplitude and phase form, with optical frequency f_o:

$$E_o(t) \triangleq \sqrt{2P_o(t)}\, \exp\Big(\mathrm{j}2\pi f_o t + \mathrm{j}\phi_o(t)\Big), \tag{3.5}$$

such that the instantaneous power $P_o(t)$ is equal to

$$P_o(t) \triangleq \frac{1}{2}\left|E_o(t)\right|^2. \tag{3.6}$$

Note that the scalar wave representation can only describe an optical wave in one signal mode. For describing optical signals in a multimode waveguide, the required number of scalar wave representation equals the number of excited modes and the total instantaneous power follows from the sum of the powers in the scalar wave representations, as the mode profiles are orthogonal. However, in this thesis it will be assumed that all optical signals are completely polarized and travel in one single mode.

Modeling noise

In all systems noise is added to the desired signal by internal or external sources. Internal sources can be noisy resistors and external sources can be external interfering signals that couple into the system by means of electromagnetic interference (EMI) or unwanted signals received by the antenna.

Within communications, noise sources are often characterized by an effective noise temperature. The definition of the effective noise temperature originates from the thermal noise in a resistor, which is caused by the thermal motion of electrons. The available thermal noise power in a resistor is given by:

$$P_\mathrm{n} = kTB \tag{3.7}$$

with k the Bolzmann constant ($1.38 \cdot 10^{-23}$ J/K), T the absolute temperature in Kelvin, and B the bandwidth in Hz. Note that the available thermal noise power is independent of the resistance value, but proportional to the resistor temperature. Because of this simple relation between noise power and temperature, an effective noise temperature can be defined for other noise sources too, even if they are not thermal in origin. A noise source having a noise temperature T generates an available noise power equal to the thermal noise that would be generated by a resistor at temperature T.

Thermal noise is often characterized as having a constant spectral density for all frequencies and can be described by a wide-sense stationary process [33]. Such a noise process is then called white noise. The noise spectral density for positive and negative frequencies is often written as

$$S_{nn}(f) = \frac{N_0}{2}. \tag{3.8}$$

From a physical point of view white noise cannot be meaningful, since a constant spectral density for all frequencies would imply an infinitely amount of power. However, a large number of noise sources have a flat spectrum over a very broad frequency range. Normally, the frequency band B of interest is finite and lies within this range. This makes the white noise model useful in practice.

3.2.2 Discrete-time representation

The discrete-time equivalents of continuous signals are found by means of sampling. The resulting signal is then described by a sequence of samples $\{\tilde{s}[n]\}$, where each sample is defined as

$$\tilde{s}[n] = s(nT_\mathrm{s}), \tag{3.9}$$

where the tilde denotes the discrete-time equivalent of the continuous-time signal and T_s equals the sample time.

According to Nyquist's criterion, a signal that has an absolute bandwidth of B Hz is completely described by specifying its values at time instants separated by T_{s} seconds, provided that $T_{\mathrm{s}} \leq 1/(2B)$ [38].

Example 3.1

For an optical signal the absolute bandwidth is inherently high, even if the signals itself are narrowband. This is a result from the optical carrier having a high frequency. For an optical wavelength of 1550 nm, the carrier frequency is

$$f_{\mathrm{o}} = \frac{c}{\lambda_{\mathrm{o}}} = \frac{3.00 \cdot 10^{8}}{1550 \cdot 10^{-9}} \approx 194 \text{ THz}. \tag{3.10}$$

Using Nyquist's criterion, the sampling rate should be at least

$$f_{\mathrm{s}} \triangleq \frac{1}{T_{\mathrm{s}}} \geq 2 f_{\mathrm{o}} \approx 3.9 \cdot 10^{14} \text{ samples/s}. \tag{3.11}$$

According to the DVB standard, each channel has a bandwidth of 33 MHz and the corresponding transmission symbol rate can be found using the ratio $\mathrm{BW}/R_{\mathrm{symb}} = 1.28$ [35]. This means that for a datastream having a symbol rate of 25.8 Mbaud, the simulation would require

$$\frac{f_{\mathrm{s}}}{R_{\mathrm{symb}}} \approx \frac{3.9 \cdot 10^{14}}{25.8 \cdot 10^{6}} \approx 15 \text{ Msamples/symbol}. \tag{3.12}$$

As a result of Nyquist's criterion, signals that have a large bandwidth or high frequency component will need to be samples with a very high sampling rate, as we have seen in the previous example. Such a high sample rate puts severe constraints on the simulation tool, in terms of computational time, as a result of the many samples that must be processed. Therefore, it is interesting to investigate other forms of signal representation to reduce the sample rate and thus the bandwidth of the signal.

Equivalent baseband representation

Using a equivalent baseband description, the absolute bandwidth can be reduced to the signal bandwidth [33, Ch. 5]. Especially for narrowband bandpass systems, a lot can be gained by using such an approach.

The equivalent baseband description is obtained by taking the *complex envelope* of the signal, that contains all information except for the carrier frequency. The complex envelope is found by calculating the in-phase component $u(t)$ and quadrature component $v(t)$ of the signal $s(t)$

$$u(t) = r(t) \cos \psi(t), \tag{3.13}$$

$$v(t) = r(t) \sin \psi(t). \tag{3.14}$$

The complex envelope $z(t)$ is then defined as

$$z(t) \triangleq u(t) + \mathrm{j}v(t), \tag{3.15}$$

or in its polar form

$$z(t) \triangleq r(t) \exp\Big(\mathrm{j}\psi(t)\Big). \tag{3.16}$$

The real signal $s(t)$ can be found again by reinserting the carrier frequency f_c and taking the real part of the signal

$$s(t) = \mathrm{Re}\Big\{z(t) \exp(\mathrm{j}2\pi f_c t)\Big\}. \tag{3.17}$$

Note that the carrier frequency can have any value, but that the absolute bandwidth of $z(t)$ is minimized by choosing the carrier frequency in the middle of the bandpass spectrum.

In a discrete-time representation, the equivalent baseband signal can be represented as a sequence of complex numbers

$$\{\tilde{z}[n]\} \triangleq \{\tilde{u}[n] + \mathrm{j}\tilde{v}[n]\}, \tag{3.18}$$

where the tilde denotes the discrete-time description.

Example 3.2

Consider the optical signal from Example 3.1 again, being modulated with an IF signal of 2150 MHz. Since the optical carrier is DSB-SC modulated, the total bandwidth will be 4300 MHz.

Using the equivalent baseband representation we can reduce the highest frequency component in the signal to the IF bandwidth. When the carrier frequency is equal to the optical frequency of the carrier, the bandwidth is minimized and equals 2150 MHz. With Nyquist's criterion, the required sample rate can be shown to be

$$f_\mathrm{s} \triangleq \frac{1}{T_\mathrm{s}} \geq 2B = 4.3 \cdot 10^9 \text{ samples/s}. \tag{3.19}$$

This means that for a DVB stream of 25.8 Mbaud, the simulation would require

$$\frac{f_\mathrm{s}}{R_\mathrm{symb}} = \frac{4.3 \cdot 10^9}{25.8 \cdot 10^6} \approx 167 \text{ samples/symbol}, \tag{3.20}$$

which is roughly 90000 times smaller than in Example 3.1.

Whether or not such an equivalent baseband representation should be used in the model, depends on the bandwidth of the electrical and optical signals that are encountered and must be represented, and the specified sampling rate. Also note that the sample rate does not necessarily have to be constant, but may vary throughout the system by interpolation and decimation [39].

3.2.3 Sampling rate

Obviously, it is desirable to have a sampling rate as low as possible to minimize the number of samples. We have seen that using an equivalent baseband representation for a narrowband bandpass signal, the sampling rate is lower-bounded by twice the signal bandwidth. However, the question remains what sampling rates must be chosen throughout the system, as the signal frequencies will change throughout the system.

Since the beamformer system described in Chapter 2 is quite complex, it is even more desirable to minimize the total number of samples that have to be processed since a lot of calculations must be performed by the simulator. Therefore, it is attractive to use the baseband representation where it provides enough gain, as the conversion to the baseband representation can also be extensive [33]. In choosing the appropriate sampling rate, we must consider the lowest possible rate defined by Nyquist's criterion, but also each component must be represented correctly with the chosen sample rate. These criteria result in a trade-off between:

- the choice of a constant or varying sample rate throughout the system;
- a desired minimal sample rate to minimize the total number of samples, based on Nyquist's criterion;
- a lower bound on the sample rate, required to model components correctly;
- the consideration that changing the sample rate requires laborious interpolation and decimation operations.

A component where the sampling rate is critical is the ORR. Within the beamformer system, ORRs are encountered in the OBFN and the OSBF. We have seen in Figure 2.9(a) that the impulse response of a ring is discrete and the time between the samples depends on the RTT of the ring. To correctly simulate the behavior, it is straightforward to take the sample rate as an integer multiple of the FSR, which is the inverse of the RTT. In this case, the simulation model is analogous to the analytical model.

The specifications for the ORRs are given in [40]. For the rings in the OBFN, the FSR is upper bounded by fabricational limits and the accommodation of the signal gives rise to a lower bound, and must be in the order of 12–14 GHz. For the rings in the OSBF, the specifications are based on a desired stopband suppression of 25 dB. An FSR of 6.7 GHz has been chosen for the design of the filter to satisfy this criterion. A sampling frequency that satisfies all requirements for the ORRs is 13.4 GHz. This is in range for the FSR of the rings in the OBFN and is twice the FSR of the OSBF.

Now that a sample frequency for ORRs has been determined, it seems appropriate to use this sample frequency for the entire optical part of the system, which is mainly comprised by the ORRs. When looking at the electrical part, the IF signals can be represented as well with this sample frequency, except for the received RF signals before being downconverted in the LNB. Since up and downsampling operations are laborious and will also burden the system, it is more convenient to choose a single sample frequency for the entire system.

Using a sample frequency of 13.4 GHz in the simulator implies that only signals with frequency components below 6.7 GHz can be represented. Signals that have frequency components higher than this can be represented using the equivalent baseband representation, as long as the width of the passband signal is smaller than 13.4 GHz. For carrier frequencies f_c that are not located in the middle of the passband, the allowable passband width is even smaller.

Example 3.3

With a sample frequency of 13.4 GHz, the required number of samples for a DVB stream of 25.8 Mbaud is

$$\frac{f_\mathrm{s}}{R_\mathrm{symb}} = \frac{13.4 \cdot 10^9}{25.8 \cdot 10^6} \approx 519 \text{ samples/symbol}, \tag{3.21}$$

which is roughly 3 times the minimum number of samples that is needed (shown in Example 3.2), but still 30000 times smaller than the required number of samples from Example 3.1. Even though the required number of samples is higher than the absolute minimum, it does circumvent the need for up and downsampling.

Consequences for the simulation model

As a result of the chosen sample frequency, automatically some assumptions are made. It is important to understand what these assumption are and consider whether these result in inaccuracies in the system model and restrict the usability of the simulator, or not. The consequences for the ORRs in the OBFN and OSBF in the model are:

1. all ORRs in the OBFN are assumed to have exactly the same circumference, and thus an equal FSR;
2. the path length difference in the arms of the OSBF is assumed to be exactly half the circumference of the ORR in the OSBF;
3. the FSR of the rings in the OBFN is assumed to be exactly twice the FSR of the ring in the OSBF.

These constraints mainly issue problems concerning inevitable fabricational inaccuracies, limiting the simulator by not being able to reproduce the effects from this. First the effects of the fabricational inaccuracies on the actual system will be given, after which the consequences for the simulator are discussed.

1. In practice it will never be the case that all rings have exactly the same length. However, the fabricational accuracy in the pathlength of the ORRs is only ±1 micron, while the total pathlength is in the order of 1–2 cm. Such a small deviation can easily be corrected by a phase shift, using the thermo-optic heaters of the ring.

2. For the OSBF, the inaccuracy in fabricating the ring and optical delay path will result in a changing frequency response over multiple FSRs. This is related to Figure 2.14, where the FSR of the upper and lower arm will not exactly be an integer multiple of each other, resulting in a mismatch in the FSR. The result in the magnitude response is shown in Figure 3.1. It is clear that the stopband suppression degrades over multiple FSRs. When the deviation in pathlength is only small, a sufficient stopband suppression over the desired frequency range can be obtained.

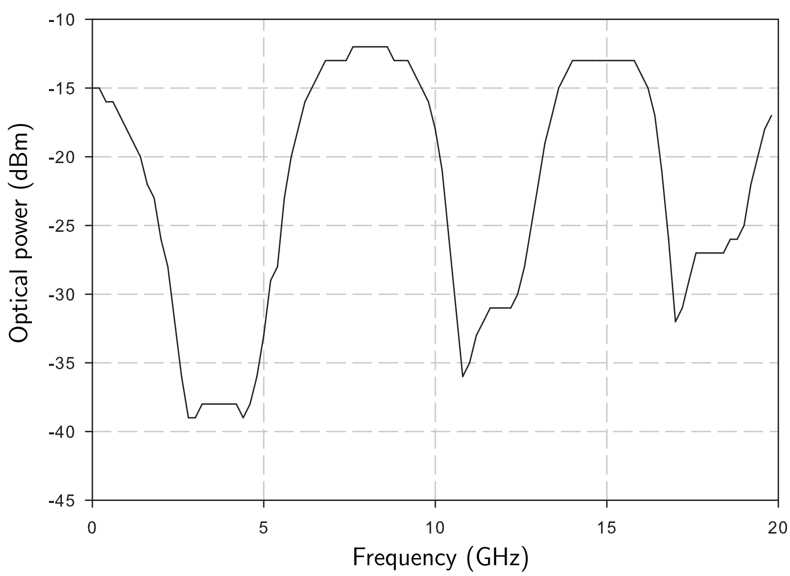

Figure 3.1: Measured magnitude response of an optical sideband filter (OSBF) over multiple FSRs, where the FSR of the MZI is not exactly twice the FSR of the ORR

3. A range has been given in the design for the FSR of the rings in the OBFN, but no ultimate specification. Therefore, in the actual system it is conceivable that the FSRs will not exactly overlap, and must be aligned in the final design to operate on the desired frequencies. This is of no effect, however, as long as the bandwidth requirements are satisfied to accommodate the signal and obtain a wide enough flat passband in the filter and a more or less constant group delay in the OBFN.

Above, the effects on the actual system are illustrated. The following consequences can be stated to have an effect on the simulation model.

1. Since all circumferences are bounded by the sample frequency, it is not possible to simulate the effect of small variations in the ring circumferences and use the simulator to investigate this. However, these variations are that small, meaning that the simulated behavior will not deviate much from the actual behavior;
2. The FSRs of the OBFN and OSBF will be perfectly aligned, opposed to the actual system. This is of no further consequence, as the processed signals will still fit well within the obtained FSR.
3. The varying magnitude response resulting from the mismatch in the OSBF cannot be simulated. For a single wavelength this brings no limitations as the response can be considered constant for a narrowband signal, but might limit the usability for multi-wavelength systems [41]. This is, however, related to the actual implementation.

Also note that not being able to simulate the effect of the inaccuracies might result in a better performance in the simulator than will observed with the actual system.

The consequences mentioned will not considerably degrade the usability of the simulator for the optical beamformer system in the SMART project. However, the necessity to simulate these effects in other RF photonics systems might result in a limited usability. Whether this is the case depends on the simulation purposes of the model, possibilities for co-simulations in combination with hardware, the usage of other simulation software and the actual need to model the effects which are not incorporated.

To study the effects resulting from the fabricational inaccuracies, a small simulator can be developed that investigates these effects, which is working with a higher sample frequency. This is not further considered in this thesis.

3.3 Conclusions

In this chapter we have selected LabVIEW as a simulation environment for the development of the simulator tool. This general purpose simulation environment allows us to define our own signal representation and is available within the TE group. Furthermore, a signal representation for both the electrical and optical domain has been introduced, together with their discrete-time equivalents. Finally, the sample frequency that will be used in the simulator is discussed and chosen to be 13.4 GHz, based on the RTT of the ORRs in the chip that was designed for the SMART demonstrator.

Chapter 4

Modeling the optical system components

In Chapter 2 a functional description of the SMART system has been given, together with a signal description for each block. In Chapter 3 a simulation environment has been chosen that will be used to model the system in.

This chapter will discuss the modeling of the optical beamforming system, whereas Chapter 5 will go into detail on the the satellite signal generation and reception, as well as the decoding of the signal after beamforming.

The optical beamforming system is depicted in Figure 4.1, and includes both the conversions to the optical domain and back to the electrical domain. The individual components will be discussed from the inside out, starting with the ORRs, working our way to a complete optical beamformer.

In each section the modeling components are identified and described, which are part of the block that must be implemented. Subsequently the implementation in LabVIEW is discussed. At the end of this chapter a discussion on noise sources in the optical beamformer system is given.

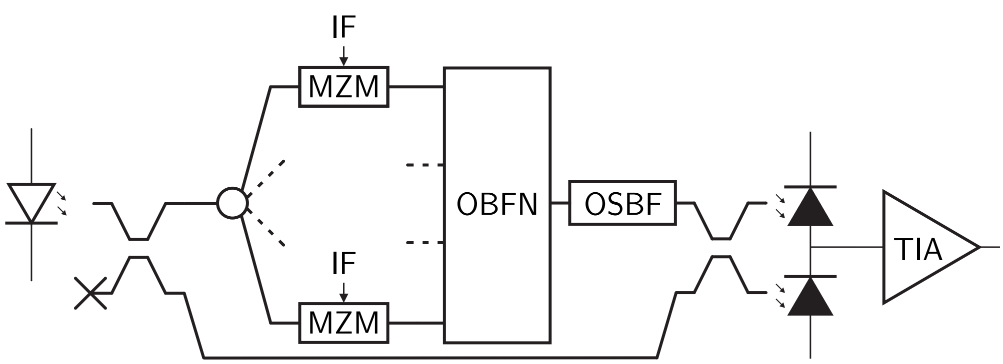

Figure 4.1: Optical beamformer system, including the conversion from and to the electrical domain.

For completeness, it is stated again that an equivalent baseband representation is used in the modeling of the optical beamformer, for the reasons mentioned in Section 3.2. Furthermore, all models are developed in the time domain, which enables bit to bit simulation.

4.1 Optical ring resonators

The ORRs are the core components in the optical beamformer system, as they provide a broadband true time delay.

4.1.1 Modeling components

In Section 2.5 we have seen that ORRs consist of a straight waveguide and a recirculating waveguide coupled parallel to it, of which a schematic drawing is given in Figure 4.2(a). When modeling an ORR, four components can be distinguished:

- *a ring*, introducing a delay equal to the RTT;
- *an optical phase shifter*, with tuning parameter ϕ;
- *a directional coupler (DC)*, with tuning parameter κ;
- *the waveguide loss*, related to the circumference of the ring.

Ring In Section 3.2.3 it was discussed that it is desirable that the RTT of the ring equals an integer multiple of the sample time. Therefore, with a sample frequency of 13.4 GHz the RTTs of the ORRs are realized by means of a single or double sample

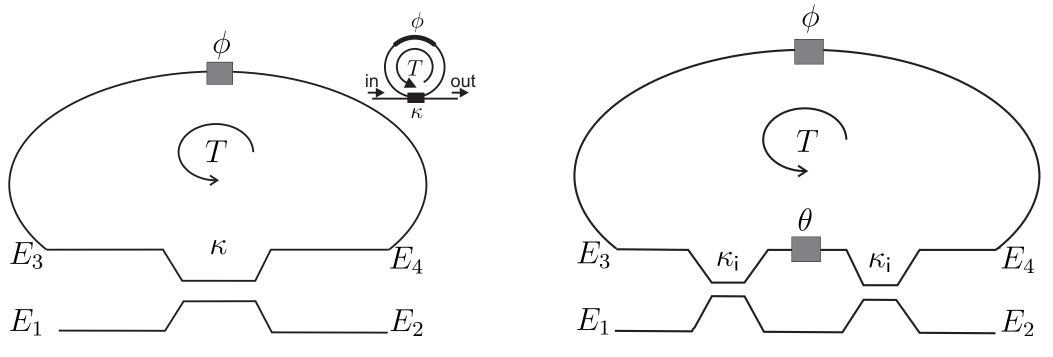

(a) ORR with one DC, with coupling coefficient κ. The inset shows the equivalent symbol used for an ORR.

(b) ORR with two DCs, having fixed coupling constant κ_i and an optical phase shifter θ to tune the coupling coefficient κ.

Figure 4.2: Schematic views of an optical ring resonator (ORR), showing the directional coupler (DC) as a part of the ring [15]

shift, corresponding with an FSR of 13.4 or 6.7 GHz respectively. The rings with an FSR of 13.4 GHz, and thus a smaller circumference, are used in the OBFN, whereas the rings with an FSR of 6.7 GHz are used in the OSBF.

Optical phase shifter In practice, the phase shift ϕ is a heater that uses the thermo-optic effect to change the refractive index and subsequently change the RTT of the ring. Since the variations in the RTT are that small that they can be approximated by optical phase shifts on top of a fixed RTT realized with a sample shift. Since a baseband representation is used, the complex signal $\tilde{z}[n]$ can be multiplied by a simple phase term

$$E_3 = E_4 \exp(-\mathrm{j}\phi), \tag{4.1}$$

where ϕ is the optical phase shift specified in radians.

DC The coupling section of the ORR can be characterized with a DC, which can be tuned by the power coupling coefficient κ. The transfer matrix is given by Eq. 2.10.

The transfer of the DC is based on the length of its multimodal section, where two waveguides are close together. To be able to tune the value of κ, we must thus be able to vary the length of this section. However, after fabrication the length is fixed, resulting in a fixed coupling value κ_i. In Figure 4.2(b) a solution using two DCs is given that makes κ tunable by means of an additional optical phase shifter θ [15]

$$\kappa = 4\kappa_\mathrm{i}(1-\kappa_\mathrm{i})\cos^2(\theta/2). \tag{4.2}$$

The phase shift θ is realized by changing the refractive index of the waveguide using the thermo-optic effect. Ideally the fixed coupling coefficient κ_i should have a value of 0.5, but the best value for fabricated κ_is is 0.465. This limits the practical tuning maximum. Note that the cosine term has a maximum value of 1, and the term $4\kappa_\mathrm{i}(1-\kappa_\mathrm{i})$ limits κ to 0.9951 [15]. The minimum value for κ is always zero.

Waveguide loss A waveguide has low loss, but in the case of an ORR it is increased slightly as a result of the small bending radius of the ring. The loss is usually specified in dB/cm and thus depends on the length of the ring. The circumference d of the ring is related to the RTT T by

$$d = \frac{Tc}{n}, \tag{4.3}$$

where c is the speed of light in vacuum and n the group index which is assumed to be approximately 1.55. For a complex signal the loss can be introduced by a factor that scales the magnitude

$$|E_3| = \gamma\,|E_4|\,, \tag{4.4}$$

with $\gamma = 10^{-\alpha/20}$ and α is the total loss of the ring in dB. Note that γ will incorporate the losses introduced by the DC, that is part of the ORR, as well.

The losses introduced in the ORRs are considered to be the dominant source in the OBFN and OSBF, and losses introduced by straight waveguides and individual DCs are neglected.

4.1.2 Simulation model and results

In Figure 4.3 the LabVIEW model of an ORR is shown. The input is a complex sequence or array of samples, that is being processed element-wise in the for-loop. The complex signal is split in its magnitude and phase, using Eq. 3.16, to scale the magnitude and change the phase. With the usage of a shift register, a sample shift is introduced to simulate a single RTT and is indicated with the symbols ▲▼.

The group delay response of an ORR can be determined by the simulation of the impulse response. The frequency response is obtained by taking the Fourier transform (FFT) of the impulse response, from which the phase response can be obtained. The group delay response is then found by taking the negative derivative of the phase.

The simulated group delay response is shown in Figure 4.4(a). Note that the peak is shifted to different center frequencies for different values of θ. This is a result from the phase shifter θ, not only changing the parameter κ (Eq. 4.2) but also introducing an extra phase shift. In [15] it is explained how this unwanted phase shift can be compensated, using ϕ. Apart from this compensation, ϕ is also used to shift the peak to a desired center frequency. After the compensation, the group delay responses are perfectly aligned as shown in Figure 4.4(b). It was verified that the resulting group delay responses in Figure 4.4(b) are identical to the analytical calculations, using Eq. 2.11.

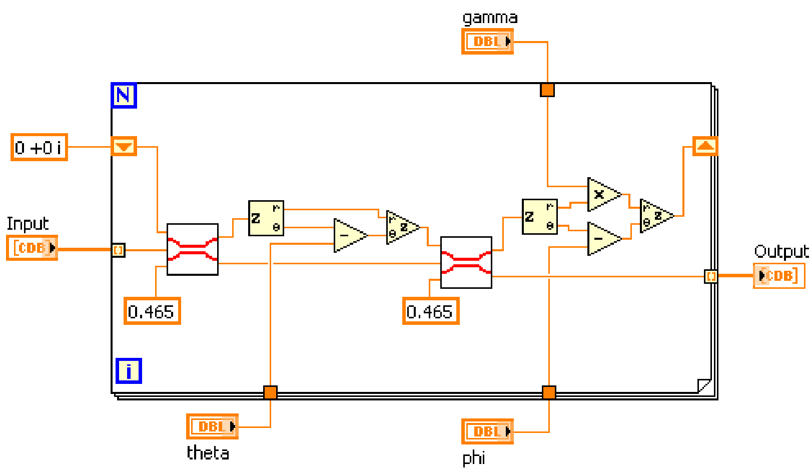

Figure 4.3: LabVIEW implementation of an optical ring resonator (ORR), using a for-loop

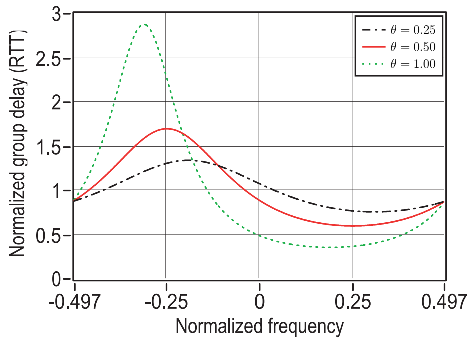

(a) Group delay without phase compensation

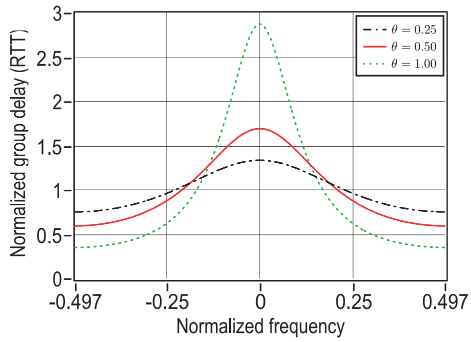

(b) Group delay with phase compensation

Figure 4.4: Simulation results, showing the group delay of an optical ring resonator (ORR)

4.2 Optical beamforming network

The OBFN consists of multiple ORRs, used to synchronize all inputs and combine them to a single output.

4.2.1 Modeling components

Within the OBFN three levels of abstraction can be identified, as shown in Figure 4.5:

- *a delay element*, consisting of one or more rings in cascade;
- *a branch couple*, consisting of two branches and a combiner;
- *a stage*, consisting of one or more branch couples.

Delay element The total group delay response of a delay element is the superposition of all individual responses of the ORRs. The desired height of the group delay response depends on the delay difference between subsequent inputs given by Eq. 2.3, whereas the width of the curve must be equal to the bandwidth of one sideband of the modulated optical signal. The number of ORRs needed to realize the required delay over the

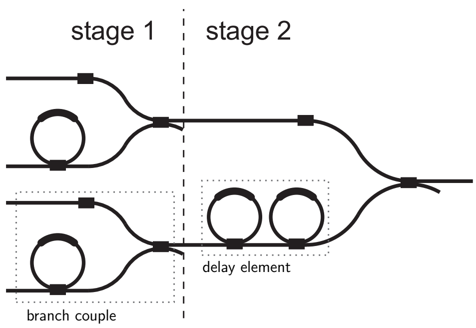

Figure 4.5: 4 × 1 optical beamforming network (OBFN)

appropriate bandwidth in a delay element is discussed in [15]. A phase shift ϕ can be added to all rings in the delay element, to shift the delay curve to the desired center frequency, such that a single sideband is enclosed by the group delay curve. The required ring settings are calculated by an algorithm developed in [16] and implemented in [18]. Given an OBFN structure, the necessary parameters are calculated, with a maximum of five ORRs per delay element, and used to synchronize all inputs of the OBFN.

Branch couple Every branch couple synchronizes two inputs, resulting in a single output after combining them. The lower branch consists of a delay element and the upper branch consists of an optical phase shifter to align the branches, such that the optical signals are added constructively in the combiner. The combiner is a tunable DC, of which a single output is used and operates as a 1:1 power splitter (i.e. $\kappa = 0.5$). In the ideal case one of the outputs will be zero as a result of destructive interference, while the other output is maximized. The coupling factors of the combiners are fixed, but must be tunable when investigating amplitude tapering. However, this is not considered in this thesis. In [19] an optical phase synchronization method has been developed in LabVIEW, but is not yet implemented in the simulation model discussed in this thesis.

Stage In each stage, one output per branch couple is generated, which serves as the inputs for the branch couples in the next stage.

4.2.2 Simulation model and results

Network structure

The components discussed in the previous section are used to build up a complete OBFN structure. In order to be able to simulate any size of OBFN, it is desirable to use a dynamical implementation that loops through as many stages, branch couples and delay elements as required, such that a single output remains. A simplified version of a dynamical OBFN implementation is shown in Figure 4.6.

The number of stages m can be found using $m = \log_2(n)$, where n is the number of inputs or AEs. The outputs of the previous stage are used as the inputs of the next stage, using shift registers. Within each stage, the model loops through the branch couples. For each branch couple the lower branch is processed by a delay element and the upper branch is aligned in optical phase with the lower branch, after which both branches are combined and added to the output. When there are multiple ORRs in a delay element this loop is executed multiple times, using shift registers as well.

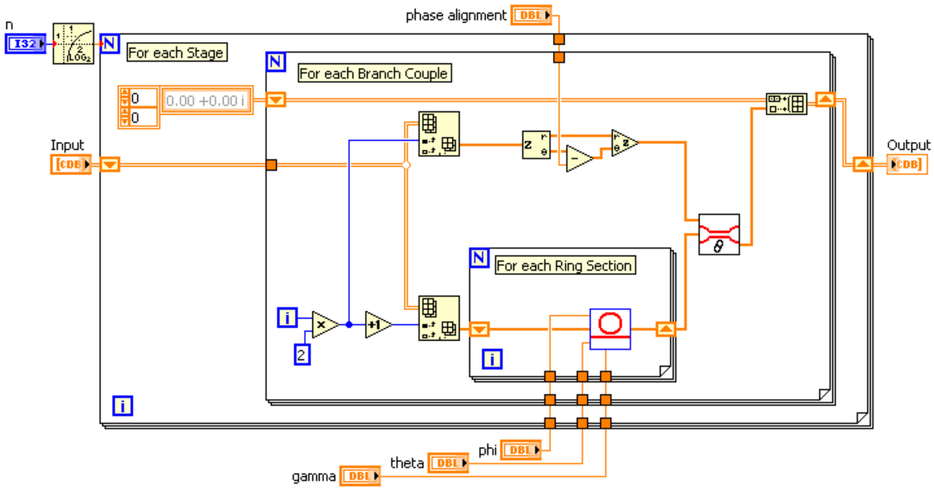

Figure 4.6: Simplified LabVIEW schematic of a dynamical optical beamforming network (OBFN), using an implementation with for-loops

Especially in the case of a dynamical implementation it is important that, during each iteration, the correct parameters are fed to the ORR, such that the correct group delay responses are generated. The required parameters are generated by an algorithm implemented in [18], requiring the OBFN structure and angle of incidence as inputs. The definition of this structure is discussed in Appendix A. The size of the OBFN structure is in principle unlimited, but is now limited by a maximum of five ORRs per delay element for which the required parameters can be calculated.

Planar arrays

So far, we have only considered OBFNs for linear arrays, limiting the focusing of the beam in only one dimension. With planar arrays we can focus in two dimensions, resulting in the ability to focus to any point in the sky. In the simulation the processing for focusing in two dimensions is implemented using multiple OBFNs as shown in Figure 4.7. In this setting the inputs are synchronized and combined for one dimension and subsequently synchronized and combined for the other dimension.

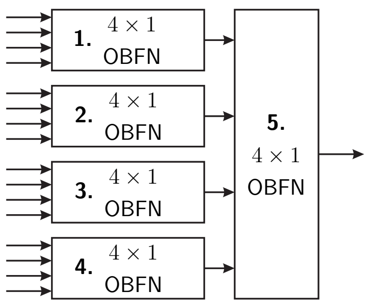

Figure 4.7: 16×1 optical beamforming network (OBFN) for a 4×4 PAA

Pre-delays

In the binary tree structures for the OBFN, shown in Figures 2.11 and 4.5, the upper paths have fixed delays since there are no ORRs in it. This structure has been chosen to reduce the total number of rings, but, at first sight, does not enable the reception of negative incident angles, as this would require a negative progressive delay between the branches. This problem can be solved by inserting pre-delays before the OBFNs.

For a linear array, the delay difference between two consecutive inputs, corresponding to the maximum incident angle of 60° specified in [40], is approximately 40 ps. The total tuning range is then roughly $2 \times 40 = 80$ ps, since we want to receive from both positive and negative angles. In order to do this, the tuning range $[0, 80]$ should be shifted to $[-40, 40]$, which can be done by fixed length differences in the coax cables from the PAA to the optical beamformer. The extra delay that has to be inserted for the most upper branch equals half the total tuning range between the first and last branch, which is $(7 \times 80)/2 = 280$ ps for eight AEs. The delays for the other inputs are found by progressively decreasing the to be inserted delay by half the tuning range between two consecutive AEs ($80/2 = 40$ ps). The implementation of this is discussed in more detail in Section 5.1.

Furthermore, the minimum delay of a single ring at the resonance frequency equals 1 RTT. Depending on the number of rings in each path, this creates an offset which must be compensated for. Since 1 RTT equals exactly the sample time, the offsets are easily corrected by inserting sample shifts, such that all paths have an equal minimum delay. In the simulator these delays are introduced in the OBFN, whereas in the actual system these delays are compensated in the coax delays.

4.3 Optical sideband filter

4.3.1 Modeling components

As explained in Section 2.6 the OSBF is used to remove a sideband of the DSB-SC-modulated optical signal, to reduce the total signal bandwidth. The OSBF is an asymmetric MZI with an ORR in its shortest arm, consisting of the following components:

- *two DCs*, as part of the MZI;
- *a delay line*, making the MZI asymmetric;
- *an ORR*, introducing a non-linear frequency dependent phase response.

DC Ideally, the DCs are both in 1:1 power splitting mode, having a coupling factor κ of 0.5. Since we cannot fabricate DCs with this exact value, the couplers are made tunable to be able to adjust them accordingly. In Section 4.1 a procedure has been discussed, utilizing two DCs to form a single coupler.

ORR In Section 3.2.3 we have seen that the FSR of the filter equals 6.7 GHz. This is exactly half the sample rate, and can thus be implemented with two sample shifts. The schematic implementation is equal to the one in Figure 4.3, except that a double instead of a single shift register is used.

Delay line Since the MZI is asymmetric, its arms have a difference in length. This is realized by introducing a relative delay in one of the arms. The delay is exactly half the RTT of the ORR and is implemented using a single sample shift.

4.3.2 Simulation model and results

The simulation model of the OSBF is shown in Figure 4.8. The individual phase responses of the upper and lower arm in the OSBF are given in Figure 4.9(a). Within one FSR the phase of the delay line (lower arm) changes over 2π, corresponding with one sample delay. For the ORR the phase changes over 4π, since a delay of two samples is incurred.

Since the FSR of the ORR is exactly half the FSR of the OSBF, the non-linear frequency dependent phase response of the ORR is shown twice in the spectrum. When comparing Figures 4.9(a) and 4.9(b), we see that a maximally flat passband is obtained when there is a constant phase difference [32, Ch. 6]. With ϕ and the phase of the arm, the center frequency of the magnitude response can be shifted, such that the passband covers a single sideband. In [21] a tuning method for the filter has been developed, and the influence of the non-linear phase response is discussed.

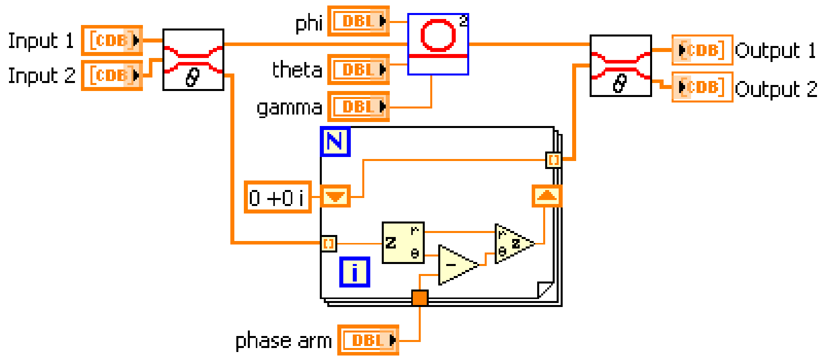

Figure 4.8: Simplified schematic of an optical sideband filter (OSBF). The DCs shown with a θ consist of two DCs having a fixed coupling coefficient κ_i and a phase shifter θ in between, and the 2 in the ORR denotes a double sample shift.

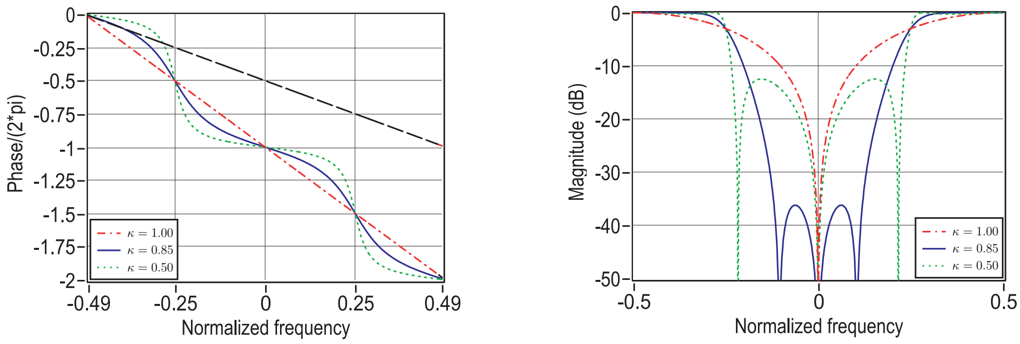

(a) Phase responses of the the lower arm (dashed line) and the upper arm (other lines)

(b) Magnitude response of the OSBF

Figure 4.9: Transfer function of an optical sideband filter (OSBF). Both ϕ and the phase of the arm are set to π. The values of κ are obtained by tuning θ properly, and the unwanted phase shifts resulting from that are compensated for.

4.4 Laser

4.4.1 Modeling components

The optical carrier is generated by a laser, which is split into multiple branches such that each of them can be modulated individually. Therefore, we have the following components:

- *laser*, to generate the optical carrier;
- *splitting network*, splitting the laser signal to multiple unmodulated carriers that are to be modulated by the AE signals.

Laser The laser generates a signal that is used as optical carrier in the optical beamformer. Each laser has RIN and phase noise, but this will not be considered in this thesis since in the performance analysis in [22] it was shown that this can be neglected. If it proves necessary in the future that RIN and phase noise are taken into account, the laser can be replaced with a more advanced model. More information about these noise sources can for example be found in [42].

Splitting network In the splitting network, the laser signal is split into two signals by means of a DC. One signal will be used as optical carrier to be modulated with the RF signals from the AEs, while the other unmodulated carrier is used for coherent detection. The amount of power that is used for modulation and coherent detection can be regulated, using the coupling coefficient of the DC, as shown in Figure 4.10. The splitting is performed by DCs.

4.4.2 Simulation model and results

Since RIN and phase noise are neglected, the complex envelope of the laser signal is specified by a constant amplitude of $\sqrt{2P_o}$ (Eq. 3.6). Moreover, the complex envelope can completely be described by the optical power.

Which part of the power is used to be modulated by the AE signals and which part is used for coherent detection, can be regulated by the coupling factor κ. Using a dynamical implementation, any number of AE signals can be accommodated. The DCs that are used to obtain the optical carriers that are modulated, are operating in a 1:1 splitting mode since no amplitude tapering is considered. It is possible to change the implementation later on, to simulate amplitude tapering as well. The number of splitting stages m can be found using $m = \log_2(n)$, where n is the number of AEs. Comparing Figure 4.10 with Figure 2.11, we see that the splitting into multiple unmodulated carriers is more or less the reverse operation of the OBFN. Note that the multiple splitting of the laser signal is a laborious operation, and will be omitted in the case of a laser signal with a constant optical power. In this case, a single signal is generated with correct power and directly used for all MZMs.

4.5 Mach-Zehnder modulator

4.5.1 Modeling components

For each AE signal, the MZM modulates this signal onto an optical carrier. The operation that the MZM performs is:

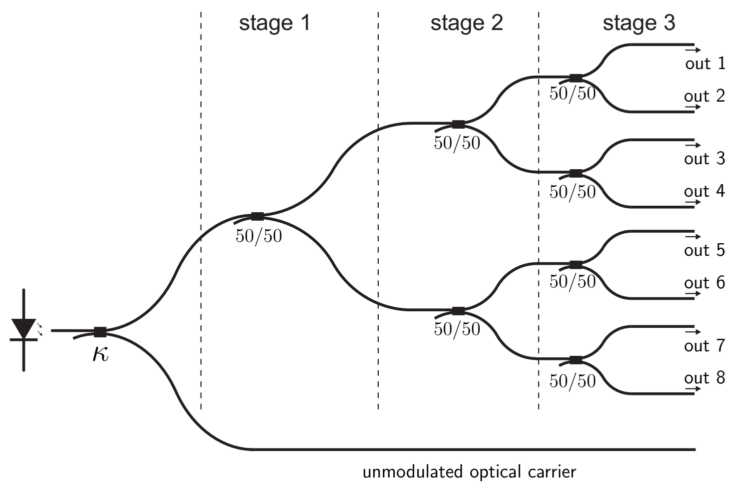

Figure 4.10: Optical carrier generated by a laser, is split into an unmodulated carrier for coherent detection, and multiple carriers that are used to modulate the AE signals on. This schematic is based on eight AE signals. Since no amplitude tapering is assumed, the DCs are in 1:1 splitting mode.

- *DSB modulation*, converting phase to amplitude modulation.

DSB modulation The modulation operation is performed by the MZM, converting the electrical QPSK-modulated signal to an optical amplitude-modulated signal. The transfer function is given by Eq. 2.8 and 2.9. These formulas are used to evaluate the output, instead of simulating the actual behavior. This limits the extent to which the push-pull operation can be investigated and the influence of phase distortion, resulting from fabricational inaccuracies. The noise that is introduced by a possible matching resistor is discussed in Section 4.7.

4.5.2 Simulation model and results

In Figure 4.11 the LabVIEW building block of the MZM is shown. For each IF signal originating from the LNBs, DSB-SC modulation is performed. Inside the MZM building block, Eq. 2.8 is executed to generate the output signal.

As the MZM is a non-linear device, harmonics are introduced during the modulation operation. In Section 2.4 it is explained that, by biasing the MZM correctly ($\Delta V/V_{\pi,\mathrm{DC}}$ is odd), even harmonics can be suppressed, which includes the optical carrier. The suppression of the direct-current term in the complex envelope of the modulated signal is shown in Figure 4.12(a). The amount of non-linear distortion (harmonics) depends on the modulation depth. For a large modulation depth the linear approximation is not valid anymore, since the transfer levels off, as shown in Figure 2.6(b). To make the non-linear distortion more clear, the modulation depth is set to more than one, clearly showing the third order harmonics in Figure 4.12(b). Note that there is a trade-off between the non-linear distortion and the amount of power in the output signal, resulting from the modulation depth [20, 22].

The push-pull operation of the MZM prevents any chirping, since the phase shift in one arm is canceled by the other arm. Since the behavior of the MZM is evaluated by its transfer function and not actually simulated, the modulated signals will always

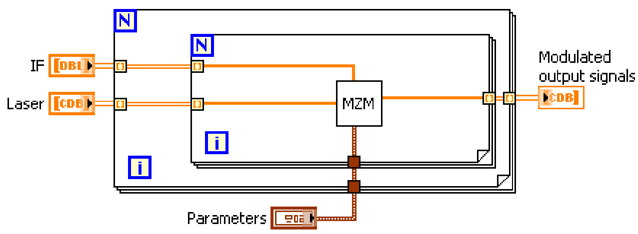

Figure 4.11: LabVIEW implementation of the MZM. Each IF signal is modulated onto an optical carrier. Note that both the laser signals and the outputs are complex, since an equivalent baseband representation is used for optical signals.

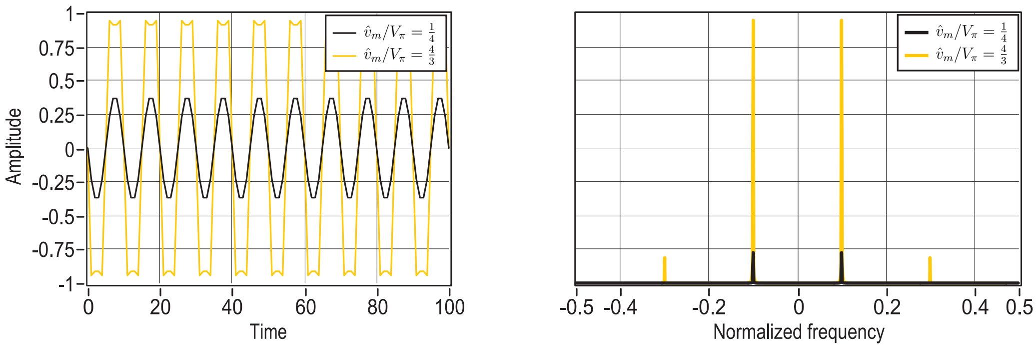

(a) Equivalent baseband representation of two modulated sine waves, with different modulation depths

(b) Power spectrum of modulated sine waves

Figure 4.12: Response of a Mach-Zehnder modulator (MZM) for a input sine wave, showing third order harmonics resulting from non-linear distortion

be chirp-free, corresponding with the ideal behavior of the MZM. If it proves desirable to simulate an imbalance between both arms, Eq. 2.8 can be modified by inserting an extra factor in front of the transfers in the branches $H_{\mathrm{PM},m}(t)$.

4.6 Balanced detection

4.6.1 Modeling components

For balanced detection the following operations and components are encountered:

- *carrier reinsertion*, required for coherent detection;
- *two photodiodes*, which are used in a balanced detection scheme;
- *transimpedance amplifier (TIA)*, converting the photocurrent to a voltage.

Carrier reinsertion Since the carrier is suppressed in the DSB-SC modulation scheme, coherent detection must be performed. The optical carrier is reinserted using a DC, as shown in Figure 4.1. The DC operates in 1:1 splitting mode, such that both outputs will be equal in power. The tunable DC is implemented using two fixed DCs or tunable MZI, as discussed before in Section 4.1.

Photodiode The photodiode converts the detected optical power to a photocurrent. The relation between optical power and current is given by the responsivity, as described by Eq. 2.12. There are several noise sources within a photodiode that generate noise currents. The most considerable sources are shot noise and thermal noise. Furthermore, noise will result from the RIN from the laser and there will be a dark current from spontaneous generation. These noise sources are discussed in more detail in Section 4.7.

TIA After balanced detection, a photocurrent is obtained which must be converted to a voltage. This is done using a TIA, where the transfer is determined by Eq. 2.14. The thermal noise introduced by the resistor can be modeled with a white Gaussian noise source and is explained in Section 4.7.

4.6.2 Simulation model and results

In Figure 4.13 a simplified balanced detection scheme is shown. First the optical carrier is reinserted. In the photodiodes the optical power is calculated with Eq. 2.13 and converted to a current, using the responsivity. The subtraction of the photocurrents will result in an IF current. With the transimpedance of the TIA a voltage will result as output.

4.7 Noise in the optical beamformer

In Chapter 2 the input-output relation for each component has been discussed. However, possible noise sources have been omitted and must be taken into account. This section will discuss the noise sources encountered in the optical beamforming system and will give the model used for implementation in LabVIEW.

Noise sources in the photodiodes are shot noise, dark current and thermal noise. Furthermore, there is thermal noise in the TIA and the MZMs.

The noise sources in the laser will not be discussed in this thesis, but more information on this can be found in [42]. In Section 4.4 it was explained that a more detailed model could be implemented if necessary.

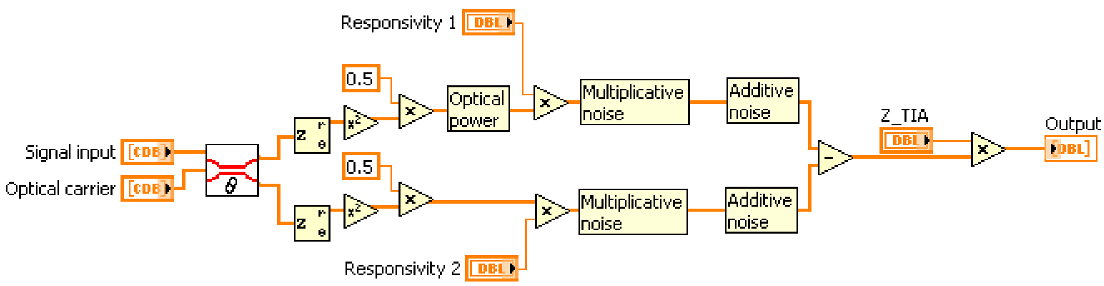

Figure 4.13: Simplified schematic of a balanced detection scheme. The locations where multiplicative and additive noise sources can be added is depicted.

4.7.1 Dark current

From [34] we know that the dark current has a maximum of 1 nA. With a responsivity of 0.8 A/W the equivalent optical input power is 1.25 nW. Assuming that the laser has an output power in the order 20 mW and assuming equal splitting, both the optical carrier for coherent detection and the optical carrier that is to be modulated as shown in Figure 4.10, will have an equal power of 10 mW. The amount of power resulting from the unmodulated carrier that reaches each of the photodiodes after reinsertion, will be 5 mW. This amount of power is already very large compared to the equivalent power resulting from the dark current (5 mW $\gg$ 1.56 nW). From this we conclude that the dark current can be neglected.

4.7.2 Shot noise

When carriers are generated by photons in a photodiode, shot noise is produced. The time between arrivals of different photons is generally not constant, and therefore the generation of carriers that contribute to the output current occurs at random points in time. For a constant optical power, the number of events in a fixed interval of time can be described by a Poisson distribution [43].

Since the optical power is not constant but varies with time as a result of amplitude modulation, we are dealing with an inhomogeneous Poisson process. As the amount of shot noise depends on the incident optical power, the noise process is characterized as a multiplicative process. This means that the outcome of the Poisson process must be realized at each sampling instant using the average power within one sampling instant as input, being a laborious operation for the simulator tool. From simulations we found that this implementation causes a severe bottleneck concerning speed.

A better approach is to use a simpler alternative to realize the Poisson process. In [23] it is suggested that this can be done using a Gaussian approximation. The approximation holds when the rate of the Poisson process is very large. In this case the rate represents the mean number of generated electron-hole pairs in a single time interval, which can be considered large ($4 \cdot 10^{16}$ for an optical power of 5 mW). The total output current of the photodiode consists of a photocurrent resulting from the responsivity $I_{\mathrm{p}}(t)$, a shot noise current $I_{\mathrm{sn}}(t)$, and a thermal noise current $I_{\mathrm{th}}(t)$ as we will see later on. This can be denoted as

$$I_{\mathrm{pd}}(t) = I_{\mathrm{p}}(t) + I_{\mathrm{sn}}(t) + I_{\mathrm{th}}(t). \tag{4.5}$$

The shot noise term is generated by a Gaussian noise source, with a current spectral density that can be found using Schottky's formula

$$S_{I_{\mathrm{sn}}I_{\mathrm{sn}}}(f) = e\,\langle I_{\mathrm{p}} \rangle = \frac{1}{2}\, e\, R\, \langle |E_{\mathrm{p}}|^2 \rangle, \tag{4.6}$$

where R is the responsivity, e the electron charge and E_p the optical field detected by the photodiode. The shot noise model in LabVIEW is shown in Figure 4.14. In the balanced detection scheme shown in Figure 4.13, shot noise is added at the position of multiplicative noise. In a for-loop the Gaussian process is executed for each sample separately. Note that the Gaussian processes in both photodiodes are independent noise sources.

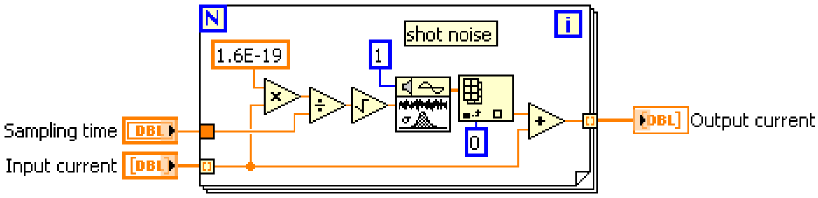

Figure 4.14: LabVIEW implementation of shot noise for a single photodiode, showing a Gaussian noise source producing the number of generated electron-hole pairs

In the discrete-time domain a noise current $\tilde{I}_\mathrm{sn}[n]$ can be realized by creating a zero mean Gaussian noise sequence with discrete power spectral density

$$S_{\tilde{I}_\mathrm{sn}\tilde{I}_\mathrm{sn}}(\nu) = \frac{S_{I_\mathrm{sn}I_\mathrm{sn}}(f)}{T_\mathrm{s}}, \tag{4.7}$$

where ν is the normalized frequency and equals fT_s. An extensive discussion on this can be found in Appendix B.

Example 4.1

In this example a calculation will be performed on the amount of shot noise that is experienced. If we consider the power of the received satellite signal to be -150 dBW, and the gain of the LNB 60 dB, the power of the IF signal at the optical beamformer will be -90 dBW. The coherent gain of the OBFN is equals to the number of inputs, and equals approximately 32 dB for 1,600 AEs [22]. The optical power arriving at the photodiode will therefore be in the order of -58 dBW.

Before detection by the photodiode, the modulated optical signal is combined with the unmodulated carrier, that will have a power of approximately 5 mW, as explained in Section 4.7.1. With a responsivity of 0.8 A/W, the detected current is shown as the solid line in Figure 4.15, showing a sine wave that represents the IF signal. When shot noise is added to the signal, the dotted line results. Since the shot noise mainly depends on the power of the modulated carrier, and not on the small modulating signal, the noise can be larger the modulating signal itself. From Eq. 4.6 the power spectral density of the current noise source can be determined to be $5.12 \cdot 10^{-22}$ A^2/Hz. Multiplying the power spectral density with the bandwidth, which is equal to the sample frequency of 13.4 GHz, a noise power of $6.86 \cdot 10^{-12}$ A^2

results. The amplitude of the noise current is then found to be 2.62 μA, which corresponds with the results that are shown.

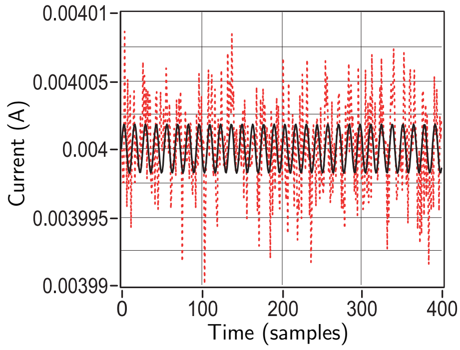

Figure 4.15: Illustration of shot noise in the photodiode with a responsivity of 0.8 A/W. The optical signal consists of an unmodulated carrier of 5 mW and a modulating signal of -58 dBW. The solid line show the photo current after detection, without shot noise. The dotted line includes shot noise.

4.7.3 Thermal noise in the photodiode

Besides shot noise and dark current, there is thermal noise in a photodiode. In Figure 4.16 an equivalent circuit for a silicon photodiode is shown, which can be used to determine the origin of thermal noise in the photodiode. The photodiode is represented by a current source parallel to an ideal diode, which represents the p-n junction. In addition, a junction capacitance C and a shunt resistance R_{sh} are shown. The series resistance R_{s} arises from the resistance of the contacts and the resistance of the undepleted silicon. More details on the equivalent circuit model and its components can be found in [44].

The thermal noise is an additive noise source and is added to the photodiode output current as shown in Eq. 4.5. In Figure 4.17(b) an equivalent scheme is given of an ideal resistor with a current noise source.

The most important source causing thermal noise is the shunt resistor. Actual values for this resistor range from 10 to 10000 MΩ [44]. In Section 3.2.1 we have seen that thermal noise sources can be represented with a white noise process, which can

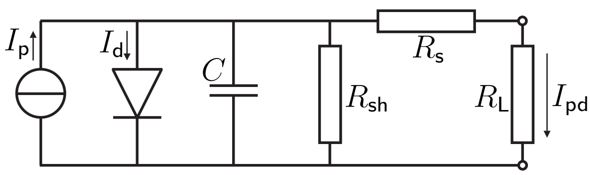

Figure 4.16: Equivalent circuit for a silicon photodiode

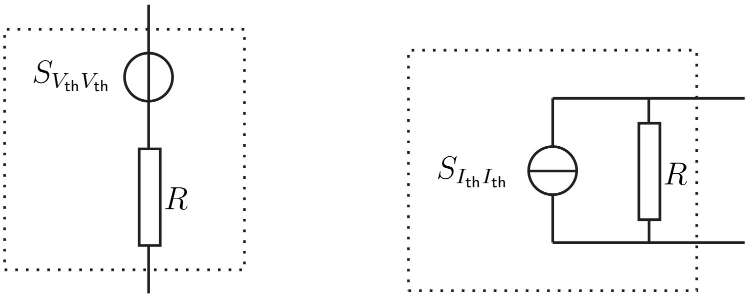

(a) Thevenin equivalent for a noisy resistor

(b) Norton equivalent for a noisy resistor

Figure 4.17: Models of a noisy resistor, showing a voltage and current noise source.

be realized with a Gaussian noise source. The mean value of the Gaussian process is zero, and since the noise is wide-sense stationary, the variance is independent of time and equals the power spectral density in the discrete time domain. In Figure 4.17(b) we see an equivalent scheme for a noise resistor that is modeled with a noise current source and an ideal resistor. The power spectral density of the current source is given to be [33]

$$S_{I_{\mathrm{th}}I_{\mathrm{th}}}(f) = \frac{2\,k\,T}{R}, \tag{4.8}$$

where k is the constant of Bolzmann, T the absolute temperature of the resistor and R the resistor value. With Eq. 4.7 the discrete power spectral density can be obtained, and is equal to

$$S_{\tilde{I}_{\mathrm{th}}\tilde{I}_{\mathrm{th}}}(\nu) = \frac{2\,k\,T}{R_{\mathrm{sh}}\,T_{\mathrm{s}}}, \tag{4.9}$$

where R_{sh} is the shunt resistance. The additive Gaussian noise is added after the shot noise and before the subtraction of the photocurrent in Figure 4.13. Again, the noise sources are independent for both photodiodes.

The junction capacitance C in Figure 4.16 is used to determine the speed of the response of the photodiode. This capacitance is considered very small, such that no noticeable distortion occurs to the detected signal. This approximation seems valid, since the frequency of the detected IF signal (1–2 GHz) is well below the cut-off frequency (8–9 GHz) of the photodiode specified in [34].

4.7.4 Thermal noise in the TIA

The transimpedance of the TIA is also a large contributor to thermal noise. Opposed to the thermal noise in the photodiode, the resistor Z_{TIA} can be modeled with a voltage source. When looking at Figure 2.16 we see that there is no impedance matching, since the input impedance of the opamp can be considered infinity. This large input impedance also causes the input of the first opamp to be virtually grounded, resulting

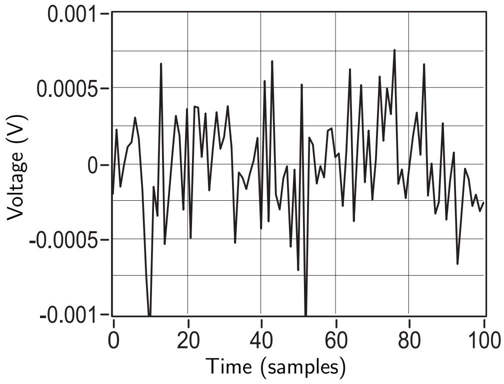

(a) Thermal noise voltage, resulting from the transimpedance of 1200 Ω at a temperature of 290 K.

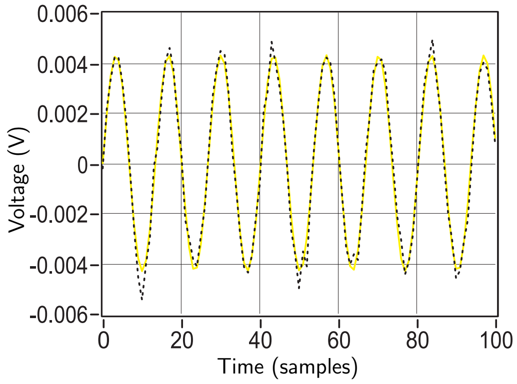

(b) Output signal of the TIA, with (dotted) and without (solid) thermal noise

Figure 4.18: Thermal noise, introduced by the TIA

in a negative voltage over the transimpedance Z_{TIA}. The noisy resistor can thus be modeled with an ideal resistor with a voltage noise source, as shown in Figure 4.17(a).

From [33] we know that the power spectral density of the voltage source is given by

$$S_{V_{\mathrm{th}}V_{\mathrm{th}}}(f) = 2\,k\,T\,Z_{\mathrm{TIA}}, \tag{4.10}$$

such that the discrete power spectral density using Eq. 4.7 is

$$S_{\tilde{V}_{\mathrm{th}}\tilde{V}_{\mathrm{th}}}(\nu) = \frac{2\,k\,T\,Z_{\mathrm{TIA}}}{T_{\mathrm{s}}}. \tag{4.11}$$

The noise voltage can be realized using a Gaussian noise source with zero mean and a variance equal to the power spectral density.

Example 4.2

In this example with the values from Example 4.1, but omitting any shot noise. After detection by the photodiodes, the resulting photocurrents are subtracted from each other as shown in Figure 4.13. The current is then converted to a voltage, where the ratio is given by the transimpedance. This transimpedance also introduces thermal noise.

For a transimpedance of 1200 Ω at a temperature of 290 K, the voltage spectral density can be determined to be $9.6 \cdot 10^{-18}$ V^2/Hz, using Eq. 4.10. Again, the bandwidth is equal to the sampling frequency, such that the noise power is $1.29 \cdot 10^{-7}$ V^2. By taking the square root, the amplitude of voltage noise source is found to be on average 0.36 mV, which matches with Figure 4.18(a). In Figure 4.18(b) the solid line shows the IF signal without thermal noise, whereas the dotted line does contain thermal noise.

4.7.5 Thermal noise in the MZM

In the MZM noise is introduced, resulting from the input impedance. A schematic view of the situation is given in Figure 4.19.

The noisy input impedance behaves as an extra voltage source with a spectral density as given in Eq. 4.11. However, the generated noise is divided over the output and input impedance, such that the input noise is reduced. The power spectral density of the noise voltage over the input is given by

$$S_{\tilde{V}_{\mathrm{th}}\tilde{V}_{\mathrm{th}}}(\nu) = \frac{2\,k\,T\,R_{\mathrm{in}}}{T_{\mathrm{s}}}\frac{R_{\mathrm{in}}^2}{(R_{\mathrm{out}}+R_{\mathrm{in}})^2}. \tag{4.12}$$

Assuming that the impedances are matched ($R_{\mathrm{in}} = R_{\mathrm{out}}$), the power spectral density is reduced to

$$S_{\tilde{V}_{\mathrm{th}}\tilde{V}_{\mathrm{th}}}(\nu) = \frac{k\,T\,R_{\mathrm{in}}}{2\,T_{\mathrm{s}}}. \tag{4.13}$$

4.8 Summary

This chapter has described the modeling of the optical beamformer, as depicted in Figure 4.1. The individual models can be attached to each other to form a complete beamformer system.

In the modeling process we started out with the ORRs, which are the key components of the beamformer. We have seen that a tunable coupling factor can be realized by two DCs with a fixed κ and phase shift in between. Using multiple ORRs and DCs a model of an OBFN is realized of which the required parameters can be calculated by [18]. The OSBF consists of an ORR that has twice the circumference of the ORRs in the OBFN and is realized with a double sample shift. The laser signal is modeled

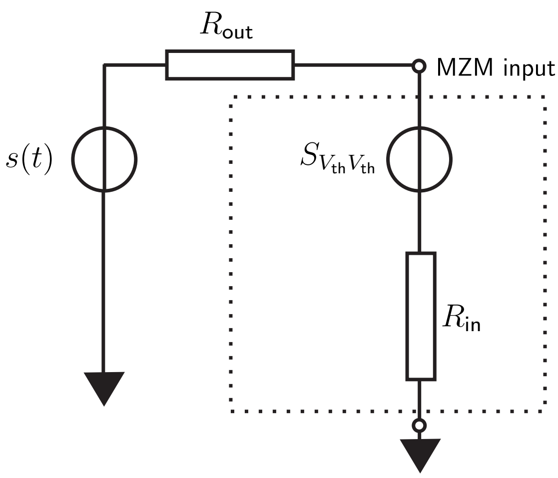

Figure 4.19: Model of a noisy input resistor, that acts an ideal input resistor with a voltage noise source

as a sequence with constant amplitude and phase. Depending on the number of AEs, the laser signal is split multiple times. Each laser signal is used as an input for the MZMs to modulate an IF signal on, using an implementation by formula. Using the responsivity of the photodiodes the received optical signals are converted to a current, and finally to a voltage by the TIA.

Finally, several noise sources have been discussed that are encountered in the optical beamformer. Noise sources are important to obtain a more realistic simulation and to be able to say something about the performance of the actual system. These noise sources include thermal noise in the MZM, photodiodes and TIA, and shot noise in the photodiode. The dark current in the photodiode turned out to be negligible.

Chapter 5

Defining a context for the optical beamformer

In the previous chapter we have discussed the components of the optical beamformer system. In this chapter we will focus on the context of the optical beamformer, such that the signals which are processed by the beamformer are well-defined. In line with the SMART project, the signals to be processed are DVB-satellite (DVB-S) signals which are received by a PAA.

We will not only discuss the desired signal, but also other signals that might be picked up by the AEs. The nature of these signals can originate from interfering satellites or other sources, and will be discussed in more detail.

Furthermore, the decoding of the signal that results as the output from the optical beamformer will be explained in more detail. At the end of this chapter a total system simulation is described, showing the signals and operations performed on the signals throughout the system.

5.1 Signal reception

First, the definition of the DVB-S signal is discussed in more detail, after which the reception of the signal by the AEs and the downconversion by the LNBs are considered.

5.1.1 Definition of the satellite signal

The signal that is received from the satellite is a DVB-S signal. The DVB-S signal is generated at a ground station, sent to a satellite, amplified, and sent back towards Earth. The satellite fleet that gives coverage for continental Europe and North-Africa is Astra 19.2°E [26]. The satellite signals are transmitted in the K_u band and range from 10.7 to 12.75 GHz, as was shown in Figure 2.2. The signal has both horizontal and vertical polarization and consists of 60 transponders per polarization, resulting in an availability of over 1150 television and radio channels. The complete DVB-S signal is provided by the satellites in the fleet together.

The DVB-S signal is standardized by the European Telecommunications Standards Institute (ETSI) and specified in [35]. A DVB-S signal consists of a multiplexed MPEG-2 stream that is modulated using QPSK. In Figure 5.1 the constellation diagram of conventional Gray-coded QPSK with absolute mapping is shown, using two bits per symbol. Each transponder in the K_u band represents a separate QPSK signal that has a bandwidth of 26–36 MHz. In between the transponders there is a guard band of at least 4 MHz. In this thesis we will assume a fixed bandwidth of 33 MHz and bandwidth-symbol rate ratio $\mathrm{BW}/R_{\mathrm{symb}}$ of 1.28, resulting in symbol rate of approximately 25.8 Mbaud [35, Annex C].

Before QPSK modulation, channel coding and baseband pulse shaping are applied. Channel coding enables the receiver to correct errors which have occurred in the transmission path, by adding redundancy to the information in the transmitter. For DVB-S an outer RS code is used, together with an interleaver and a convolutional inner code. Within this thesis, channel coding will not be considered in more detail and is not implemented in the simulator.

Pulse shaping has two interrelated purposes:

1. maximizing spectral efficiency, by generating bandlimited channels;
2. reducing inter-symbol interference (ISI).

Pulse shaping can be performed by a raised cosine filter. A normal pulse has high frequency components that can cause interference. By smoothing the pulse with a filter, a bandlimited pulse can be obtained. The response of such a filter is shown in Figure 5.2. Note that there is a zero-crossing at each sampling instant other than 0, which reduces the effect of ISI. The roll-off factor α is used to make a trade-off between the pulse bandwidth and the amount of ISI (in the case of timing jitter), depending on how fast the pulse levels off.

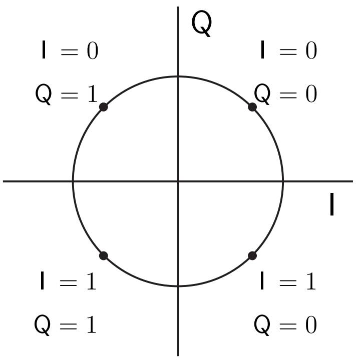

Figure 5.1: Constellation diagram for QPSK

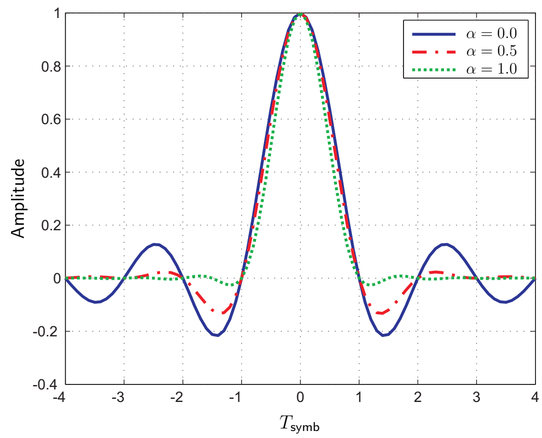

(a) Frequency response for raised cosine filter

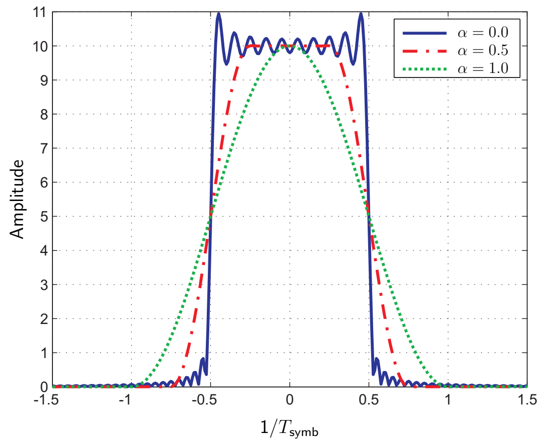

(b) Impulse response for raised cosine filter

Figure 5.2: Raised cosine

Often, a raised cosine filter is implemented using two *root* raised cosine filters. One of the filters is used at the transmitter end for pulse shaping, while the other is used at the receiver end as a matched filter. The cascade of both filters will result in the desired response equal to that of a single raised cosine filter. It is advantageous to use a filter at the receiving end that matches the received signal, as this maximizes the SNR at the detector output [33]. For the DVB-S signal a root raised cosine with a roll-off factor of 0.35 is specified [35].

5.1.2 DVB-S reception by the antenna elements

The DVB-S signal is considered to be received by a flat PAA, such that the delay between adjacent elements is constant. This enables easy modeling and a more easy determination of the settings for the ORRs in the OBFN. Each of the AEs will receive an identical signal $s(t)$, but with a different delay. It was shown that the difference in delay can be calculated with Eq. 2.3, based on the angle of incidence and the distance between two AEs.

In the simulator tool we have to simulate these delays as well, such that the signals can be synchronized in the optical beamformer later on. In Chapter 3 a suitable sample rate of 13.4 GHz has been discussed, which corresponds with a sample time of 74.63 ps. Ideally, we want to use sample shifts to delay the broadband signal to incur no distortion. However, in Section 4.2.2 we have seen that the total tuning range comprises 80 ps, meaning that with a sample time of 74.63 ps only two angles of incidence can be simulated, corresponding to zero and one sample shift. By increasing the sample rate, more incident angles can be simulated, but this also requires a larger number of total samples. For example, if we consider twelve different angles, the sample rate must be increased by a factor twelve as well, resulting in a sample rate which is already 160.8 GHz. In that case the number of samples per symbol will be in the order of 6,250.

A more flexible approach is to use phase shifts to delay each carrier in the AE signal, enabling us to simulate any possible angle. This comes, however, at the cost of some distortion that is added to the signal. Note that phase shifters are not used in the actual physical implementation, but merely as a tool in the simulator. Instead of Eq. 2.2, the AE signal can then be written with a phase shift in each carrier, omitting any delay for the envelope (amplitude and phase):

$$v_{\mathrm{AE},m}(t) \cong \sqrt{Z_{\mathrm{c}} G_{\mathrm{AE}}} \sum_{n=1}^{N} r_n(t) \cos\Big(2\pi f_{\mathrm{RF},n}(t-\tau_m) + \psi_n(t)\Big). \tag{5.1}$$

Note that actual gain of the AEs differs from the theoretical gain, which is specified by the aperture efficiency η. For the simulation models it will considered that the actual gain of the AEs is specified, such that the aperture efficiency can be left out of consideration.

Example 5.1

A time delay can be approximated with a phase shift, when the shift is only small compared to the symbol time. If we assume that time delays are performed by sample delays when possible, the maximum delay that must be realized by phase equals one sample time (74.63 ps).

A symbol rate of 25.8 Mbaud for DVB-S corresponds with a symbol time of 38.76 ns. The ratio of the symbol time and maximum delay by phase shift is

$$\frac{38.76 \cdot 10^{-9}}{74.63 \cdot 10^{-12}} \approx 519, \tag{5.2}$$

showing that the symbol time is much larger than the sample time, making the error in the envelope negligible. Note that it is necessary to realize the delays partly by sample shifts, and cannot be realized by phase shifts solely.

For a PAA of 32 AEs, with an element spacing of 1.5 cm, and an angle of incidence equal to 60°, the delay between the first and last element approximately 1.34 ns (Eq. 2.3). The ratio of the symbol time and maximum delay by phase shifts would be

$$\frac{38.76 \cdot 10^{-9}}{1.34 \cdot 10^{-9}} \approx 29, \tag{5.3}$$

showing that the delay of the envelope cannot be neglected.

In Example 5.1 we have seen that using a combination of both sample and phase shifts results in the required delay with a negligible pulse distortion. Therefore, the AE signals will not only consist of a phase shift of the carrier as shown in Eq. 5.1, but the signal will have a relatively small error for the envelope as well.

5.1.3 Downconversion by the LNBs

In Figure 2.4 we have seen that the LNB consists of two bandpass filters (BPFs), an amplifier, and a mixer for downconversion to IF. As a result of the polarization decoupling, filtering and downcoversion, one of the four bands of the DVB-S signal can be selected. Thus, either the horizontal or vertical polarization is selected, in combination with the upper or lower part of the band, as explained in Section 2.3. A signal with a bandwidth of 1200 MHz will result (950–2150 MHz).

Note that a single mixing carrier is used to preserve coherency. A phase shift is introduced by the downconverting operation from RF to IF, with the mixing carrier generated by the LO. This can be seen in the voltage signal described by Eq. 2.4. This offset ($2\pi f_{\mathrm{LO}\tau_m}$) can be compensated in the optical beamformer, or in the downconverting operation. When the mixing signals that are used for downconversion are delayed in phase, such that they match the time delay of the signal that is to be downconverted, the phase term will disappear and the output voltage of the LNB can be written as

$$\begin{aligned} v_{\mathrm{LNB},m}(t) = &\sqrt{Z_{\mathrm{c}} G_{\mathrm{AE}} G_{\mathrm{LNB},m}} \\ &\cdot \sum_n r_n(t-\tau_m) \cos\Big(2\pi f_{\mathrm{IF},n}(t-\tau_m) + \psi_n(t-\tau_m)\Big), \end{aligned} \tag{5.4}$$

where $\{f_{\mathrm{IF},n}\}$ is the set of subcarriers at IF between 950–2150 MHz.

5.1.4 Noise generated by the AEs and the LNBs

Both the AEs and the LNBs generate noise that must be taken into account. The noise can be characterized with an equivalent noise temperature, as explained in Section 3.2.1.

The noise that is generated by the AEs is a result from the fact that the antenna itself is actually a conductor.

The noise in the LNBs is mainly generated by the BPFs. From [45] we know that an equivalent temperature of 50 K ($F = 0.7$ dB) can be assumed for an LNB.

All noise sources can be considered incoherent, which means that effectively the mean powers will add up in power in the beamformer. It is important that the equivalent noise temperature in these components is kept as low as possible, since according the Friis' formula, the system noise temperature is largely defined by the first components. Friss' formula for the noise temperature is

$$T_{\mathrm{system}} = T_1 + \frac{T_2}{G_1} + \frac{T_3}{G_1 G_2} + \cdots\,, \tag{5.5}$$

where T_n and G_n are respectively the noise temperature and gain of component n.

5.1.5 Implementation in LabVIEW

The signal reception is modeled in LabVIEW using a simplified scheme, to reduce the computational burden on the simulator. The major difference is that only those transponders are simulated, that will appear after being processed by the LNB. Furthermore, the operation of the LNB is omitted and the generated subcarriers are directly upconverted from baseband to IF instead of RF, as shown in Figure 5.3. This means that the LNB spectrum shown in Figure 2.5 is directly generated. The two advantages of this are:

1. there is no need to use an equivalent baseband representation, since the IF band can be represented directly with a sample rate of 13.4 GHz. This would not have been the case if RF signals needed to be represented;
2. the laborious operations in the LNB, including filtering and downconversion, are avoided. As a result of this, the transfer of BPFs is considered ideal and any noise that is introduced will be represented by an equivalent noise temperature.

A QPSK signal is realized by standard blocks in LabVIEW. For each subcarrier a separate bit stream is used, which are upconverted after modulation with their respective IF carrier frequencies. The parts of the delays that can be realized with sample shifts, will be introduced after the signal has been upconverted to IF. The remaining parts will be introduced giving an extra phase in the upconverting mixing carrier. Note that for each subcarrier a different phase offset is used to minimize the distortion, according to $\phi_{n,m} = 2\pi f_{\mathrm{IF},n}\tau_m$, where $f_{\mathrm{IF},n}$ is the IF frequency of each subcarrier n.

When introducing a phase shift in the mixing carrier that equals the time delay of the signal to preserve coherency, the phase term in Eq. 2.4 disappears and the output voltage of the LNB consists of a set of subcarriers at IF between 950 and 2150 MHz, as described by Eq. 5.4. However, as mentioned before, a combination of phase and sample shifts is used to delay the signal, instead of a real true time delay.

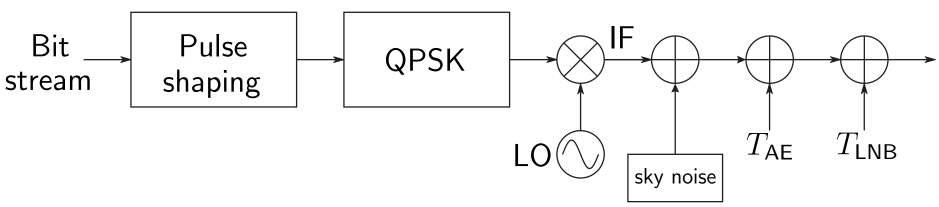

Figure 5.3: Schematic steps for the generation of the received satellite signal by a single AE. In the figure the signal consists of only one channel. Multiple channels can be summed, after being upconverted to the correct frequency in the IF band (950–2150 MHz). Sky noise represents noise that is received by the AEs from the sky

and the temperatures represent thermal noise sources.

With Friis' transmission equation the amount of power that is received can be calculated. After upconversion of the QPSK signal and before adding noise, the signal must be scaled according to this power level. The voltage and the power of the simulated signal can be calculated with Eq. 3.4 and 3.3, respectively.

5.2 Noise reception

The noise that is received by the AEs is called sky noise. There are four sources that can be identified to contribute:

- cosmic microwave background radiation;
- atmospheric noise;
- Earth noise;
- interfering satellites.

Cosmic microwave background radiation Cosmic microwave background radiation (CMBR) originates from the 'Big Bang'. The noise temperature is defined as the temperature that is observed when looking in zenith (directly at the sky), assuming that there is no atmosphere. cosmic microwave background radiation (CMBR) shows a frequency-dependent noise power, but can be considered constant around 2.7 K for frequencies above 1 GHz [46].

Atmospheric noise Atmospheric noise results from black body radiators in the atmosphere of the Earth, that extends about 20 km above the Earth's surface. The main contributors of atmospheric noise are water vapor and oxygen, which mainly reside in the troposphere. The contribution to the noise temperature is shown in Figure 5.4, depicting the observed brightness temperature [46].

Earth noise The Earth can be approximated as a black body radiator with an average temperate of 290 K. If an antenna had its entire radiation pattern directed towards ground, the antenna temperature T_A would be approximately 290 K. The amount of Earth noise picked up by the AEs on aircraft depends on the mounting position.

Interfering satellites The satellite spacing is in the order of 2 degrees in the US and in the order of 3 degrees in Europe [27]. Since the receiving AEs have an almost hemispherical radiation pattern, multiple satellite signals will be picked up. Only when the beamforming operation is performed, the radiation pattern of the entire array will show a small main lobe. Figure 5.5 shows the radiation patterns of linear arrays, where the beamwidth becomes smaller by an increasing number of AEs. Note that only those

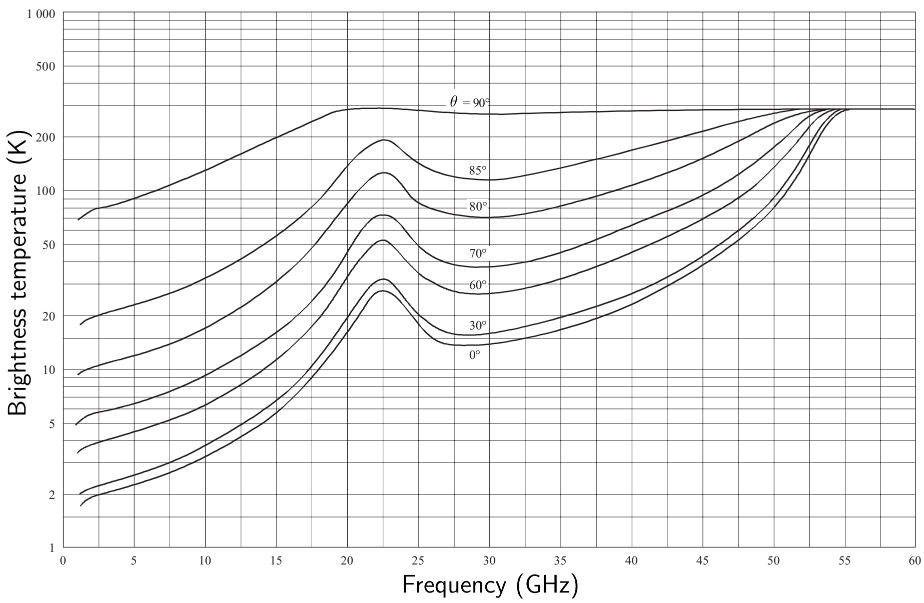

Figure 5.4: Brightness temperature for clear air for 7.5 g/m^3 of water vapor concentration

satellites that are transmitting within the same frequency range (10.7–12.75 GHz) will be seen as interfering sources. The number of satellites that would be in range, and therefore are considered as noise sources, is not investigated in this thesis.

5.2.1 Noise picked up by the AEs

Noise sources can be characterized by an equivalent noise temperature, as explained in Section 3.2.1. For sky noise sources this temperature is called the brightness temperature of the sky and indicates the temperature that is observed by the antenna,

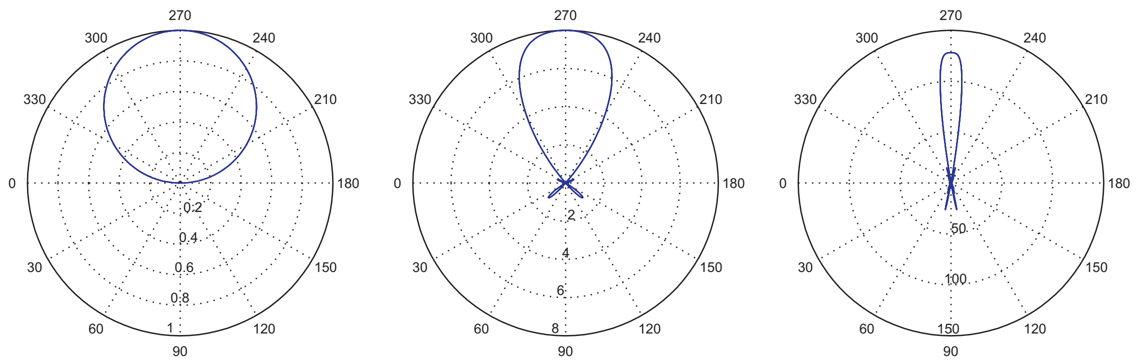

(a) Radiation pattern of a single AE (b) Radiation pattern of a linear array with 8 AEs (c) Radiation pattern of a linear array with 128 AEs

Figure 5.5: Radiation patterns of an individual AE and two linear array of AEs. Note that the peak gain equals the number of AEs.

and with Eq. 3.7 the actual received noise power can be determined. The amount of noise power that actually appears at the antenna terminals depends on the gain and radiation pattern of the antenna. This temperature is characterized by the antenna temperature T_{A} and is given by [47, 48]

$$T_{\mathrm{A}} = \frac{\displaystyle\int_0^{2\pi}\int_0^{\pi} T_{\mathrm{B}}(\theta,\phi)\, G(\theta,\phi)\, \sin(\theta)\, \mathrm{d}\theta\, \mathrm{d}\phi}{\displaystyle\int_0^{2\pi}\int_0^{\pi} G(\theta,\phi)\, \sin(\theta)\, \mathrm{d}\theta\, \mathrm{d}\phi}, \tag{5.6}$$

where $T_{\mathrm{B}}(\theta,\phi)$ is the brightness temperature that is observed in a direction, specified by the zenith distance θ and the azimuth angle ϕ. For a lossless passive antenna the denominator equals 4π steradian. By taking the integral over the sky an average temperature is obtained that is perceived by the antenna.

Eq. 5.6 showed that the antenna temperature can be found by integrating over the complete radiation pattern, multiplied by the brightness temperatures of the sky noise sources. It is important to note that the broadside direction of the PAA is not necessarily in zenith. By changing the orientation of the PAA the observed antenna temperature will probably increase, as the antenna will pick up more Earth noise that has a high brightness temperature. For example, NLR is investigating at what positions it is desirable to place PAAs on the plane fuselage to obtain a desirable radiation pattern for the whole array. This indicates that the observed noise temperature can be considerable and must be taken into account.

5.2.2 Coherent noise sources

In the design process of modeling sky noise, it is important to note that the sky actually exists of an infinite number of radiating bodies, and thus noise sources. The time-delayed versions of the noise signals that are received by the AEs are coherent. Therefore, the reception of sky noise is quite similar to the reception of the satellite signals.

Whether the coherent noise sources will add up constructively in the beamformer depends on the gain of the total radiation pattern of the PAA. In fact, this pattern shows from which direction the signals are added constructively and destructively.

Since it is not possible to generate an infinite number of radiating bodies, a better way is to divide the sky in a discrete number of areas that are represented by a single noise source. Of course the noise is modeled more correctly if the number of parts is high. However, a trade-off must be made here, since a larger number of noise sources also increases the computational burden on the simulator.

5.2.3 Sky noise model in LabVIEW

The observed sky noise at the output of the LNB will be in the IF band, after it has been downconverted and filtered. In Figure 5.3 we have seen that the generation of the satellite signal occurs directly in the IF band, which is the approach that will be used for the generation of sky noise as well.

Just as the satellite signals, the noise signals must be delayed as well, such that each AE receives a correctly delayed signal. For the satellite signals we decided to use phase shifts to delay each individual subcarrier in the signal, under the assumption that the relative delay is much smaller than the symbol time. In Example 5.1 we saw that this was indeed the case. However, in the case of noise signals there are no narrowband subcarriers. Thus, to correctly delay the broadband noise signals (950–2150 MHz), we must work with sample shifts.

In order to realize the correct delay with one or more sample shifts, the sample rate must be increased to obtain the appropriate sample times. After the delays have been introduced, the signals are downsampled to comply with the system sample rate of 13.4 GHz. The operation of downsampling can be performed by decimation. Decimation is the process by which high-frequency information is eliminated from a signal to reduce the sampling frequency without resulting in aliasing [39]. The process of decimation is shown in Figure 5.6, where M is the decimation factor (or downsampling factor). The low-pass filter (LPF) has a cut-off frequency at $f_s/(2M)$ Hz to avoid aliasing.

It is advantageous to use multiple stages in the decimation process, i.e. a cascaded architecture of the decimation process that was shown in Figure 5.6. Especially for large changes in sample rates, multiple stages are found to be more computationally efficient, since this leads to a considerable relaxation in the specifications of the anti-aliasing filters [39].

To avoid the necessity of interpolation during the decimation operation, it is decided to use only sample frequencies that are integer multiples of the system sample frequency. This requirement limits possible angles of incidence (related to the unit time delay by Eq. 2.3) without using excessive sample rates, but still allows for a fair amount of angles from which noise sources can be simulated.

The LabVIEW implementation is shown in Figure 5.7. Each sky noise source is associated with a noise power spectral density, a decimation factor, and a sample shift

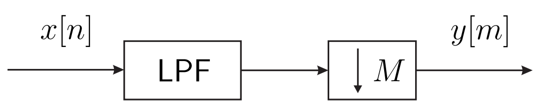

Figure 5.6: Decimation in a single stage. The low-pass filter (LPF) has a cut-off frequency of $f_s/(2M)$ and avoids aliasing, and M is the decimation factor.

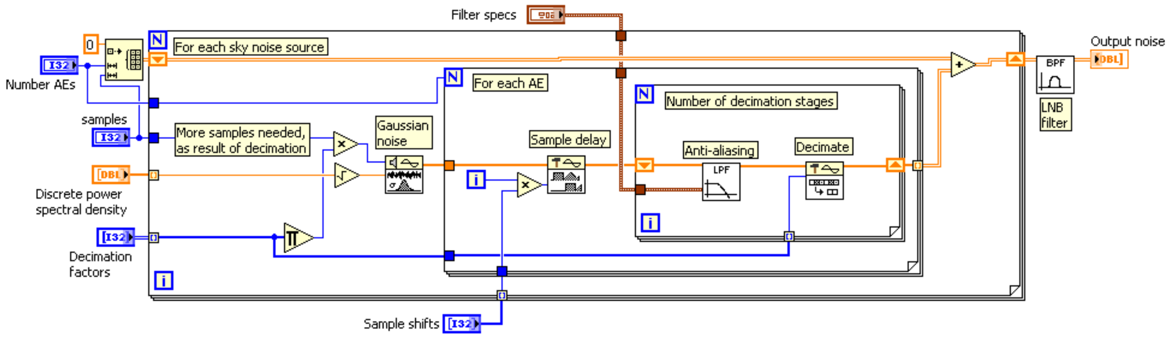

Figure 5.7: Simplified LabVIEW implementation of sky noise. For each sky noise source, a noise signal is generated which is delayed by a different amount of samples for each AE. After delaying the signals, they are decimated to fit the system sample rate, and band-pass filtered to simulate the behavior of the LNB.

unit. The latter two define the difference in time delay $\Delta\tau$ between two adjacent AEs, and subsequently determine the angle of incidence θ (compare with Eq. 2.3)

$$\sin(\theta) = \frac{c\,\Delta\tau}{d} = \frac{c\,T_\mathrm{s}\,k}{d\,M}, \tag{5.7}$$

where c is the speed of light, d the distance between adjacent AEs, T_s the system sample time, k the sample shift unit and M the decimation factor. An overview of resulting angles for multiple decimation factors and sample shift units can be found in Table 5.1. The number of decimation stages (for-loop iterations) is adjustable and follows from the decimation factors. When the noise signals are downsampled to the system sample rate, the signals are band-pass filtered to simulate the behavior of the LNB. Recall that the satellite signal does not have to be band-pass filtered, since only in-band subcarriers are generated. Furthermore, note that the anti-aliasing filter is not combined with the BPF, since the anti-alias filtering occurs before downsampling and the band-pass filtering afterwards. As the requirements on the BPF are a lot more strict than the requirements on the anti-alias filter, the filters can better be split since increasing the sample rate for the BPF would increase its order drastically.

The scheme in Figure 5.7 generates the received noise signal for a linear array of AEs. For multiple linear arrays, the noise signals will be duplicated, since there is only one degree of freedom that is taken into account. When two degrees of freedom are taken into account, the determination of the decimation factors becomes quite complex as the relation between the time delay difference and angle of incidence is not linear.

The decimation filters and LNBs that are used in the simulation environment are based on the Kaiser window. The filter coefficients are determined automatically, based on the frequency requirements that can be specified. Quick evaluations have shown flat magnitude responses and linear phase transfers. A more efficient or better designed filter might be available, but this has not been investigated. For now, it has been chosen

Table 5.1: Angles of incidence in degrees, related to the decimation factor M and the unit sample shift k.

		k				
		1	2	3	4	5
M	1	-	-	-	-	-
	2	48.27	-	-	-	-
	3	29.84	84.28	-	-	-
	4	21.91	48.27	-	-	-
	5	17.37	36.66	63.58	-	-
	6	14.40	29.84	48.27	84.28	-
	7	12.31	25.24	39.77	58.53	-
	8	10.75	21.91	34.04	48.27	68.88
	9	9.55	19.37	29.84	41.56	56.02
	10	8.58	17.37	26.60	36.66	48.27
	11	7.80	15.75	24.02	32.87	42.72
	12	7.14	14.40	21.91	29.84	38.45
	13	6.59	13.27	20.15	27.34	35.03
	14	6.12	12.31	18.65	25.24	32.21
	15	5.71	11.48	17.37	23.45	29.84
	16	5.35	10.75	16.25	21.91	27.80
	17	5.04	10.11	15.27	20.56	26.04
	18	4.76	9.55	14.40	19.37	24.49
	19	4.51	9.04	13.63	18.31	23.13
	20	4.28	8.58	12.94	17.37	21.91

to use filters with a near to perfect response in the passband, such that the distortion occurred due to filtering can be left out of consideration. In the future, filters that correspond with the characteristics of the filters in the LNB that are actually used could be implemented.

5.2.4 Combining the generation of the satellite signal with sky noise generation

One might debate whether the approach that has been taken for the generation of sky noise should be taken for the generation of the satellite signal as well. This would provide us with satellite signals without any distortion due to phase shifting, but there would be a constraint on the possible angles of incidence. Furthermore, there is a trade-off in computational efficiency between the implementations using a phase shift or a sample shift.

The most laborious operation in the generation of signals is filtering. This operation is performed by the pulse shaping filter when generating the QPSK signal, and the anti-aliasing filter when generating sky noise. By combining the generation of the satellite signal with the generation of a single sky noise source from the same direction, the filter operations can possibly be combined. However, the satellite signal must be upsampled before combining it with the noise signal to be delayed and decimated, which is also a laborious operation due to filtering operations. An additional advantage is that the initial QPSK modulation can be performed at a lower sample rate, such that a smaller total number of samples have to be processed by the pulse shaping filter.

In order to determine whether it is advantageous to use a sample shift, a consideration concerning the filtering operations should be made. Using sample shifts will increase the computational efficiency of the pulse shaping filter, but then again an additional filtering operation must be performed during the upsampling operation. Keep in mind that the required sample rate will probably be quite high, since it must be an integer multiple of both the delays between individual linear arrays, and the delays between individual AEs within a linear array. We must therefore find the greatest common divisor, such that the delay for all AEs can be realized at the same sample frequency. The exact consequences for the computational efficiency have not been investigated and is not further considered in this thesis.

5.3 Decoding a selected channel

In Section 5.1 it was explained that the transmitted satellite signal consists of multiple subcarriers that are all QPSK-modulated. The first task in retrieving the information signal is to select a channel, by means of a tuner. In Figure 2.17 we saw that this is done with a tunable LO which serves as a mixer, and a BPF fixed at a center frequency of 479.5 MHz that has a passband width of 33 MHz. After the selection of the channel, the signal is decoded and retrieved. The combined operation of tuning and decoding is performed in the modem, as shown in Figure 2.1.

Since the implementation shown in Figure 5.3 omits channel coding, the only action that need to be taken in the decoder is the QPSK demodulation. Two different approaches for demodulation have been taken. The first approach considers an integrate-and-dump filter, whereas in the second approach the signal is sampled after being passed through a matched filter. Both approaches are depicted in Figure 5.8.

In the demodulation process, the in-phase and quadrature channels are first retrieved by mixing the QPSK signal with respectively a cosine and a sine. After mixing the baseband signals are obtained. Note that the phase of the LO must be aligned manually in the simulator with the phase of the QPSK signal. From this point on, the processing of the signals differs for the two approaches that have been taken. In Figure 5.8(a) the signal is integrated over one symbol time, making the detection less susceptible to time jitter. Afterwards, the sign operation makes a decision based on a threshold of zero. In Figure 5.8(b) the quadrature signals are first processed by a matched filter (MF) to maximize the SNR, after which the signal is sampled in the middle of each symbol. Just as with the first approach, a sign operator makes a decision based on the threshold of zero. The final step is the conversion of two parallel bit streams to a serial bit stream, consisting of all the message bits.

5.3.1 Implementation in LabVIEW

The implementation in LabVIEW is a little bit different from the actual implementation, to reduce the computational burden on the simulator tool. The tuner is not working with a tunable mixer and a fixed BPF, but with a tunable BPF. Since the BPF inserts thermal noise, a Gaussian noise is added before the filter, such that the noise will be band-limited as well. The LabVIEW implementation of the BPF is combined

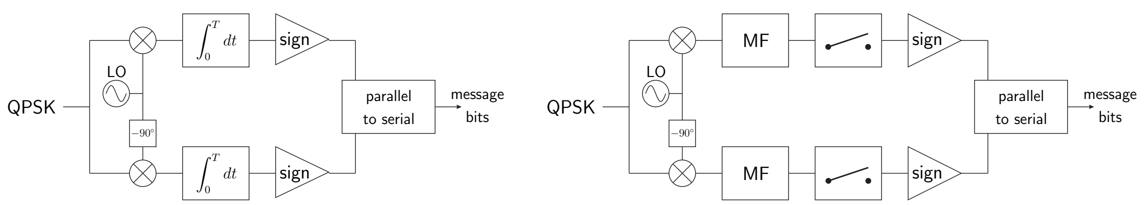

(a) QPSK receiver with an integrate and dump filter

(b) QPSK receiver, sampling the quadrature channels after matched filtering

Figure 5.8: QPSK demodulation schemes. The sign operation indicates a decision device, based on a threshold of zero.

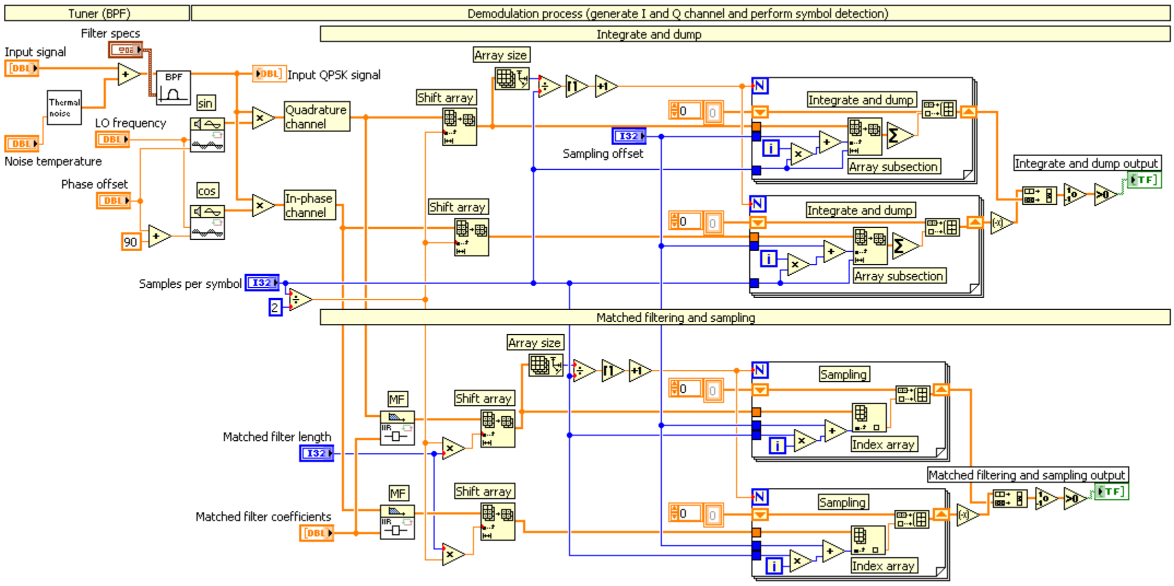

Figure 5.9: Simplified LabVIEW implementation of the demodulation processes

with the demodulation process that is shown in Figure 5.9.

The demodulation of the QPSK is not implemented with the standard blocks of LabVIEW. The blocks that LabVIEW provides are more advanced than needed for this application and therefore it is hard to get insight in the actual operations that are performed inside and to tune the block correctly. To keep our model transparent, it has been chosen to model our own demodulator. Both the approaches mentioned in Section 5.3 are executed in parallel. Figure 5.9 shows the simplified LabVIEW implementation.

With the LO and the mixers, the selected QPSK signal is downconverted to baseband. The filtering operations that are included in the model, such as band-pass filtering for the channel selection and matched filtering at the receiver, induce a delay in the signal. This delay is the result of the transient response of the filter. To make sure that the detection occurs over the right interval, these delays are compensated for. The delays inserted by the OBFN and at the generation of the signal are neglected, since they will comprise only a few samples. Furthermore, it is important that the phase of the mixing carriers is aligned with the QPSK signal. It is hard to predict the exact phase of the signal, but this can be manually aligned in the simulator. The upper process shows that in a for-loop the samples within one symbol time are integrated and dumped in an output array. In the lower process, the quadrature signals are first matched filtered with the coefficients used for the pulse shaping filter. In the for-loops, the signals are sampled in the middle of the symbol and dumped to an output array. For both the upper and lower process, the output arrays are interleaved to obtain parallel to serial conversion. Using a sign operation, a boolean array with message bits results.

Note that, the filtering operations by the BPF and the matched filter, show transient responses. This results in a delay for the signals To make sure that no information is lost during these operations (due to the finite length of the signal array) guard bits must be added at the end of the signal in the modulation process. Furthermore, it is quite important that the delays added by filtering are recognized and compensated for. Otherwise the sampling operation will occur at the wrong instant and the integration process might involve half symbols.

5.4 System simulation

In Figure 5.10 multiple graphs are shown that illustrate the operations on the signals throughout the system. The simulation has been executed using a linear antenna array with 8 AEs. Therefore, an 8×1 OBFN is used to synchronize the signals.

In Figure 5.10(a) the individual signals of the AEs are shown in the IF band, that illustrate the time delays resulting from the angle of incidence. Since a flat array is used, the delays between the signals are identical, as shown in the figure.

After the IF signals are converted to the optical domain, the signals must be synchronized and combined by the operation of the OBFN. Figure 5.10(b) shows the path delays for each input. Note that the normalized delays are not evenly spaced, which results from the fact that for each ORR a minimum normalized delay of 1 RTT is introduced, as explained in Section 4.2.2. The magnitude of the complex envelope for both a single input and the output of the OBFN is shown in Figure 5.10(c). The inputs of the OBFN are theoretically added with a factor $1/\sqrt{N}$, with N the number of inputs, resulting in an amplification of $\sqrt{8}$. In the figure the amplification is more or less a factor 2, instead of $\sqrt{8}$. This results from the fact that the group delay curves are not completely flat in the band of interest, and from noise in the signal.

Figure 5.10(b) shows that the delays are only constant for a certain frequency range, which encompasses a single sideband. The faulty sideband is removed by the OSBF after the beamforming operation, as shown in Figure 5.10(d). In the figure it is shown that the left sideband is almost completely unattenuated, whereas the right sideband is almost completely removed, which is expected from the frequency response shown in the figure.

After the optical signal is converted back to the electrical domain, a single channel is selected for demodulation in the decoding process. The specified channel is filtered out by a BPF, that removes all other carriers, as shown in Figure 5.10(e). The figure shows that one carrier is passed unattenuated, and the others are suppressed, as expected. In the demodulation process the quadrature channels of the QPSK signal are obtained, of which one is shown in Figure 5.10(f), and are used to determine the message bits, as explained in Section 5.3.

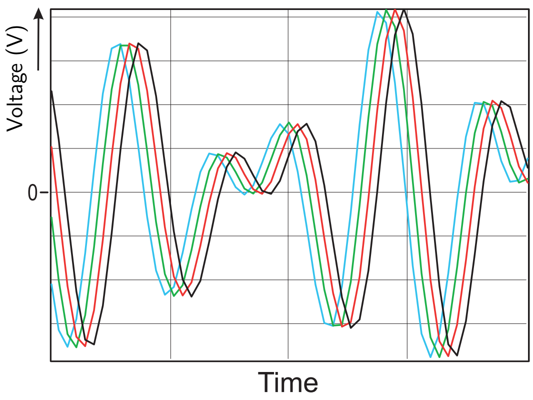

(a) QPSK signals from 8 LNBs, for which the signal is shown partly. A constant delay between the signals is observed.

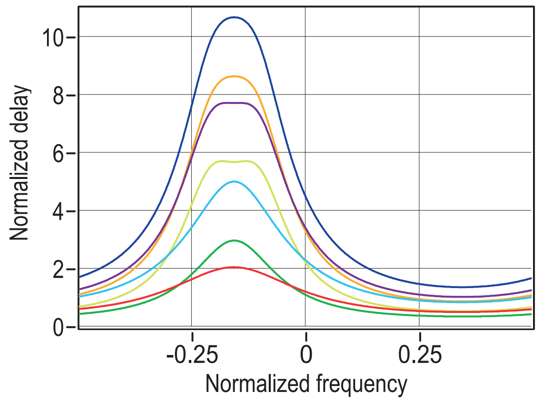

(b) Group delay response of the OBFN, showing the path delays for each of the AE signals.

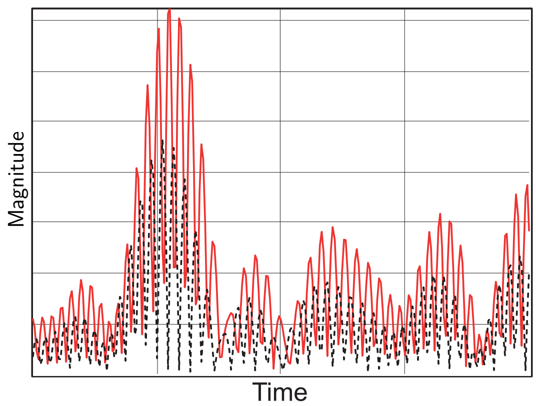

(c) Magnitude of the complex envelope of a single OBFN input, and the magnitude of the OBFN output. The magnitude of the output is the sum all the magnitude of all inputs, which are scaled by a factor $1/\sqrt{8}$.

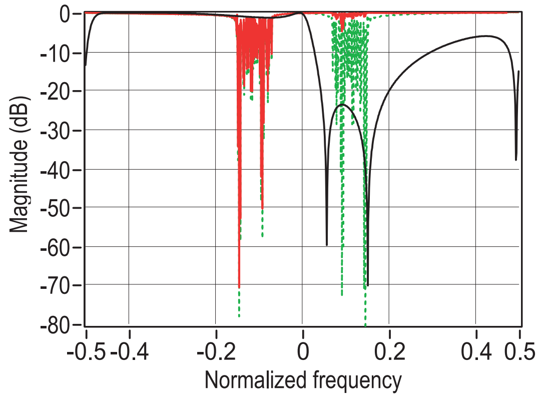

(d) Magnitude response of the OSBF, with the negated and scaled spectra of the signals before and after filtering added to the figure. Observe that one sideband is almost completely removed, and the other is passed unattenuated.

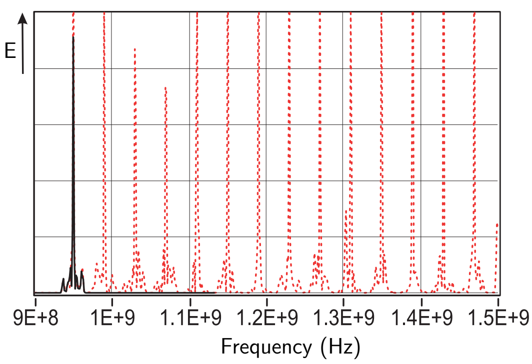

(e) Bandpass filtering to select the first channel for demodulation. The dotted line shows the spectrum before filtering, and the solid line the spectrum after filtering.

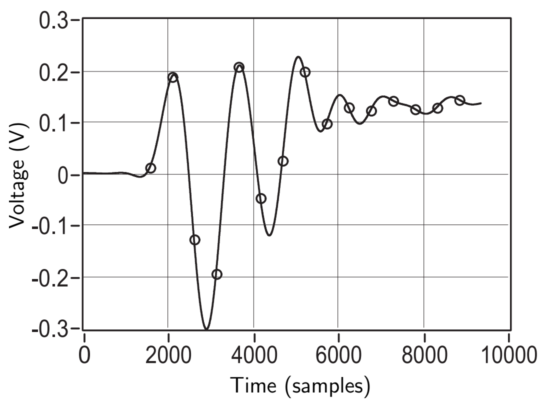

(f) One of the two quadrature channels that results after matched filtering. The circles indicate the sampling instants on which the message bits are retrieved.

Figure 5.10: Multiple figures that show the signals throughout the system, and the operations performed on the signals, for an 8×1 PAA simulation run. The dotted lines show the input signals and spectra, whereas the solid lines represent the output signals and spectra.

5.5 Summary

In this chapter the context for the optical beamformer has been described. This context defines the signals which are processed by the optical beamformer and will be used for simulation tests. We started our discussion with the definition of the DVB-S standard. Subsequently, the realization of the received signal in LaBVIEW was discussed. Instead of generating the RF signals that are picked up by the AEs, it was shown that is computationally more efficient to directly generate the output signals of the LNBs. This does not affect the system performance, but does increase the efficiency of the model by omitting the necessity of an equivalent baseband representation and by only generating those subcarriers that remain after the filtering operation in the LNBs.

Except for the desired satellite signal that is received by the AEs, sky noise is picked up. It has been explained where sky noise originates from, and how this can be modeled. An important observation was that sky noise can be coherent too — just as the received satellite signals— which influenced the design method for the noise sources. It was shown that delays in the sky noise signals have to be realized by sample shifts, since the noise signal is broadband. After the noise signal have been generated and delayed at higher sample rates, the signals are downsampled to match the system sample rate.

After the satellite signal has been processed by the optical beamformer, one subcarrier must be selected to be decoded. Two different implementations have been shown for demodulation, using an integrate-and-dump filter, and sampling after matched filtering.

Finally, a short simulation has been demonstrated for an 8×1 OBFN, showing the operations that are performed on the signals throughout the system. It was also shown that the theoretical gain of the beamformer is not completely reached in simulations, since the group delay is not perfectly constant for the signal band of interest.

Chapter 6

Computational complexity

In developing a simulator it is important to know what the required computational time is, and how the model scales. In the previous chapter we have shown a simulation test for a small optical beamfomer, but in the future beamformers with more than 1,600 inputs must be simulated to investigate the eventual performance of the system.

In this chapter we will investigate what are the most critical blocks in the simulation model, since they determine the computational efficiency largely. For each of these blocks the input dependencies will be determined, such that we can predict the runtime for larger models and get an indication of the scalability of the model. At the end of this chapter some additional optimization possibilities will be discussed.

6.1 Determining the complexity of the model

It is quite a difficult task to determine the complexity of the whole model at once. A better approach is to determine the most critical sections in the model and determine their computational complexity. These findings will then give an indication for the scaling of the model, and indicate possible bottlenecks.

6.1.1 Specifying the complexity

The computational complexity investigates the scalability of a model. The complexity is often specified as an upper bound on the required number of operations, depending on some input n. Moreover, the required number of operations $f(n)$ can be upper-bounded by $g(n)$ multiplied by any real positive constant a. It is also possible to give a lower bound $h(n)$ on the number of operations:

$$
\begin{aligned}
f(n) &\leq a \cdot g(n), && (6.1)\\
f(n) &\geq b \cdot h(n), && (6.2)
\end{aligned}
$$

where a and b are real positive constants. A more common way to refer to the computational complexity is to say that $f(n)$ is in $O(g)$, where O means in the order of. Normally, $g(n)$ and $h(n)$ are polynomial functions such as n or n^2. A lower bound is denoted by a small o, i.e. $o(h)$.

In LabVIEW, a special profiling tool can be used to determine the computational complexity. For a simulation run, the processing time in each building block is recorded. With multiple simulations and using varying parameters, the complexity can be determined. This tool can be found in the tools drop-down menu under Profile, and is called Performance and Measurement.

The number of message bits that is used for simulation, ranges from 0 to 500. The resulting number of samples can be more than 100,000 in various places in the simulator. Furthermore, OBFNs with 4, 8 and 16 inputs and a single output have been tested. No more than 16 inputs are simulated per OBFN, since the implementation of the OBFN is now limited with a maximum of five ORRs per delay element; see Section 4.2.2. The number of inputs that could be used for testing was upper bounded by its relation to a maximum number of five ORRs per delay element that can be simulated. In Figure 4.7 we have seen that we can use multiple OBFNs for planar arrays, and we can use this to determine the complexity of planar arrays as well.

6.1.2 Critical blocks

The most critical building blocks are found to be:

1. QPSK modulation;
2. upconversion;
3. generation sky noise;
4. LNBs;
5. MZMs;
6. determining the ring settings;
7. OBFN.

QPSK modulation

There are two important input parameters that both show a linear relation with the complexity. Depending on the number of samples per bit, the total number of samples can be found using the number of input message bits.

In this block, pulse shaping and QPSK modulation are performed. The dependencies are:

- number of channels	$O(n)$
- number of samples	$O(n)$

Note that the computational time mainly depends on the filter operation for baseband pulse shaping. Therefore, the contribution of this block can be neglected when no pulse shaping is used.

Upconversion

This operation upconverts the baseband QPSK signals to the IF band. Each subcarrier has to be upconverted using its own carrier frequency, after which the signals are added. Since the delays are partially implemented with phase shifts, the upconversions are executed separately for each AE. The dependencies are found to be:

- number of channels	$O(n)$
- number of samples	$O(n)$
- number of AEs	$O(n)$

Generation sky noise

The complexity of sky noise generation is mainly influenced by the filter stages. Low-pass filters are used as anti-aliasing filters and a BPF is used to simulate the behavior of the LNB to bandlimit the output. The complexity can best be characterized by the operations of the LPF and BPF, since they are the most laborious.

The dependencies of the LPF are found to be:

- filter order	$O(n)$
- number of decimation stages	$O(n)$
- number of sky noise sources	$O(n)$
- number of samples	$O(n)$
- number of AEs	$O(n)$

The dependencies of the BPF are found to be:

- filter order	$O(n)$
- number of samples	$O(n)$
- number of AEs	$O(n)$

Note that the filter order and number of decimation stages are interrelated. It seems attractive to use as little decimation as possible, but this will make the order of the filter increase more than proportional.

LNBs

In the LNBs, thermal noise is added to the signal and the signal itself is multiplied by a gain. The BPF in the LNB limits the bandwidth of the noise and is the most laborious operation. The dependencies of the BPF are similar to those found for the generation of sky noise:

- filter order $O(n)$
- number of samples $O(n)$
- number of AEs $O(n)$

MZMs

This operation modulates the electrical IF signals onto the optical carriers. For the MZMs two dependencies are found:

- number of samples $O(n)$
- number of AEs $O(n)$

The total number of AEs depends on the number of linear arrays and the number of AEs per linear array.

Ring settings

This block is implemented in [18] and mainly depends on the total number of ORRs in the OBFN, but also on the number of ORRs per delay element. The complexity is found to be:

- number of ORRs in the OBFN $o(n)$–$O(n^2)$

Note that the number of ORRs is related to the number of AEs. Furthermore, in the current implementation we assume flat planar arrays, such that OBFNs 1–4 in Figure 4.7 all use the same values. For conformal arrays, the algorithm must be called for each OBFN individually. The complexity relation shows that the determination of the ring settings is independent of the number of samples. This shows that this operation can be performed separately from the simulation run, and may be implemented as an initialization step.

OBFN

The computational efficiency of an OBFN is mainly influenced by the individual ORRs, and thus the total number of ORRs. The dependencies are found to be:

- total number ORRs in the OBFN $O(n)$
- number of samples $O(n)$

Note that the number of ORRs is related the the number of inputs, which equals the number of AEs. Therefore, the OBFN complexity is indirectly dependent on the number of AEs.

6.1.3 Extrapolation of the complexity relations

We have to keep in mind that the relations found in Section 6.1.2 will not hold for infinite scaling. At a certain moment a maximum size of arrays and matrices will be reached, and buffers will be full. Depending on the operating system and the simulation software additional computational time will be required to cope with large arrays and matrices, which will lead to time requirements larger than expected.

In LabVIEW there is a tool called Show Buffer Allocations which allows for the investigation of the array and buffer sizes. This tool is found under Profile in the Tools drop-down menu. This tool can be used to identify bottlenecks in the simulation and to determine whether the limits of arrays and buffers are reached.

6.2 Indication of the required computational time

Using the complexity relations found in Section 6.1.2, we can extrapolate from relatively small simulations to an idea about the required computational time for larger simulations. The following simulation has been performed on a computer with a 3.0 GHz dual-core Pentium processor and 1.0 GB of RAM, and will give an indication of the required time for future simulations. Note that the timing characteristics are strongly related to the utilized hardware, but do give some insight on the necessary computational time on other platforms as well.

Suppose that we consider a PAA with 16×16 AEs, and we are using pulse shaping and omitting sky noise, since the implementation is not completely accurate for planar arrays. The satellite signal is considered to consist of 20 channels, of which each contains a message of 100 bits. Multiple OBFNs are used, as shown in Figure 4.7. Using the profiling tool of LabVIEW the following timing results are obtained:

QPSK modulation	6.2 s
Upconversion	10.6 s
LNBs	15.1 s
MZMs	8.4 s
Determining the ring settings	4.0 s
OBFN	14.0 s
Remainder, unaccounted LabVIEW time	9.0 s
Total	67.3 s

Example 6.1

If we want to estimate the computational time needed for a PAA with 64×32 AEs, all critical blocks that have dependencies regarding the number of AEs must be accounted for. The new computational times can be calculated by taking the increase in AEs into account.

QPSK modulation This operation is not dependent on the number of AEs and the required computational time will remain the same.

Upconversion The number of AEs in a PAA of 64×32 will be 8 times as large compared to a PAA with 16×16 AEs. Since, the upconversion operation has a linear dependency on the number of AEs, the required computational time will increase by a factor 8. Therefore, the new contribution equals $8 \times 10.6 = 84.8$ seconds.

LNBs The complexity relations of the LNBs show a linear relation to the number of AEs. Therefore, the new required time is $8 \times 15.1 = 120.8$ seconds.

MZMs The MZMs also show a linear dependency on the number of AEs. Therefore, the new contribution of the MZMs will be $8 \times 8.4 = 67.2$ seconds.

Ring settings The determination of the ring settings shows a dependency that has a linear lower bound and a quadratic upper bound. Therefore, it is not easily said what the new contribution will be. However, we can make an estimation. For a PAA of 16×16 AEs, the algorithm is called twice to find the settings for a 16×1 OBFN. From this we can conclude that the required time for a single call of the algorithm is 2 seconds.

Extrapolating from an 8×1 OBFN, with respectively 1, 1 and 2 ORRs in its stages, the number of ORRs in larger OBFNs can be determined. The number of ORRs in a 64×1 OBFN is then 112 and is a factor 5.6 times the number of ORRs in a 16×1 OBFN, which equals 20. In a 32×1 OBFN a total of 48 ORRs can be found.

The dependency on the number of rings is larger than linear, but smaller than quadratic. Therefore, a minimum and maximum is given. The minimum total required time will be the sum of both calls to the algorithm and equals $(2 \times 5.6) + (2 \times 2.4) = 36$ seconds. The maximum required time will be $(2 \times 5.6^2) + (2 \times 2.4^2) \approx 74.2$ seconds.

OBFN The total number of ORRs for a 64×32 OBFN is $112 \times 32 + 48 = 3632$. The number of ORRs in a 16×16 OBFN equals $20 \times 16 + 20 = 340$. Thus, the number of ORR has increased by a factor of 10.7. Therefore, the newly required time by the OBFN block will be $10.7 \times 14.0 = 149.8$ seconds.

Total Now, the newly calculated computational times can be used to determine the total required time for a 64×32 simulation.

QPSK modulation	6.2 s
Upconversion	84.8 s
LNBs	120.8 s
MZMs	67.2 s

Determining the ring settings	16.0–74.20 s
OBFN	149.8 s
Remainder, unaccounted LabVIEW time	9.0 s
Total	453.8–512.0 s

6.3 Possible optimization

The deducted complexity relations of the developed blocks in LabVIEW are mostly found to be linear. Possibilities for optimization are to reduce the number of dependencies for each block, or to develop an implementation such that a smaller value for a in Eq. 6.1 can be found.

It is for example interesting to investigate whether it is useful to simulate all channels or not. When the channels are spaced far apart, they will hardly influence each other. Therefore, a simulation with a small number of channels will probably suffice. Furthermore, the required number of sky noise sources to accurately represent the sky can be investigated. A last example is the determination of the influence of noise sources. If these appear negligible, they can be omitted in the simulation model.

Since the performance of the simulator tool will in the end depend a lot on the required and available resources, it is advantageous to optimize the buffer usage in LabVIEW and investigate other benefits of the simulation environment. One of the possibilities is to use multi-threading, which is beneficial for multi-core processors since multiple processes are run in parallel.

Finally, some improvements can be made in the modeling of the filters that are used. Both the LPFs and BPFs are probably over-dimensioned, such that any distortion by the filters can be let out of consideration as mentioned in Section 5.2.3. By investigating other design methods it is most probable that a lot of efficiency can be gained. The importance of this is also indicated by the timing results of the LNBs shown in Section 6.2.

6.4 Increase in complexity for more advanced models

Throughout this thesis several simplifications have been introduced to enhance the computational efficiency of the model. On one hand, certain effects have been omitted since they proved to be negligible in theory, and on the other hand some adaptations to the model have been introduced to simplify the implementation. Next, a discussion will follow on some of these simplifications, indicating what the effect on the complexity will be when more advanced models are used.

MZM

The current implementation of the MZM is based on a formula describing the ideal operation. When differences in arm lengths and imbalances must be considered, a more advanced model using DCs and phase shifters can be used to simulate the actual behavior of the MZM. Since the optical signal uses an equivalent baseband representation, phase shifts are easily introduced by means of additions. Also, the function performed by the DCs consists of basic operations. Therefore, the number of operations that must be performed by the simulator will likely not differ a lot from the current implementation.

LNB

The output of the LNBs is now directly generated, based on some parameters that specify the satellite signal. When the actual operation of the LNBs must be incorporated, amplification, filtering and downconversion operations must be added, as well as the usage of an equivalent baseband representation of the RF satellite signal. Especially the filter operations that are added will require a lot of computational time. However, one such filter is already used for limiting the bandwidth of the noise that is added by the LNB, and is thus already present.

Another consequence of the implementation of the LNB is that probably also frequency channels will be generated, that are filtered out later on. This will not only require extra time for the generation, but also for the realization of the correct delays for the extra channels.

Laser

RIN and phase noise can easily be added to the laser model. Since only a single laser signal has to be generated, the effect on the computational efficiency will be marginal. However, to keep the signals coherent, an actual splitting network must be used, instead of reusing a single array that is generated in the case of a constant optical. The splitting network is described in Section 4.4. Since the splitting and rearranging of the arrays in LabVIEW is computationally heavy, the efficiency of the model will decrease. Note that the usage of the splitting network will also enable the implementation of amplitude tapering.

DVB-S signal

The actual DVB-S signal does not have equal channel bandwidths for the complete frequency range. The implementation of the exact signal will not largely influence the computational efficiency of the model, but does make it a lot more complicated. A lot of extra parameters are needed, as well as a lot of small extra operations that must be performed, such that the realized signal will match the actual frequency spectrum of the DVB-S signal.

6.5 Summary

In this chapter the complexity of the model has been determined, by specifying the complexity relations of the most critical blocks in the simulation model. It was shown that most of the dependencies are linear, except for the determination of the ring settings. However, the contribution to the total computational time of this block is small, and therefore the simulation model is found to have a near to linear complexity. It was demonstrated how one can extrapolate from relatively small simulation to large simulation, by using the complexity relations.

Several possibilities for optimization have been discussed to make the simulator more efficient. Probably, the largest gain in efficiency can be made by improving the decimation filters used for the generation of sky noise, and the BPFs in the LNBs and the modem. Furthermore, an indication is given on the effects of using more advanced models for several blocks in the simulation model.

Chapter 7

Conclusions and recommendations

7.1 Conclusions

In this thesis a simulator tool has been developed to simulate optical beamformer systems. The manual for this tool can be found in Appendix C. In the design process the specific application of airborne satellite reception has been taken as a pilot application. From this application we can generalize to other applications in RF photonics, such as beamforming for radio astronomy.

It was shown that LabVIEW offers a good simulation environment for the development of the simulator tool. Compared to dedicated software packages, LabVIEW offers flexibility in specifying the signal representation. This enables a suitable optical signal representation, such that interference effects can be simulated, and is convenient for simulations concerning multiple domains, as required in RF photonics.

Within LabVIEW a full system model has been realized of the optical beamformer system. For each of its components it has been decided to what extent effects and noise must be taken into account. To be able to test the optical beamformer system, a context has been defined that applies to the application of airborne satellite reception of the DVB-S signal. By using a dynamical implementation, we have created a flexible system that can be used to simulate PAAs with any number of AEs. An integral part of the simulator tool that is required for performing simulations, is the generation of the ORR settings, which was developed in [18]. However, this integral part currently limits the possible OBFN network structures insofar that a maximum of five ORRs per delay element can be used.

It is concluded that a fixed system sample rate of 13.4 GHz, which is matched on the FSRs of the ORRs in the OBFN, is suitable for optical beamformers. This rate enables the simulation of the behavior of ORRs in a simple way. Furthermore, the sample rate is large enough to encompass the signal bandwidth, such that an equivalent baseband representation can be used to represent optical signals and to reduce the total number of required samples.

The reception of DVB-S by the AEs results in multiple signals which are time-delayed versions of each other. It was shown that the usage of phase shifts is a suitable way to realize these delays, while retaining the possibility to perform simulation for any angle of incidence. To minimize the distortion, each subcarrier of the satellite signal is delayed separately. Furthermore, it was shown that delayed sky noise signals must be realized by sample shifts, since these are broadband. To be able to realize the correct delays, the noise is generated at a higher sample rate, delayed and subsequently downsampled to match the system sample rate of 13.4 GHz. It is concluded that this is a suitable way to realize the delays in the sky noise signals.

The scalability of the simulator tool has been investigated by means of computational complexity relations. It is concluded that the realized simulator tool is suitable for real-size system simulations with a reasonable number of message bits. The complexity relations can be used to extrapolate from smaller simulations, to get an indication on the required computational time for larger systems. It was shown that a simulation for a system with more than 2,000 AEs, employing a QPSK signal of 100 message bits can be performed within ten minutes. Note that the usability is dependent on the calculation of the ORR settings, since the performance of the system depends largely on this and which is inherent to the system.

Except for the specific application of airborne satellite reception, it is concluded that the simulator tool can be used for other RF photonics systems as well. This is deduced from the fact that a suitable signal representation has been shown for both electrical and optical signals, enabling cross-domain simulations. Furthermore, a lot of realized building blocks are common within RF photonics systems, such as Mach-Zehnder modulation and detection using photodiodes, but RF processing functions such as optical filtering by means of ORRs —with multiple in and outputs— as well.

7.2 Recommendations

The research and modeling work that has been carried out for this thesis is part of ongoing research within the TE group. To be able to use the acquired knowledge and simulator tool to its full extent, some directions for further research are given here.

Performance analysis

In this thesis all components in the satellite receiver system have been modeled and tested. The next step is to perform full system simulations.

- In the performance analysis done in [22] a lot of assumptions were made in the derivations. It was recommended to check the analytical results by simulation, which is now possible with the use of the developed simulator tool. It should be checked whether the simulator behaves as expected for full system simulations, and if the theory matches the simulation results.

- In [9, 10] measurements on optical beamformer chips have been presented. It is recommended to use the simulator tool to identify the differences between measurements and simulations, such that the simulation model can be improved and inaccuracies in the device can be located.
- The synchronization in the decoder of the mixing carrier and detected signal should be checked. The alignment and filtering delays should be compensated correctly, to get an accurate decoding operation which is needed for performance analysis.

Extending the usability of the model

In this thesis we have developed a simulator tool that comprises the most important aspects for the simulation of optical beamformers. There are, however, still a number of expansions that can be added to the model.

- It is recommended to implement performance metrics, such as the BER, the CNR. The implementation of this offers enables extensive evaluation of the system.
- LabVIEW has the ability to perform co-simulations, combining hardware and software. This means that various parts in the simulator model can be replaced with actual fabricated chips and PCBs. It is recommended to exploit this strong combination, which enables a good evaluation of the performance and helps in the detection of possible bottlenecks in the system design.
- Since the individual gains of the AEs are small, a lot of elements are needed to provide sufficient gain. With the simulator tool it is possible to easily upscale the model and simulate a real-size system. However, the size of the delay elements in the OBFN network structure that can be simulated is bounded by the software developed in [18]. Therefore, it is recommended to research the calculation of ring settings for larger network structures.
- By implementing radiation patterns for AEs (directive gains for signal reception), suppression and amplification of signals in the OBFN can be compared with the analysis on radiation patterns of PAAs. Therefore, it is recommended to do research on the radiation patterns of array antennas.
- It should be checked whether the RIN and phase noise in the laser can indeed be neglected. For this the laser block should be replaced with a more advanced model.
- By the usage of amplitude tapering, a better radiation pattern of the PAA can be obtained, enabling the suppression of sidelobes. To investigate this, weighting factors must be introduced for the AE signals.

- It is recommended to investigate the possibility to research wavelength division multiplexing (WDM) systems with the simulator tool. With the usage of WDM, it is possible to reduce the number of required OBFN network structures since they can be used for multiple wavelengths simultaneously. This work is part of the MEMPHIS project [49, 41].
- In the actual implementation conformal antenna arrays will be used on aircraft, instead of flat PAAs. It should be investigated how this affects the performance of the system, by modeling the conformal arrays accordingly.
- Newer standards appear for the definition of DVB-S, that use other modulation methods than QPSK. It is interesting to know what the performance of the system will be for newer standards such DVB-S2, employing for example 8-PSK. Therefore, other modulation methods should be included as well.

Increasing the computational efficiency

Since the system that is modeled is quite complex, it is advantageous to increase the efficiency of the simulator as much as possible and use the available resources to their full extent.

- A first step in utilizing all resources is multi-threading. Nowadays, most of the processors are multi-core allowing multiple separate processes to be executed in parallel. With LabVIEW this possibility can be exploited, but requires some changes to the implementation of the model. Especially for more critical blocks in the model a lot might be gained regarding computational efficiency.
- It should be investigated whether the computational efficiency of the filters that are used can be increased. The current implementation employs over-dimensioned filters, such that any distortion introduced by the filters can be left out of consideration. Moreover, the response of the implemented bandpass filters should match the behavior of the filters in the actual LNBs and modems, and decimation filters should be designed such that they do not introduce any unwanted effects, but are as efficient as possible.
- It is possible to combine the generation of the satellite signal with the generation of a sky noise source from the same direction. Whether or not this combination increases the computational efficiency should be investigated. However, recall that this will reduce the tunability of the angle of incidence to a discrete number, but the advantage is that a complete distortion-free signal is generated.

References

[1] W. Chang, *RF photonic technology in optical fiber links.* Cambridge University Press, 2002.

[2] (2009, Apr.) Telecommunication Engineering. [Online]. Available: http://www.el.utwente.nl/te

[3] (2009, Apr.) SenterNovem. [Online]. Available: http://www.senternovem.nl/english

[4] (2009, Apr.) SMART. [Online]. Available: http://pideaplus-smart.org

[5] L. Zhuang, C. Roeloffzen, and W. van Etten, "Continuously tunable optical delay line," in *Proc. of the 12th IEEE/CVT Symp. in the Benelux*, Enschede, The Netherlands, Nov. 2005.

[6] C. Roeloffzen, L. Zhuang, R. Heideman, A. Borreman, and W. van Etten, "Ring resonator-based tunable optical delay line in LPCVD waveguide technology," in *Proc. of the 9th Anual Symposium of IEEE/LEOS Benelux Chapter*, Mons, Belgium, Dec. 2005, pp. 79–82.

[7] L. Zhuang, C. Roeloffzen, and W. van Etten, "Ring resonator-based continuously tunable optical delay line," in *URSI Benelux Meeting*, Eindhoven, The Netherlands, May 2006, p. 23.

[8] R. Heideman, A. Melloni, M. Hoekman, A. Borreman, A. Leinse, and F. Morichetti, "Low loss, high contrast optical waveguides based on CMOS compatible LPCVD processing: technology and experimental results," in *Proc. of the 9th Annual Symposium of the IEEE/LEOS Benelux Chapter*, Mons, Belgium, Dec. 2005, pp. 71–74.

[9] L. Zhuang, C. Roeloffzen, R. Heideman, A. Borreman, A. Meijerink, and W. van Etten, "Single-chip optical beam forming network in lpcvd waveguide technology based on optical ring resonators," in *Proceedings of the International Topical Meeting on Microwave Photonics (MWP'2006)*, Grenoble, France, Oct. 2006, pp. 1–4.

[10] L. Zhuang, C. G. H. Roeloffzen, R. G. Heideman, A. Borreman, A. Meijerink, and W. van Etten, "Single-chip ring resonator-based 1×8 optical beam forming network in cmos-compatible waveguide technology," in *NIRICT Kick-off congress*, Utrecht, The Netherlands, Mar. 2007, pp. 1130–1132.

[11] A. Meijerink, C. G. H. Roeloffzen, L. Zhuang, D. A. I. Marpaung, R. G. Heideman, A. Borreman, and W. van Etten, "Phased array antenna steering using a ring resonator-based optical beam forming network," in *Proceedings of the 13th Symposium on Communications and Vehicular Technology in the Benelux*, Liege, Belgium, Nov. 2006, pp. 7–12.

[12] C. Roeloffzen, A. Meijerink, L. Zhuang, D. Marpaung, R. Heideman, A. Leinse, M. Hoekman, and W. van Etten, "Integrated photonic beamformer employing continuously tunable ring resonator-based delays in CMOS-compatible LPCVD waveguide technology," in *Asia-Pacific Optical Communications (APOC) 2008*, Hangzhou, China, Oct. 2008, pp. 7135–59, (invited).

[13] L. Zhuang, A. Meijerink, C. Roeloffzen, D. Marpaung, R. Heideman, M. Hoekman, A. Leinse, and W. van Etten, "Novel ring resonator-based optical beamformer for broadband phased array receive antennas," in *Proceedings of the LEOS Annual Meeting 2008*, Newport Beach, California, Nov. 2008, pp. 71–74.

[14] ——, "Broadband phased array antenna steering by means of coherent signal combining in an integrated ring resonator-based optical beamformer," in *Proceedings of the 13th Annual Symposium of the IEEE/LEOS Benelux Chapter*, Enschede, The Netherlands, Nov. 2008, pp. 71–74.

[15] R. Blokpoel, "Staggered delay tuning algorithms for ring resonators in optical beam forming networks," Master's thesis, University of Twente, Aug. 2007.

[16] R. J. Blokpoel, A. Meijerink, L. Zhuang, C. G. H. Roeloffzen, , and W. van Etten, "Staggered delay tuning algorithms for ring resonators in optical beam forming networks," in *Proc. of the 12th Annual Symposium of the IEEE/LEOS Benelux Chapter*, Brussels, Belgium, Dec. 2007, pp. 243–246.

[17] J. van 't Klooster, "Context, Design and Implementation of a Control System for Ring Resonator-based Optical Beam Forming Networks," Master's thesis, University of Twente, Oct. 2008.

[18] J. van Galen, "Modelation, Simulation and Implementation of an OBFN Control Software System," Master's thesis, University of Twente, unpublished.

[19] A. Garcia, "Optical phase synchronization in coherent optical beamformers for phased array receive antennas," Master's thesis, University of Twente, Feb. 2009.

[20] B. den Uyl, "Single sideband modulation for optical beam forming in phased array antennas," Bachelor's thesis, University of Twente, Aug. 2006.

[21] L. Hong, "Implementation and tuning of optical singlesideband modulation in ring resonator-based optical beam forming systems for phasedarray receive antennas," Master's thesis, University of Twente, Mar. 2009.

[22] R. Meijerink, "Performance study of a ring resonator-based optical beam forming system for phased array receive antennas," Master's thesis, University of Twente, Dec. 2007.

[23] A. Meijerink, "Coherence multiplexing for optical communication systems," Ph.D. dissertation, University of Twente, 2005.

[24] U. Reimers, *DVB: The Family of International Standards for Digital Video Broadcasting*, 2nd ed. Springer, 2004.

[25] (2009, Apr.) Europe, Africa & Middle East. LyngSat. [Online]. Available: http://www.lyngsat.com/europe.html

[26] (2009, Apr.) SES ASTRA - 19.2°. Astra — the leading provider of satellite services. [Online]. Available: http://www.ses-astra.com/business/en/satellite-fleet/19-2E/index.php

[27] J. Verpoorte, H. Schippers, and G. Vos, "Specifactions for airborne antennas for multimedia satellite communiation (project SMART)," internal report, 2005.

[28] (2009, Apr.) Microstrip antenna. Wikipedia — the free encyclopedia. [Online]. Available: http://en.wikipedia.org/wiki/Microstrip_antenna

[29] H. Schippers, J. Verpoorte, P. Jorna, A. Hulzinga, A. Meijerink, C. Roeloffzen, L. Zhuang, D. Marpaung, W. van Etten, R. Heideman, A. Leinse, A. Borreman, M. Hoekman, and M. Wintels, "Broadband conformal phased array with optical beam forming for airborne satellite communication," in *Proceedings of the IEEE Aerospace Conference 2008*, Big Sky, Montana, Mar. 2008, p. 3.0102.

[30] C. Cox, *Analog optical links: theory and practice.* Cambridge University Press, 2004.

[31] R. Heideman, D. Geuzebroek, and J. Walker, "High contrast surface waveguide technology for biochemical sensing and telecom applications," *Lasers and Electro-Optics Society, 2006. LEOS 2006. 19th Annual Meeting of the IEEE*, pp. 957–958, Oct. 2006.

[32] C. K. Madsen and J. H. Zhao, *Optical filter design and analysis.* John Wiley & Sons, 1999.

[33] W. van Etten, *Introduction to random signals and noise.* John Wiley & Sons, Ltd., 2005.

[34] (2009, Apr.) Data sheet R2860E Digital Receiver. Emcore Corporation. [Online]. Available: http://www.emcore.com/assets/fiber/R2860e.pdf

[35] *Digital Video Broadcasting (DVB); Framing structure, channel coding and modulation for 11/12 GHz satellite services*, European Telecommunications Standards Institute Std. EN 300 421 V1.1.2, Aug. 1997.

[36] *LabVIEW — the software that powers virtual instrumentation*, National Instruments Std., 2009, version 8.6.

[37] *Simulink — dynamic system simulation for Matlab*, The MathWorks, Inc. Std., 2008, version 7.2 (part of Release 2008b).

[38] S. Haykin, *An introduction to analog and digital communications.* John Wiley & Sons, Inc. New York, NY, USA, 1989.

[39] J. Reed, *Software Radio: A modern approach to radio engineering.* Prentice Hall Press Upper Saddle River, NJ, USA, 2002.

[40] A. Meijerink, L. Zhuang, C. Roeloffzen, M. Hoekman, and A. Leinse, "Functional design of the demonstrator chipset," SMART Deliverable 2.3.1, internal report, 2005.

[41] M. Burla, M. Khan, L. Zhuang, and C. Roeloffzen, "Multiwavelength Optical Beam Forming Network with Ring Resonator-based Binary-Tree Architecture for Broadband Phased Array Antenna Systems," in *Proc. of the 13th Annual Symposium of the IEEE/LEOS Benelux Chapter*, Enschede, The Netherlands, Nov. 2008, pp. 99–102.

[42] L. Kazovsky, S. Benedetto, and A. Willner, *Optical Fiber Communication Systems.* Artech House, Inc., 1996.

[43] W. van Etten and J. van der Plaats, *Principles of optical fiber communications.* Twente University Press, 2000.

[44] (2009, Apr.) Photodiode characteristics. UDT Sensors Inc. [Online]. Available: http://www.optics.arizona.edu/Palmer/OPTI400/SuppDocs/pd_char.pdf

[45] (2009, Apr.) Datasheet SPV-50 PLL LNB. Invacom. [Online]. Available: http://invacom.com/products/documents/PLLLNB.pdf

[46] ITU, "Radio Noise," Recommendation ITU-R P.372-9, 2007.

[47] C. Balanis, *Antenna theory: analysis and design.* Harper & Row, Publishers, Inc., 1982.

[48] C. Balanis and W. InterScience, *Modern antenna handbook.* Wiley, 2008.

[49] (2009, Apr.) The Memphis project. [Online]. Available: http://www.smartmix-memphis.nl/

Appendix A

OBFN structure

The OBFN is implemented in LabVIEW, using a dynamical network structure to be able to simulate beamforming networks with any number of inputs. The only requirement is that the number of inputs is a power of 2.

In order to specify this network structure, we must first introduce two concepts that are shown in Figure A.1. The number of stages m depends on the number of inputs n and is determined by $m = \log_2(n)$. A delay element consists of one or more ORRs in cascade that form a delay element.

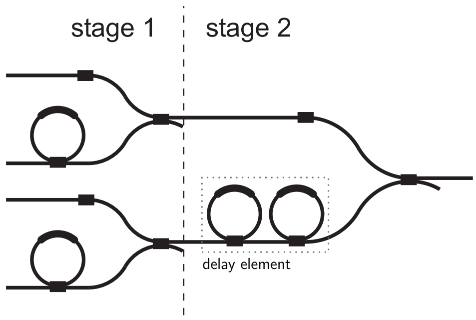

Figure A.1: Definition of a stage and a delay element in an OBFN

A.1 Defining the OBFN structure

The OBFN structure is defined by a matrix in which the rows represent the paths and the columns each represent a delay element. A path is defined from an input to the output and passes through a number of delay elements. The delay elements that are encountered appear as non-zero values in the row that represents a path. The actual value in the columns indicate the number of ORRs in a delay element. For example, the network matrix of a 8×1 OBFN is shown in Figure A.2.

The basic steps to transform a given structure into the matrix are:

1. scan through a single stage at the time;

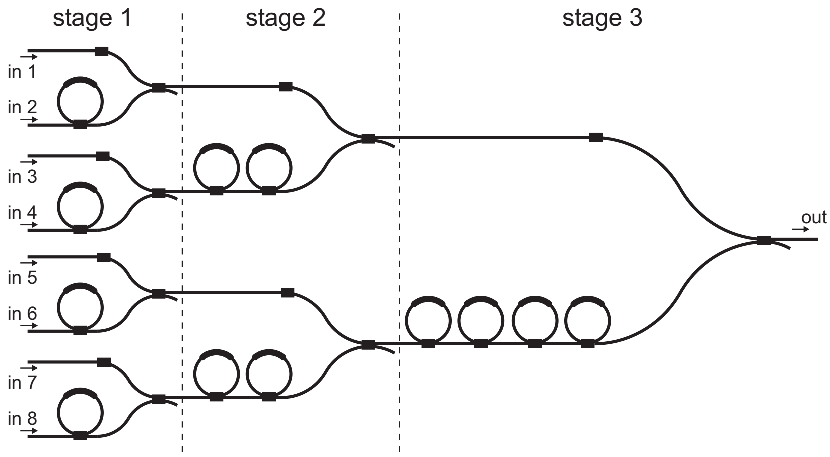

(a) 8×1 OBFN structure

0	0	0	0	0	0	0
1	0	0	0	0	0	0
0	0	0	0	2	0	0
0	1	0	0	2	0	0
0	0	0	0	0	0	4
0	0	1	0	0	0	4
0	0	0	0	0	2	4
0	0	0	1	0	2	4

(b) Input matrix that represents the 8×1 OBFN structure

Figure A.2: Network structure for an 8×1 OBFN, that is converted into a matrix equivalent that specifies the structure within the simulator.

2. consider all delay elements that are encountered, while passing along the branches;
3. use a separate column for each delay element and enter the number of ORRs within the delay element into the corresponding rows that represent a path going through that section.

The following check-up rule can be used to see if the mapping worked correctly:

- summing the values in each row gives the number of ORRs that is encountered in the designated path from input to output.

Note that multiple non-zero entries in a column defines that the delay element is encountered in multiple paths. That is why the delay elements in the first stage only a single entry.

A.2 Retrieving the ORR settings

With the LabVIEW application developed in [18] the settings for the ORRs in the OBFN can be calculated. The LabVIEW program requires several input parameters, which are:

- angle of incidence,
- number of AEs,
- AE spacing,
- RTT of the ORRs,
- normalized bandwidth of a single sideband of the signal,
- loss in the ORRs,
- OBFN structure matrix,
- array with the number of ORRs per stage,
- array with coax delays that specify the pre-delays and the offset resulting from the minimum delay in each path.

The matrix structure that describes the network structure is compatible with the structure used for the dynamical implementation. The latter two input requirements can be derived from this matrix, but must be generated manually.

The output ring settings from [18] must be converted to a new lay-out to fit with the dynamical implementation of the OBFN. Furthermore, the values themselves are converted as well, since an offset of 2π might occur, or the values need to be negated to fit the implementation.

Appendix B

Power spectral density in the discrete time domain

This appendix will show the derivation for the relation between the continuous- and discrete-time power spectral density. In Section 3.2.1 we saw that thermal noise sources can be characterized by a power spectral density. To be able to generate white Gaussian noise in the discrete-time domain, we must know the discrete-time equivalent.

In Section 3.2.2 it was shown that the discrete-time equivalent of a continuous signal can be found by means of sampling, defined as

$$\tilde{x}[n] = x(n\,T_\mathrm{s}). \tag{B.1}$$

It can be shown that discrete-time form of the autocorrelation of x equals the autocorrelation in the continuous domain:

$$\begin{aligned}
R_{\tilde{x}\tilde{x}}[m] &\triangleq E\Big[\tilde{x}[n]\tilde{x}[n+m]\Big] && \text{(B.2)}\\
&= E\Big[x(n\,T_\mathrm{s})x\Big((n+m)T_\mathrm{s}\Big)\Big] && \text{(B.3)}\\
&= R_{xx}(m\,T_\mathrm{s}). && \text{(B.4)}
\end{aligned}$$

We start our derivation with the discrete-time autocorrelation $R_{\tilde{x}\tilde{x}}[m]$. The discrete-time power spectral density follows by taking the discrete-time Fourier transform (DTFT):

$$S_{\tilde{x}\tilde{x}}(\Omega) = \sum_{m=-\infty}^{\infty} R_{\tilde{x}\tilde{x}}[m]\;\exp(-\mathrm{j}\,m\,\Omega), \tag{B.5}$$

where Ω is the normalized angular frequency variable in radians. Using Eq. B.4 and writing R_{xx} as the inverse Fourier transform of the PSD function $S_{xx}(\omega)$, we get

$$S_{\tilde{x}\tilde{x}}(\Omega) = \sum_{m=-\infty}^{\infty} \frac{1}{2\pi} \int_{-\infty}^{\infty} S_{xx}(\omega)\ \exp(\mathrm{j}\,\omega\,m\,T_\mathrm{s})\,\mathrm{d}\omega\ \exp(-\mathrm{j}\,m\,\Omega), \tag{B.6}$$

$$= \frac{1}{2\pi} \int_{-\infty}^{\infty} S_{xx}(\omega) \sum_{m=-\infty}^{\infty} \exp\Big(\mathrm{j}(\omega\,T_\mathrm{s} - \Omega)\,m\Big)\,\mathrm{d}\omega, \tag{B.7}$$

$$= \frac{1}{2\pi} \int_{-\infty}^{\infty} S_{xx}(\omega) \sum_{m=-\infty}^{\infty} \exp\left(\mathrm{j}\left(\omega - \frac{\Omega}{T_\mathrm{s}}\right) m\,T_\mathrm{s}\right)\mathrm{d}\omega. \tag{B.8}$$

The Poisson sum formula [33] allows us to replace the infinite sum of exponentials by an infinite sum of delta functions, and is given by

$$\sum_{m=-\infty}^{\infty} \exp\Big(\mathrm{j}\Psi\,m\,T_\mathrm{s}\Big) = \frac{2\pi}{T_\mathrm{s}} \sum_{m=-\infty}^{\infty} \delta\left(\Psi - \frac{2\pi m}{T_\mathrm{s}}\right). \tag{B.9}$$

Combining Eq. B.8 and B.9 results in

$$S_{\tilde{x}\tilde{x}}(\Omega) = \frac{1}{2\pi} \int_{-\infty}^{\infty} S_{xx}(\omega) \frac{2\pi}{T_\mathrm{s}} \sum_{m=-\infty}^{\infty} \delta\left(\omega - \frac{\Omega}{T_\mathrm{s}} - \frac{2\pi m}{T_\mathrm{s}}\right)\mathrm{d}\omega, \tag{B.10}$$

$$= \frac{1}{T_\mathrm{s}} \sum_{m=-\infty}^{\infty} \int_{-\infty}^{\infty} S_{xx}(\omega)\,\delta\left(\omega - \frac{\Omega}{T_\mathrm{s}} - \frac{2\pi m}{T_\mathrm{s}}\right)\mathrm{d}\omega. \tag{B.11}$$

Using the sifting property of the delta function, the delta function can be removed such that the spectral density becomes

$$S_{\tilde{x}\tilde{x}}(\Omega) = \frac{1}{T_\mathrm{s}} \sum_{m=-\infty}^{\infty} S_{xx}\left(\frac{\Omega}{T_\mathrm{s}} + m\frac{2\pi}{T_\mathrm{s}}\right). \tag{B.12}$$

The argument of S_{xx} shows the repetition in the frequency domain. When the sampling time T_s is chosen such that there is no aliasing ($S_{xx}(\omega) = 0,$ for $|\omega| > 1/(2T_\mathrm{s})$), and considering a single FSR, Eq. B.12 can be written as

$$S_{\tilde{x}\tilde{x}}(\Omega) = \frac{1}{T_\mathrm{s}} S_{xx}\left(\frac{\Omega}{T_\mathrm{s}}\right), \quad -\pi < \Omega < \pi, \tag{B.13}$$

which we can rewrite using $\Omega = \omega T_\mathrm{s}$ to

$$S_{\tilde{x}\tilde{x}}(\omega T_\mathrm{s}) = \frac{1}{T_\mathrm{s}} S_{xx}(\omega). \tag{B.14}$$

If a sequence of independent samples is generated, with mean zero and a variance equal to $\sigma_{\tilde{x}}^2$, the following autocorrelation is found

$$R_{\tilde{x}\tilde{x}[m]} = \begin{cases} \sigma_{\tilde{x}}^2, & m = 0, \\ 0, & m \neq 0. \end{cases} \tag{B.15}$$

Note that for other values for m than zero, the autocorrelation is zero since all samples of the process x are uncorrelated, and the process is called white noise.

Inserting Eq. B.15 into Eq. B.5, we find that the power spectral density is equal to the variance of the discrete-time signal

$$S_{\tilde{x}\tilde{x}}(\Omega) = \sigma_{\tilde{x}}^2, \tag{B.16}$$

and therefore the discrete power spectral density can be used to describe a white noise process.

Appendix C

Simulator documentation

This chapter provides the documentation for the simulator tool. First, some general information will be given on the software that is used and the hardware on which the simulator tool has been developed. Next, a tour of the user interface will be given, explaining the settings that are used for simulations. At the end of this chapter an overview with common parameter values is given.

C.1 General information

The simulation model has been built in LabVIEW 8.6 [36] on a 3.0 GHz dual-core processor with 1.0 GB of RAM and a Microsoft Windows XP Professional operating system. Some of the operations executed in the simulator rely on Matlab (R2008b), which must be installed on the system. The required Matlab dependencies are automatically loaded in a Matlab Command Window when the simulation model is opened. Make sure that the path to the Matlab files is known by Matlab. This can be done by starting Matlab, and adding the path of the simulator tool with all subfolders in 'Set path', which is found in the 'file'-menu. Note that due to caching of Matlab code, changes are not immediately effective in LabVIEW. In order to make the changes effective, both the LabVIEW simulator and Matlab Command Window must be closed and restarted.

C.2 User interface

An overview of the user interface is given in Figure C.1. In the lower part of the screen the controls are categorized under tabs. At the right side of the screen, the downconverted QPSK signal after reception is shown, where the upper graph is the quadrature channel and the lower graph the in-phase channel. Next to the graphs, in the middle of the screen, the transmitted and decoded bitstreams for two different demodulation processes are shown.

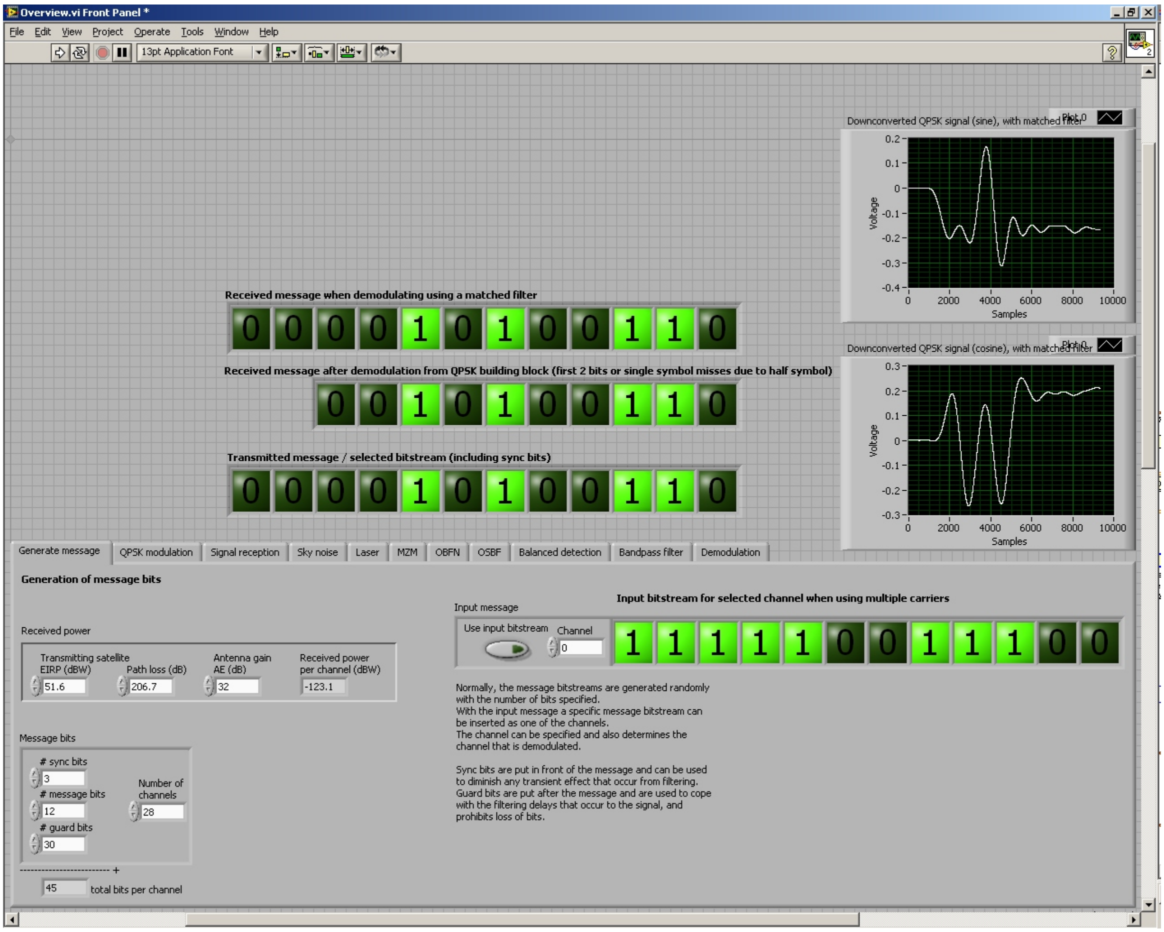

Figure C.1: User interface of the simulator tool at startup

We will continue with a description of the controls in the categorized tabs in the lower part of the screen. The tabs are:

- Generate message;
- QPSK modulation;
- Signal reception;
- Sky noise;
- MZM;
- OBFN;
- OSBF;
- Balanced detection;
- Bandpass filter;
- Demodulation.

C.2.1 Generate message

In this tab, the specification for the satellite signal can be found. The message will consist of one or more subcarriers (channels). There are three entry fields:

- *Received power*, in which the received signal power per channel is calculated;
- *Message*, in which the number of synchronization, message and guard bits can be specified, together with the number of channels;
- *Input message*, in which a specific input bitstream can be specified for one of the channels. The channel numbers start from zero.

Note that the synchronization and guard bits are always zero, and the message bits are generated randomly. The synchronization bits are not actually used for synchronization, but serve as an extra symbol since the first QPSK symbol will only consist of half the number of samples. The guard bits are used to cope with any delays that are inserted by filtering. The received power is used to scale the signal later on, after it has been QPSK-modulated.

C.2.2 QPSK modulation

This tab specifies the parameters for QPSK modulation. There are three sections with input fields:

- *Simulation and modulation parameters*, specifies the system sample rate and number samples per symbol. These two parameters determine the symbol rate;
- *Frequency specifications*, specifies the frequencies for the subcarriers. The signals are generated directly in the IF band, and depending on the IF start frequency and the number of channels, a certain part of the IF band will be used;
- *Pulse shaping parameters*, in which the pulse shaping filter can be specified, together with the pulse shaping coefficient and the filter length. When no pulse shape filtering is applied, the filter length should be set to 1. For the root raised cosine filter, a filter length of 8 is appropriate.

C.2.3 Signal reception

In this tab the angle of incidence and the number of AE are specified. There are three input sections:

- *Parameters planar antenna array*, specifies the number of AEs per linear array and the number of linear arrays;
- *LNB parameters*, specifies the equivalent noise temperature of the LNB, as well as the gain. An additional noise temperature for the feeder can be specified as well;

- *Incident angle*, specifies the zenith distance (θ) and azimuth angle (ϕ). The angles are depicted in the figure shown in the tab.

From the zenith distance and azimuth angle, the time delay between AEs within a linear array and the time delay between linear arrays are determined. These delays serve as input parameters for the OBFNs, such that the signals can be synchronized.

The network structures for OBFNs with up to 32 inputs are specified. For a larger number of inputs, new networks have to be added using the specification in Appendix A. Furthermore, the ring settings generator must be able to handle the number of ORRs per delay element to work properly.

C.2.4 Sky noise

Within this tab the insertion of sky noise can be regulated. Multiple sky noise sources can be identified using the following settings:

- *Noise temperature*, specifying the brightness temperature of each sky noise source;
- *Unit sample shift*, the number of sample shifts to realize a unit delay;
- *Decimation factors*, consisting of an array of decimation factors per source. The product of the individual decimation factors defines the total decimation factor.

For each source, the angle of incidence is determined by the product of decimation factors and the unit sample shift (Eq. 5.7). It is advantageous to use multiple decimation stages to make the downsampling operation more efficient. The number of decimation stages will not be equal for each sky noise source. However, LabVIEW needs the arrays with decimation factors to be equal in length, which is solved by padding the array with 1s.

Note that only one degree of freedom can be specified for the sky noise sources. This means that all sky noise sources will be located in the y-z plane, shown in the figure in the 'Signal reception' tab, or equivalently have an azimuth angle of 90 degrees. Furthermore, the larger the number of sky noise sources, the better the representation of actual sky noise will be.

C.2.5 MZM

In this tab the electrical to optical conversion is regulated. There are two input sections:

- *MZM parameters*, specifying ΔV, $V_{\pi,\mathrm{DC}}$, V_π and the loss, with which the bias and modulation depth of the MZM can be tuned;
- *Optical power*, equals the optical power emerging from the laser, which is split into the number of inputs (AEs).

With a correct bias, the even terms (including the carrier) can be suppressed. From [22] we know that the condition for this is $\Delta V = (2n+1)V_{\pi,\mathrm{DC}},\ n \in \mathbb{Z}$. V_π determines the modulation depth, i.e. that a smaller value will increase the modulation depth. The loss defines the excess loss in the MZM.

C.2.6 OBFN

This tab shows the path delays for the OBFN, based on the input settings that are given in:

- *OBFN parameters*, specifies the input parameters that are needed for the process that calculates the ring settings and shift the delays the correct frequency range.

The center frequency should be chosen to be in the middle of a single sideband, such that the signals are delayed appropriately. Note that the center frequency is given as a normalized frequency and that the chosen sideband must coincide with the passband of the OSBF.

Within the tab, two graphs are shown. The left graph shows the theoretical group delay responses for each path, that are calculated with Eq. 2.11. The right graph shows the simulated group delay responses using actual ORRs, which should match the left graph (apart from a possible shift over frequency). When the graphs are not identical, something went wrong in the conversion of the ring settings.

C.2.7 OSBF

In this tab the specification of the OSBF is performed. A resulting frequency response is shown, based on the input parameters:

- *OSBF parameters*, specifies the filter parameters. The parameters must be set, such that one of the signal sidebands is removed, while the other is passed unattenuated.

With the visualization of the magnitude response, shown in the graph in the tab, a reasonable filter characteristic can be obtained. Normally, the upper input and output are used (shown in Figure 2.13(b)), but with the switch buttons the other input and output can be selected as well. More information on tuning the filter can be found in [21].

C.2.8 Balanced detection

This tab specifies the detection of the optical signal by photodiodes. The following input sections are present:

- *Parameters PDs*, defines the photodiode parameters including responsivity, operating temperature and the shunt resistance;
- *TIA impedance*, specifies the transimpedance that converts the current to a voltage;
- *Coupling factor for carrier reinsertion*, specifying the the coupling factor (by means of θ) that regulates the DC that reinserts the unmodulated optical carrier.

Note that there are two photodiodes, which can have different values. This allows for example the possibility to simulate imbalances. If the photodiodes are perfectly balanced, the output current and voltage should have a zero direct-current value. The implementation noise does not require any parameters, since this only depends on the amount of impinging optical power.

C.2.9 Bandpass filter

This tab shows the modem operation, in which a channel selection is made. The available input field in this tab is:

- *Noise temperature*, specifies the equivalent input noise temperature of the BPF.

There is a button to select whether the bandpass filter should be used or not. In the case of simulations with only one channel, the filter is obviously unnecessary. The graph in the tab shows the signal spectrum before and after filtering, in which the individual subcarriers can be identified clearly.

The channel that is selected is shown together with its center frequency. The channel selection can be specified in the 'Generate message' tab, together with a possible bitstream. Note that the specified channel number will be used, whether or not the specified bitstream is used. Furthermore, some information about the filter is given, which is based on the frequency specification given in the tab 'QPSK modulation'.

C.2.10 Demodulation

This tab is used for synchronizing the demodulation carrier with the QPSK signal. The input fields are:

- *Amplitude mixing carrier*, specifies the amplitude of the carrier that is generated for demodulation;
- *Phase offset*, used to synchronize the mixing carrier with the signal to be demodulated.

For the demodulation process it is very important that the mixing carrier is synchronized with the QPSK signal. With the 'Use sync loop' button enabled, the phase offset can be set to the correct value, while using the graph in the tab for the alignment. It has proven beneficial to align the mixing carrier a small fraction to the right of the QPSK signal.

C.3 Parameters

In this section, an overview of parameters and constants will be given. Most of the parameters are already set in the simulator tool, but the overview is also meant as a reference.

The DVB-S standard describes the signal [35]:

◇ *Modulation scheme*	QPSK
◇ *RF frequency range*	10.7–12.75 GHz
◇ BW/R_{symb}	1.28
◇ *Pulse shaping filter*	root raised cosine
◇ *Pulse shaping coefficient*	0.35

For Europe and North Africa, DVB-S is provided by a satellite fleet from Astra, called 19.2°E [26]. The fleet consists of multiple satellites, that each only provide a part of the total frequency band.

◇ *Polarization*	H/V
◇ *Number of subcarriers*	60 per polarization
◇ *Channel bandwidth*	26–36 MHz
◇ *Guard band*	$>$ 4 MHz
◇ *Altitude*	$\approx$ 36,000 km

Most Dutch television channels are provided by the Astra 1H satellite from the fleet. The bandwidth of the subcarriers is 33 MHz, which is the value that is also used for the simulator. With the specified $\mathrm{BW}/R_{\mathrm{symb}}$ a symbol rate of 25.8 Mbaud results.

For the SMART project, the following parameters were assumed [27]:

◇ *Transmit power (EIRP)*	51.6 dBW
◇ *Pathloss*	206.7 dB
◇ *Number of AEs*	1569
◇ *AE spacing*	1.5 cm
◇ *PAA gain*	32 dB

The gain of an individual AE depends a lot on the fabrication techniques, but can be considered to be around 3 dB.

From the datasheet of the LNB we can deduce the following parameters [45]:

◇ *IF frequency range*	950–2150 MHz
◇ *Gain*	60 dB
◇ *Noise temperature*	50 K

For the conversion of the electrical IF signal to the optical domain, the following parameters are assumed:

◇ *Optical laser power*	20 mW
◇ *Excess loss MZM*	3–5 dB
◇ ΔV	$(2n+1)V_{\pi,\mathrm{DC}},\ n \in \mathbb{Z}$

The loss in the ORRs depends on the unit loss and the circumference of the ORRs.

◇ *Ring loss*	0.1–0.5 dB/cm
◇ *ORR circumference OBFN*	1.44 cm
◇ *ORR circumference OSBF*	2.89 cm

For the conversion of the optical signal to the electrical domain, the following parameters can be assumed [44, 34]:

◇ *Responsivity photodiodes*	0.8 A/W
◇ *Shunt resistance*	10–10000 MΩ
◇ *Transimpedance*	1200 Ω

Furthermore, the following parameters are assumed throughout the system:

◇ *Characteristic line impedance*	50 Ω
◇ *Reference temperature for components*	290 K (room temp.)